90845

AEROSPACE REPORT NO
ATR-76(7509)-1

# Investigation of Fire Whirls and Firebrands

Prepared by A. MURASZEW and J. B. FEDELE
Vehicle Engineering Division
The Aerospace Corporation
El Segundo, Calif. 90245

and

W. C. KUBY
University of California, Santa Barbara

30 April 1976

DESIGNATED STATION REPRESENTATIVE: R. C. ROTHERMEL
NORTHERN FOREST FIRE LABORATORY
INTERMOUNTAIN FOREST AND RANGE EXPERIMENT STATION
Missoula, Montana 59801

Prepared for

USDA FOREST SERVICE
Washington, D. C.

INT Grant No. 16

THE AEROSPACE CORPORATION

Report No. ATR-76(7509)-1

# INVESTIGATION OF FIRE WHIRLS AND FIREBRANDS

Prepared by

A. Muraszew and J. B. Fedele
Vehicle Engineering Division
The Aerospace Corporation
El Segundo, Calif. 90245

and

W. C. Kuby
University of California, Santa Barbara

30 April 1976

Designated Station Representative: R. C. Rothermel
Northern Forest Fire Laboratory
Intermountain Forest and Range Experiment Station
Missoula, Montana 59801

Prepared for

USDA FOREST SERVICE
Washington, D. C.

INT Grant No. 16

Report No.
ATR-76(7509)-1

# INVESTIGATION OF FIRE WHIRLS AND FIREBRANDS

Approved by

A. Muraszew, Senior Staff Engineer
Aero Engineering Subdivision
Vehicle Engineering Division

E. G. Hertler, Director
Aero Engineering Subdivision
Vehicle Engineering Division

P. Stevens, Director
Resource Development Office
Energy and Transportation Division

## ACKNOWLEDGMENTS

The authors would like to acknowledge the contribution of R. C. Rothermel and his colleagues at the Northern Forest Fire Laboratory (NFFL) in Missoula, Montana, in the form of high quality experimental data and constructive suggestions with regard to data analysis.

The authors would also like to express appreciation to M. L. Brown of NFFL for his keen perception and inventiveness in the firebrand experiment set up and instrumentation, and to Mr. R. Postolka of the University of California, Santa Barbara, for his resourcefulness and diligence in development of instrumentation and test techniques for the fire whirl experiments.

CONTENTS


ACKNOWLEDGMENTS . . . . . iii

I. INTRODUCTION . . . . . 1

II. SUMMARY OF PREVIOUS WORK . . . . . 4

III. INVESTIGATION OF FIREBRAND BURNING . . . . . 8

A. Goals and Method . . . . . 8

B. Further Development of the Experimental Technique . . . . 9

1. Igniter Development . . . . . 10

2. Improvement in Firebrand Measurement Technique . . . . . 10

C. Results and Discussion . . . . . 11

1. Burning in Still Air. . . . . 11

2. Burning in Wind . . . . . 16

3. Effect of Relative Air Humidity . . . . . 27

4. Effect of Fuel Moisture . . . . . 28

5. Flaming Versus Glowing Combustion . . . . . 31

IV. ANALYSIS OF FIRE WHIRL AND FIREBRAND INTERACTION . . . . . 35

A. Goals . . . . . 35

B. Fire Whirl Analytical Model . . . . . 37

C. Formulation of Firebrand Trajectory Model . . . . . 49

D. Analytical Results and Discussion . . . . . 55

1. Correlation of Fire Whirl Analysis and Experimental Data . . . . . 55

2. Extrapolation of the Model to Full-Size Fire Whirl. . . . 63

3. Firebrand Trajectory Calculations . . . . . 80

V. EXPERIMENTAL WORK . . . . . 98

A. Introduction . . . . . 98

CONTENTS (Continued)

B. Experimental Apparatus and Instrumentation . . . . . 98
C. Wood Crib Test Results and Discussion . . . . . 102

VI. CONCLUSIONS . . . . . 126

VIII. RECOMMENDATIONS . . . . . 128

APPENDICES:

A. INSTRUMENTATION ERROR EVALUATION . . . . . 129
B. ACETONE FIRE WHIRLS . . . . . 134

SYMBOLS . . . . . 150

REFERENCES . . . . . 154

FIGURES


| | | |
|---|---|---|
| 1. | Data Flow - Fire Spread Simulation | 2 |
| 2. | Density Change of Oven-Dry Burning Wood Cylinders, Wind Velocity = 0 mph | 12 |
| 3. | Density Change of Burning Oven-Dry Wood Plates | 14 |
| 4. | Final Density as a Function of Diameter or Thickness at Wind Velocity, v = 0 | 15 |
| 5. | Comparison of Experimental and Calculated Values for Weight Ratio of In-Still-Air Burning Firebrands | 17 |
| 6. | Density Change of Burning of Oven-Dry Wood Cylinders, Wind Velocity, v | 18 |
| 7. | Change in the Exponential Constant, k, with Wind Velocity | 20 |
| 8. | Comparison of Experimental and Calculated Values for Weight Ratio of In-Flight Burning Firebrands | 21 |
| 9. | Simulated Firebrand Burning After Impact | 23 |
| 10. | Area (Volume) Change of Burning Oven-Dry Wood Plates. | 26 |
| 11. | Effect of Wood Moisture on Burning Rate | 29 |
| 12. | Correlation Between Experimental and Analytical Expression for the Effect of Moisture on Wood Burning Rate | 30 |
| 13. | Fire Whirl Geometry | 39 |
| 14. | Variation of Experimental Constants (a', b') with Burn Rate and Circulation Intensity | 62 |
| 15. | Variation of Mean Vertical Velocity (at ground zero) and Burn Rate Amplification Factor with Circulation Strength and Height | 69 |
| 16. | Firebrand Trajectory Experiments | 82 |
| 17. | Firebrand Subscale Trajectory, Height vs Time | 83 |

FIGURES (Continued)


18. Firebrand Subscale Trajectory, Height vs Time . . . . . 84

19. Firebrand Subscale Trajectory, Height and Radial Position vs Time . . . . . 85

20. Azimuthal Trajectory of a Firebrand in the Swirl. . . . . 90

21. Fire Whirl Core and Firebrand Vertical Velocity. . . . . 91

22. Firebrand Weight Change in Flight . . . . . 92

23. Firebrand Trajectories In and Out of the Fire Whirl . . . . . 93

24. Firebrand Trajectories In-Wind for Various Woods . . . . . 95

25. Firebrand Trajectories In-Wind from Various Initial Heights . . . . . 96

26. Wood Crib Configuration . . . . . 104

27. Wood Crib Ignition . . . . . 105

28. Typical Time Variation of Fire Whirl Parameters . . . . . 106

29. Developed Fire Whirl Core . . . . . 108

30. Axial Temperature and Vertical Velocity Variation with Crib Diameter. . . . . 110

31. Circulation and Burn Rate Variation with Crib Diameter . . . . 111

32. Temperature Profiles as Function of Crib Diameter . . . . . 112

33. Burn Rate Variation with Stick Height . . . . . 114

34. Temperature Profiles as Function of Height of Burning Sticks . . . . . 115

35. Radial Distribution of Vertical Velocity . . . . . 116

36. Radial Distribution of Tangential Velocity. . . . . 117

37. Axial Velocity Variation with Height. . . . . 119

FIGURES (Concluded)


| | | |
|---|---|---|
| 38. | Axial Temperature Variation with Height . . . . . | 120 |
| 39. | Temperature Profile Variation with Vertical Height. . . . . | 121 |
| A-1. | True Gas Temperature Compared to Measured Temperature Using Thermocouple . . . . . | 132 |
| B-1. | Temperature Profiles at Height of 17 in. for Various Dish Diameters . . . . . | 136 |
| B-2. | Temperature Profiles at Height of 45 in. for Various Dish Diameters . . . . . | 137 |
| B-3. | Axial Velocity Variation with Dish Diameter at Various Heights . . . . . | 138 |
| B-4. | Circulation Profiles at Height of 45 in. for Various Dish Diameters . . . . . | 139 |
| B-5. | Acetone Burn Rate Variation with Boundary Layer Gap . . . | 141 |
| B-6. | Acetone Burn Rate Variation with Swirl Air Flow . . . . . | 142 |
| B-7. | Tangential Velocity Distribution at Various Heights . . . . . | 143 |
| B-8. | Circulation Distribution at Various Heights . . . . . | 144 |
| B-9. | Temperature Profiles at Various Heights . . . . . | 146 |
| B-10. | Axial Temperature and Vertical Velocity Variation with Height . . . . . | 147 |
| B-11. | Velocity Vector Direction Variation with Radial Position . . . . . | 148 |
| B-12. | Vertical Velocity Profiles at Various Heights . . . . . | 149 |

TABLES


1. Fall Velocity of Wood Samples (Oven-Dry) . . . . . 33

2. Fire Whirl Parameters for UCSB Experiments . . . . . 59

3. Core Properties versus $\Gamma$, $z_e$ for $\rho_b R_o$ = 0.1165 $lb_m$/$ft^2$-sec, d = 4/900 ft . . . . . 68

4. Effect of d (Effective Stick Diameter) on Core Properties for $\Gamma$ = 3000 $ft^2$-sec, $z_e$ = 3000 ft, and Constant $\rho_b R_o$ = 0.1165 $lb_m$/$ft^2$-sec . . . . . 70

5. Core Properties versus $\Gamma$, $z_e$ for $\rho_b R_o$ = 0.03 $lb_m$/$ft^2$-sec, d = 4/900 ft . . . . . 71

6. Core Properties versus $\Gamma$, $z_e$ for $\rho_b R_o$ = 0.3 $lb_m$/$ft^2$-sec, d = 4/900 ft . . . . . 74

7. Core Properties versus $\Gamma$, $z_e$ for $\rho_b R_o$ = 0.7 $lb_m$/$ft^2$-sec, d = 4/900 ft . . . . . 75

8. Boundary Layer Radial Inflow Velocity at Core Base, for d = 4/900 ft . . . . . 79

9. Effect of Initial Core Radial Position and Firebrand Orientation on Maximum Firebrand Range: $D_o$ = 2 in., L = 8 in., $\rho_{w_o}$ = 30 $lb_m$/$ft^3$ (red pine) . . . . . 88

10. No-Swirl Burn Rate Data (Oven-Dry Fuel) . . . . . 122

# I. INTRODUCTION

The Aerospace Corporation investigation of fire whirls and firebrands described in this report continues work begun in 1972 and subsequently funded in CYs 1974 and 1975 by the USDA Forest Service, Northern Forest Fire Laboratory (NFFL), Missoula, Montana, under the direction of R. C. Rothermel. The research work performed under Aerospace funding was described by Muraszew[1]. The continuing effort under Forest Service Grant No. 12 was reported by Muraszew, Fedele and Kuby[2]. The continuation of firebrand investigation under Forest Service Grant No. 16 is the subject of this report.

The purpose of the Firebrand Investigation Program is to develop a statistical definition of the hazard of spot fires generated by short- and long-range firebrands.

Previous field observations and analyses have shown that a "normal" two-dimensional convection column created above a fire front can lift small brands and embers and deposit them closely ahead of the fire front. However, in most cases such a column does not possess sufficiently high uplift velocities to lift larger size firebrands (1/2-in. diameter or larger) high enough for them to be wind-borne 1/2 mile or further, forming there a possible nucleus of a spot fire. Calculations of "normal" convection column uplift velocities were investigated by several researchers, and review of their work, as well as trajectory calculations for near-field firebrands, were presented in Ref. 1.

In addition, it was observed that fire whirls that occasionally form over a fire front can throw firebrands large distances. Since no comprehensive analysis of this phenomenon was available, the evaluation of fire-whirl-generated firebrands was undertaken. The fire whirl and firebrand problem is complex, and is but one part of the total fire-spreading phenomenon diagrammed in Fig. 1. Several successive analytical and experimental steps have to be taken to describe the role of fire whirls and firebrands. It is

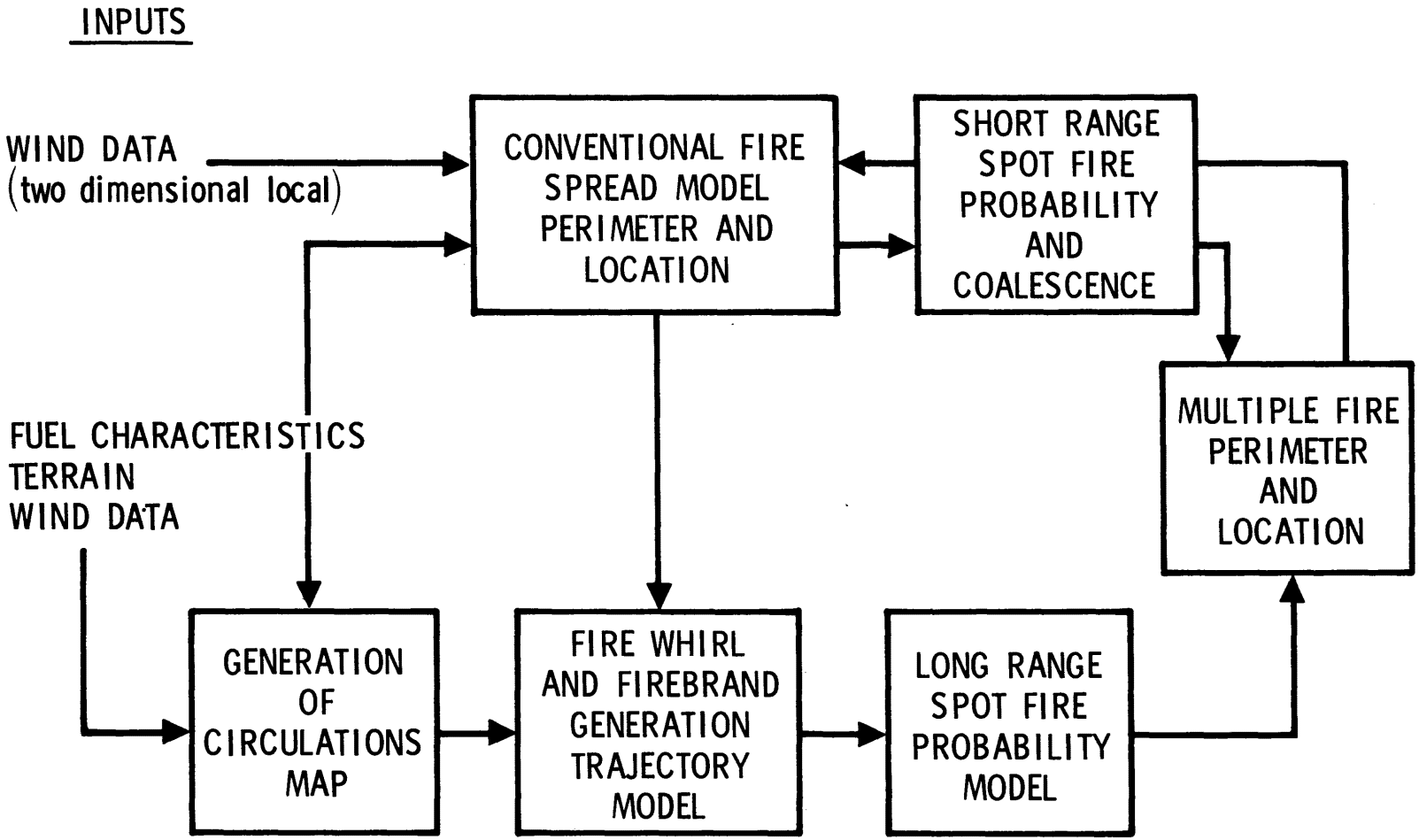


Fig. 1. Data Flow - Fire Spread Simulation

assumed that burning-fuel characteristics are known and that a fire spread model for a conventional continuous fire front is available[3] from which the characteristics of a conventional two-dimensional convection column can be defined. From this and the known ambient wind (as distinguished from local air movement caused by the fire), the trajectory of firebrands of various sizes and their condition at impact can be calculated with the existing models[1].

The work completed to date on the Firebrand Investigation Program has primarily concentrated on generation of spot fires through long-range travel of firebrands. Spot fire mechanisms such as fire whirls were postulated, and a mathematical model was formulated characterizing a fire whirl as a function of the initiating swirl and burning-fuel characteristics. Trajectory calculations of firebrands of various sizes lifted by the fire whirl and carried by the wind were performed and are discussed in this report.

To assess the probability of spot fire occurrence requires additional effort on the statistical assessment of the number and size of firebrands lifted, formulation of recipient fuel ignition criteria, and estimation of the probable number of spot fires generated. The probability of the occurrence of an initiating swirl, which is a function of ambient wind, topography, and fuel characteristics (identified in Fig. 1 as "generation of circulations map") also has yet to be evaluated and enters into the long-range spot fire probability assessment. The probability of short-range spot fires and their coalescence near the fire front to form pseudo-flame fronts which could increase the rate of fire spread by a factor of 3 to 5[4] has not been investigated and requires additional effort.

Finally, the probability models of short- and long-range spot fires should be integrated into an overall fire spread model which would give the fire-fighting managers a most probable real time assessment of the hazards involved.

## II. SUMMARY OF PREVIOUS WORK

This section summarizes work completed in 1974 under Forest Service Grant No. 12 and reported previously[2]. This work had two main objectives: (1) to evaluate experimentally and to define analytically the changes in weight and size of firebrands burning in the wind and on the ground, and (2) to generate and confirm experimentally an integrated mathematical model of a fire whirl--coupling the ground boundary layer flow, the burning-fuel heat transfer, and the fire whirl core flow as a function of the initiating ambient swirl and burning-fuel characteristics.

Experimental work on firebrand burning was performed at the NFFL in Missoula, Montana, under the direction of R. C. Rothermel. From this work, it appeared that the change in average density (i.e., density of virgin wood and char combined) of burning wood can be approximated by

$$\frac{\rho_{(t)} - \rho_c}{\rho_o - \rho_c} = e^{-\frac{t}{D_o \cdot k}} \qquad (1)$$

where $\rho_o$, $\rho_{(t)}$, $\rho_c$ are initial, instantaneous, and final (when the burning stopped) wood densities, $D_o$ is initial sample diameter (or characteristic dimension), and k is an experimental constant and a function of wind velocity. This equation is further amended in this report to obtain a better correlation with experimental data.

When burning in the wind (simulating free fall), part of the char was blown away and, provided the element was ignited over the whole surface, the burning continued with $\rho_c \sim 0$ (i.e., the specimen burned up completely). When burning on the ground, the burning stopped at some point which was mainly a function of the initial sample diameter. The value of $\rho_c$ for ground burning was evaluated experimentally and defined by an empirical equation.

To obtain an analytical expression for the change in fir[redacted] teristic dimension D (diameter for cylinders and for other shap[redacted] flat plates the equivalent ratio of volume to surface, 4V/S) the wor[redacted] by Tarifa[5] was utilized. Tarifa observed that the ratio of instantaneous to initial free fall velocity of firebrands $[w_{(t)}/w_o]$ can be represented for a variety of sizes and wood types by a unique function of initial sample characteristics and burn time. When the initial characteristics of a firebrand are known, the ratio of fall velocities can be determined at any time.

The instantaneous characteristic dimension can be expressed as

$$\frac{D_{(t)}}{D_o} = \left[\frac{w_{(t)}}{w_o}\right]^2 \cdot \frac{\rho_o}{\rho_{(t)}} \qquad (2)$$

and the condition of the firebrand at impact after a known time of flight can be established.

In the generation of the analytical model of a fire whirl, the work of several researchers was reviewed and utilized. It was found that none of this past work considered a comprehensive model of a fire whirl coupling the ground boundary layer with the burning fuel and the fire whirl core flow. Since such a model was required for evaluation of fire whirls as firebrand lifters, analysis was performed and a mathematical model of a fire whirl was created based on the characteristics of the ambient circulation initiating the fire whirl and the burning fuel properties.

In order to obtain solutions using input data available in the field, several simplifications were introduced; however, the pertinent physical processes were retained. A major simplification consisted of computing radially averaged core properties so that the gas dynamics equations (i.e., conservation of mass and momentum) could be expressed as a function only of one independent variable, z, the height within the core. Boundary conditions at the core-ambient air interface were obtained from Ref. 6.

[redacted]tion for the core parameters derived with the simplifying
[redacted]ns is

$$(\rho_\infty - \rho) g a_o^2 = \frac{\rho_\infty \cdot \Gamma^2}{2 \cdot z_e} \tag{3}$$

where $\Gamma$ is the ambient circulation (tangential velocity times radius), $\rho_\infty$ and $\rho$ are ambient air density and average gas density in the core, respectively, $a_o$ is the core radius at zero height, and $z_e$ is the fire whirl height.

A separate energy balance was employed relating the steady state fuel ignition to the heat convected to the fuel surface at the fire whirl core. Using Reynolds' analogy to relate the heat transfer to the skin friction at the fuel surface-core interface, a convective heat transfer coefficient was defined as a function of core and fuel properties.

An overall mass balance was utilized which included the radially inward ground boundary layer flow, the burning-fuel mass addition, and the upward core flow. In calculating the boundary layer flow, Schlichting's analysis for pure rotational flow above the ground[7] was used with the necessary modifications to account for energy and mass addition into the core. It was assumed that at high values of swirl intensity entrainment of air along the core height will not greatly affect the radially averaged core uplift velocities. From the set of equations, a fuel burn amplification factor--i.e., the ratio of the rate of fuel burning with swirl to that without swirl--was obtained. The no-swirl, real fire, burn rate data were obtained from Rothermel's work[3].

The equation derived from the burn rate amplification factor in the fire whirl is

$$\frac{R}{R_o} = 1 + \frac{h_w (T - T_s)}{\rho_b \cdot R_o \cdot Q_i} \tag{4}$$

where R and $R_o$ are linear burn rate of fuel (ft/sec) in the presence of swirl and no swirl, respectively; T and $T_s$ are average core temperature and fuel surface temperature, respectively; $h_w$ is convection heat transfer calculated from Reynolds' analogy; $Q_i$ is heat input required for fuel ignition (Btu/lb); and $\rho_b$ is the bulk density of the fuel.

Experimental work to verify the various assumptions made was carried out at the University of California, Santa Barbara, under the direction of W. C. Kuby. A relatively large fire-whirl generator (3-ft diameter, 18-ft height) was built in which the initiating swirl was produced by tangential ground boundary layer inlets into the generator and by using a blower to tangentially discharge air at various heights into the apparatus. Acetone was burned in the initial phase of the program; this was followed by several tests with wood cribs. The tests verified the main assumptions regarding the "top hat" distribution of axial velocity and of averaging temperature within the core. Agreement with the measured and calculated values of burn rate amplification ratio was obtained. The tests also provided preliminary data for the definition of two experimental factors: one was included in the heat transfer coefficient, and the other factor was in the ground boundary layer formulation used in the overall mass balance equation.

At the conclusion of the 1974 work, it appeared that modifications to the experimental fire whirl test rig were required to increase the swirl intensity and provide means of swirl control. Tests using various wood fuels for obtaining data on firebrand generation and correlating fire whirl analytical models for natural wood burning were also desired. Further, in-wind burning data with natural fuels at varying moisture content required additional analysis, and test data received from wind tunnel experiments could be improved by control of ignition time for test repeatability. The work discussed in this report was directed toward achieving these goals.

## III. INVESTIGATION OF FIREBRAND BURNING

### A. GOALS AND METHOD

The goal of this investigation is to derive analytical means for prediction of firebrand condition at impact, knowing its initial condition and the time of flight, and to predict the progress of burning on the ground after impact. Such information is necessary for the prediction of firebrand ability to ignite recipient fuels.

To achieve this goal:

1. Review of literature on cellulose-type fuel ignition and burning and the results of such review were presented in previous reports[1,2].

2. Experimental work on wood samples was carried out in still air and in wind tunnels at various wind velocities at the NFFL in Missoula, Montana[2]. The wood samples were mostly cylindrical varying in size from 2.5 to 0.6 cm diameter, but some tests were also carried out with 12.6 by 12.6 cm flat plates as representative of wood shingles and flat bark pieces. The wood types included pine, Ponderosa pine, birch, Western larch, spruce, and cedar.

3. Analysis was conducted utilizing the work of other researchers as well as the experimental data obtained from Missoula to arrive at a set of semiempirical equations describing firebrand burning processes. It must be realized that wood burning is a complex thermochemical process with nonhomogeneous material. While the experimental method was refined to reduce the error of measurements, some spread of data was unavoidable because of wood nonhomogeneity and because of the sample-to-sample differences in wood combustion.

The nonhomogeneity of wood can be illustrated, for instance, by a variation in virgin wood density of wood samples of any given type. For birch, the mean density of oven-dry samples was 0.6 $g/cm^3$ with a coefficient of variation of ±11.5%; for pine, the mean density was 0.42 $g/cm^3$ with a coefficient of variation of 12.6%, but the difference between the lowest and highest density was 65% for birch and 43% for pine. A similar trend was observed in

other woods. Since the thermal diffusivity of wood changes with its density, a variation in the burn rate of any one type of wood under the same test conditions can be expected and was indeed observed.

To maintain as much uniformity of combustion as possible, a considerable effort was spent on development of an ignition technique which would provide a uniform burning over the whole surface of a sample at the end of the ignition period. However, even with all the precautions taken, early changes in the combustion pattern developed. Small cracks on the charred surface formed randomly, changing the heat transfer process into the wood and causing occasional "jetting" of hot gases from the cracks and changing the flaming and the glowing periods. The longer a sample was allowed to burn, the greater was the effect of combustion variability on the data spread. In addition, the smaller the remaining mass and size of a sample at the end of the measured burn time, the greater the experimental error in determining its size and average density. To reduce the above data spread, each test was repeated three or more times for data averaging.

In the development of an empirical correlation for prediction of firebrand burning rate, the above factors had to be considered and a "representative" burn rate established by using mean values for defining the experimental constants or by application of linear regression technique to correlate the data.

## B. FURTHER DEVELOPMENT OF THE EXPERIMENTAL TECHNIQUE

The test setup for observations and measurements of firebrand burning in wind and in quiescent air was briefly described in Ref. 2, and a more detailed description of the apparatus, instrumentation, and techniques developed will be presented in a future NFFL report.

The comments in this report will, therefore, be limited to indicate the evolution of the apparatus and experimental technique which took place during 1975 subsequent to the work described in Ref. 2.

1. Igniter Development

Uniform and complete ignition of a sample was considered of paramount importance in the reproducibility of burn data. On the other hand, it was considered very important to minimize the ignition time and the sample weight loss during ignition so that the subsequent self-burning process was least affected by the ignition phase.

A natural gas multi-hole igniter with a small addition of oxygen was developed to try to satisfy both constraints. The igniter was shielded to minimize wind effects during ignition, and the sample was rotated to assure even ignition of the whole surface. This arrangement proved satisfactory and resulted in a uniform ignition, although the ignition weight loss of 25 to 30% was higher than the desired 20% limit which corresponds to the amount that would have been lost due to self-burning within the same time interval.

The ignition time was 30 to 35 sec for the 1-in. dowels and shorter for the smaller diameter samples corresponding approximately (in sec) to 12 to 14 times the diameter of the sample expressed in cm.

2. Improvement in Firebrand Measurement Technique

The methods used previously for determination of instantaneous size and weight of burning samples were found inadequate for the desired accuracy measurements. The accuracy goal was ±2% for weight and ±10% for volume.

The weighing system consisted of a cantilevered beam equipped with a strain gage whose output was measured after filtration and amplification, resulting in a linear relationship between the weight and the signal. The weighing instrumentation was quite accurate, but the source of error lay in asymmetrical wind drag forces developed during sample burning. Initially, the sample was placed horizontally in the tunnel and any asymmetry in the drag affected the weight readings. This was overcome by vertical placement of the sample in the tunnel, and satisfactory weight readings were subsequently obtained with expected accuracy of ±5%.

The instantaneous size of the sample was measured in the early work from photographs obtained by two cameras 90 deg apart viewing the sample end-side and broadside. However, it was difficult to determine an accurate calculation of volume from the size measured, mainly because the sample shape was frequently asymmetrical and irregular and because distinct outlines of glowing sample boundaries could not be obtained.

Consequently, the measuring method was revised. A sample was allowed to burn for a predetermined time, then removed from the tunnel, quenched in nitrogen, and weighed. To determine volume, the sample was immersed in a known volume of water. To account for the water absorbed by the sample, it was weighed again and a correction was made to obtain the true volume. The estimated accuracy of weight measurements was ± 2% and volume measurements ±10%.

## C. RESULTS AND DISCUSSION

Reference 2 described the shape, size, and wood type of samples used in the experimental work at NFFL. Tests were carried out with varying wind velocities (0 to 25 mph) simulating the range of the fall velocities of the samples at "baseline" condition of oven-dry fuels (i.e., approximately 2% of moisture), 25% relative air humidity, and 85°F ambient temperature. Other tests were carried out with varying relative humidity or varying fuel moisture to evaluate the effects of these parameters on fuel burning.

Early test data were presented and discussed[2]. Additional data obtained with the improved test technique had an influence on the form of empirical equations derived earlier. The discussion here will therefore be limited to presentation of the new data and of modified empirical expressions for prediction of firebrand burn rates.

### 1. Burning in Still Air

The burn data of zero wind velocity are shown in Fig. 2 for a variety of wood and wood sizes. Analyses of the data by Rothermel have shown that an empirical equation with $1/D_o^2$ in the exponent provides a better fit than the previously derived equation with $1/D_o$.

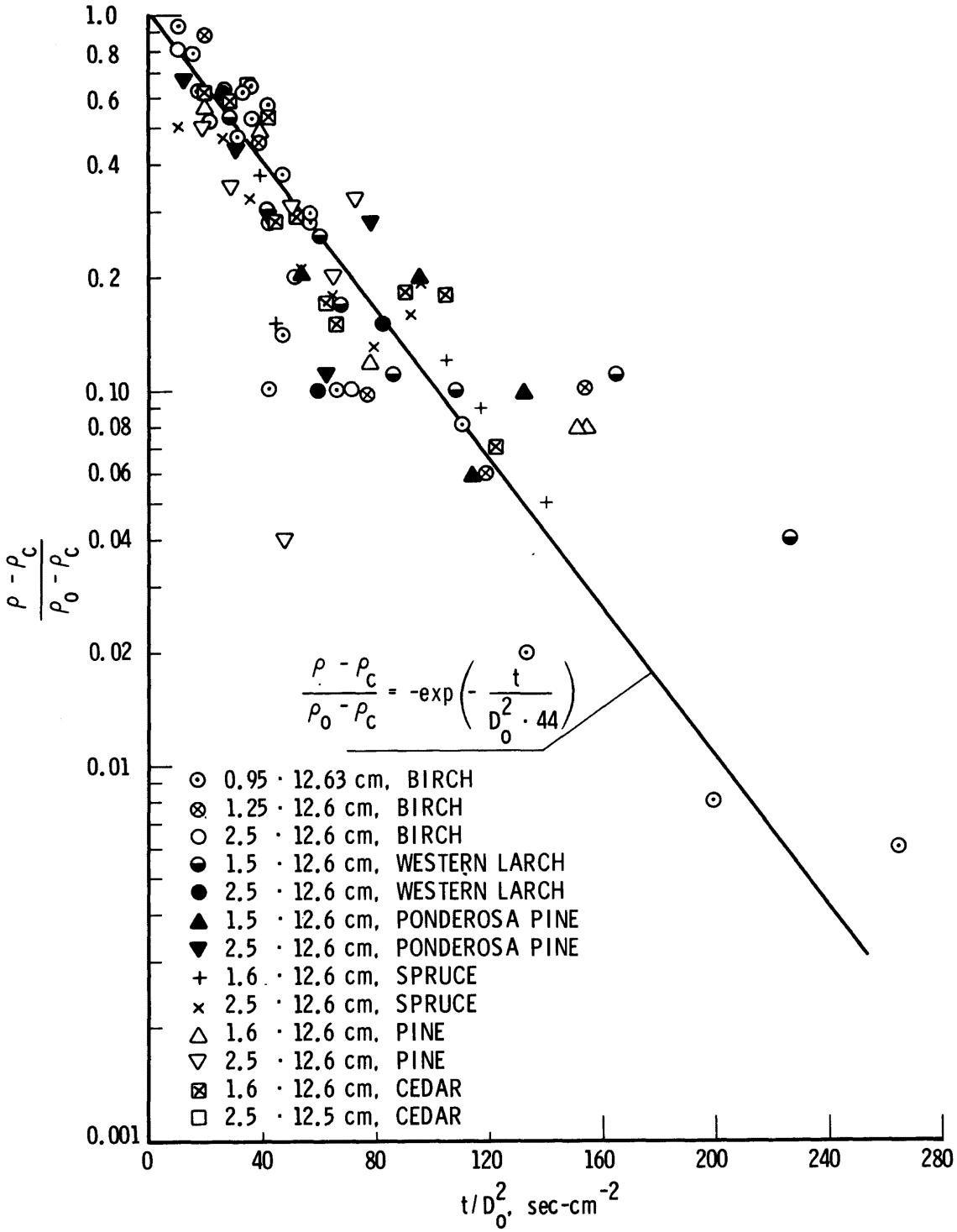


Fig. 2. Density Change of Oven-Dry Burning Wood Cylinders, Wind Velocity = 0 mph

The density change for cylindrical shapes is defined by

$$\frac{\rho - \rho_c}{\rho_o - \rho_c} = e^{-\frac{t}{D_o^2 \cdot 44}} \tag{5}$$

where

$\rho$ = instantaneous average density of firebrand
$\rho_o$ = initial density
$\rho_c$ = final average density at cessation of burning
$t$ = burn time, sec
$D_o$ = initial diameter, cm

The constant k = 44 sec/cm$^2$ and represents a mean of 75 test data with a standard deviation of 12.9.

For square plates (Fig. 3b)

$$\frac{\rho - \rho_c}{\rho_o - \rho_c} = e^{-\frac{t}{h_o \cdot 126}} \tag{6}$$

where $h_o$ is the initial plate thickness, in cm. The constant k = 126 represents a mean of 31 test data with a standard deviation of 31.9.

The final burn density $\rho_c$ is defined for cylinders and square plates by (see Fig. 4)

$$\frac{\rho_c}{\rho_o} = 0.5 \left(\frac{V_o}{S_o}\right)^2 \tag{7}$$

where $V_o$ and $S_o$ are initial volume (cm$^3$) and surface area (cm$^2$) of a sample, respectively. For cylinders

$$\frac{\rho_c}{\rho_o} = 0.5 \left(\frac{D_o}{4}\right)^2 \tag{8}$$

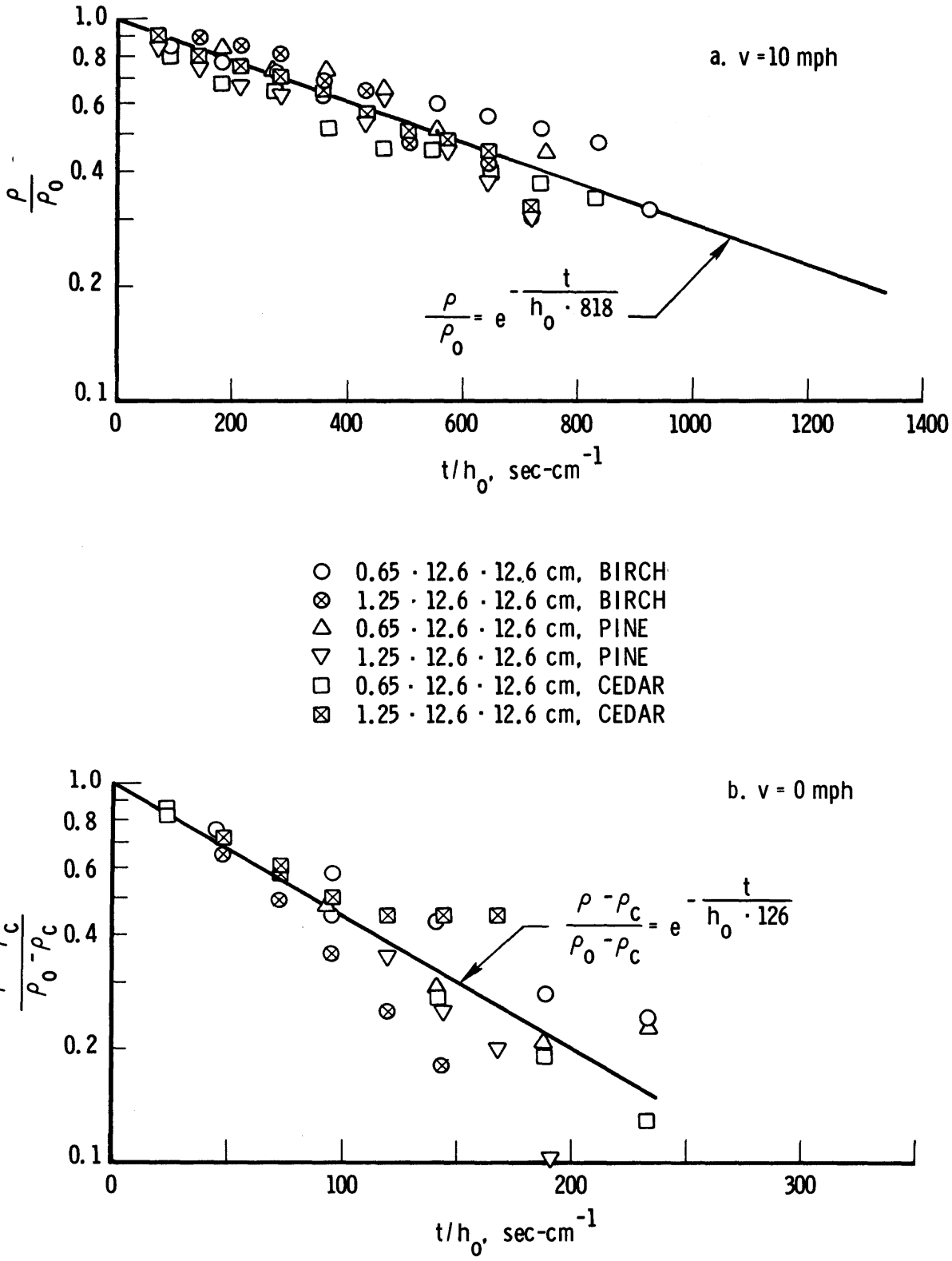
a. v = 10 mph
$\frac{\rho}{\rho_0}$
$\frac{\rho}{\rho_0} = e^{-\frac{t}{h_0 \cdot 818}}$
t/h0, sec-cm-1
○ 0.65 · 12.6 · 12.6 cm, BIRCH
⊗ 1.25 · 12.6 · 12.6 cm, BIRCH
△ 0.65 · 12.6 · 12.6 cm, PINE
▽ 1.25 · 12.6 · 12.6 cm, PINE
□ 0.65 · 12.6 · 12.6 cm, CEDAR
⊠ 1.25 · 12.6 · 12.6 cm, CEDAR
b. v = 0 mph
$\frac{\rho - \rho_c}{\rho_0 - \rho_c}$
$\frac{\rho - \rho_c}{\rho_0 - \rho_c} = e^{-\frac{t}{h_0 \cdot 126}}$
t/h0, sec-cm-1

Fig. 3. Density Change of Burning Oven-Dry Wood Plates

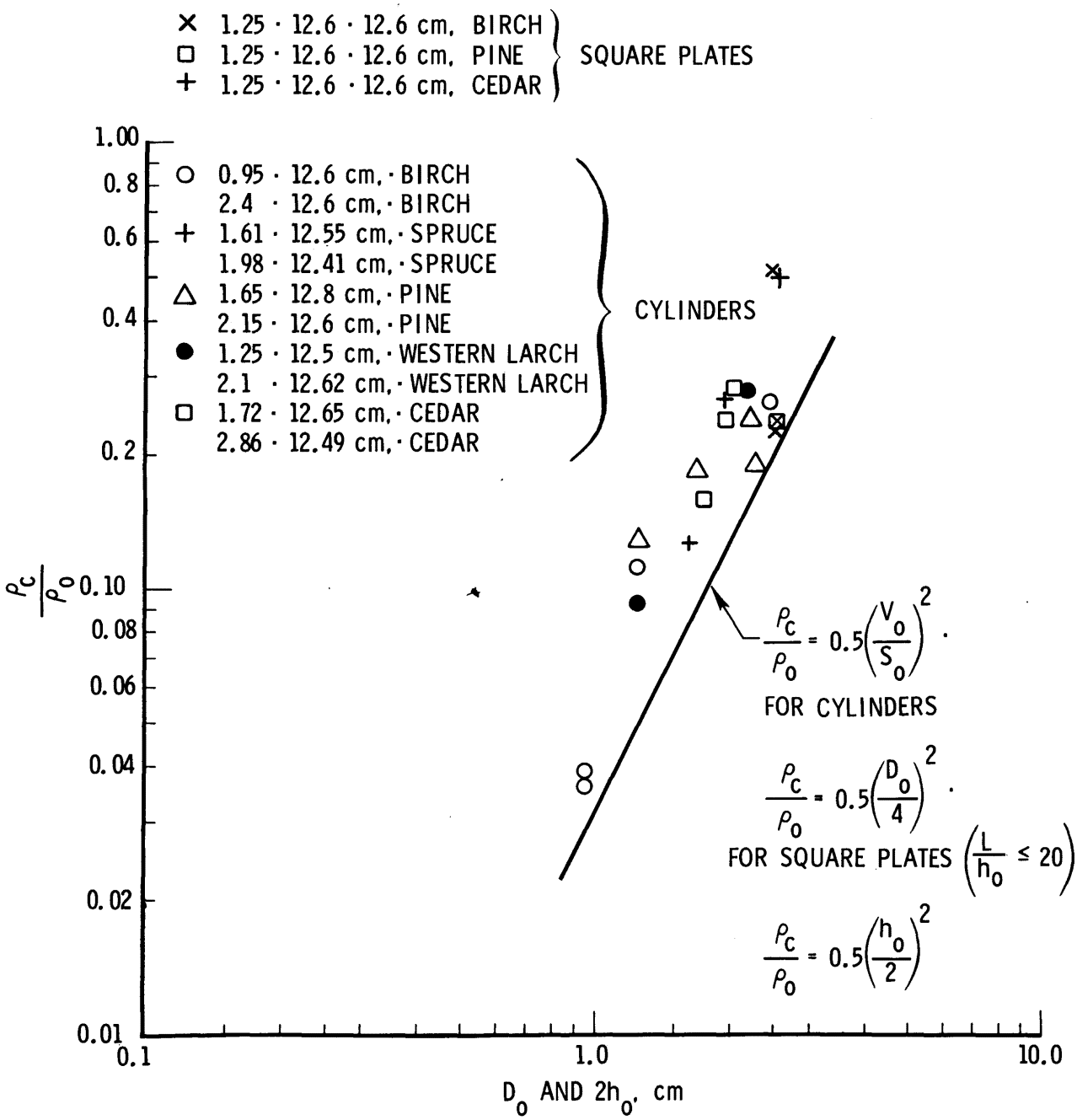


Fig. 4. Final Density as a Function of Diameter or Thickness at Wind Velocity, v = 0

and for plates

$$\frac{\rho_c}{\rho_o} = 0.5 \left(\frac{h_o}{2}\right)^2 \tag{9}$$

Figures 2 and 3b show that the spread of data becomes progressively greater with longer burn times and smaller values of $\rho/\rho_o$ for the reasons discussed in Section III-A. It is possible that a better correlation could be found to represent the last phases of burning; however, from the point of view of firebrand hazard this phase is of lesser importance since only a few percent of the initial mass remains to be burned.

From the volume measurements, it appears that there is only a small change in sample cylinder diameter while burning in still air. Consequently, in the calculations of mass change for ground burning it can be assumed that it is constant, and mass will vary proportionally to the density. Calculation performed on this basis is compared against test data in Fig. 5. The loss of weight of the sample during ignition accounts for the difference between the two curves, although their slopes are similar. The calculated curve assumed that the rate of mass loss during ignition follows the exponential law established for the burn process.

The assumption of no significant change in firebrand size during ground burning is also extended to firebrands which burn on the ground after flight. The diameter calculated at the time of impact will remain substantially unchanged during the subsequent ground burning in still air.

2. Burning in Wind

The in-wind burning data are shown in Figs. 6a and 6b. The empirical equation derived is similar to the still air equations assuming $\rho_c \sim 0$ (i.e., the firebrand completely burns up)

$$\frac{\rho}{\rho_o} = e^{-\frac{t}{D_o^2 \cdot k}} \tag{5a}$$

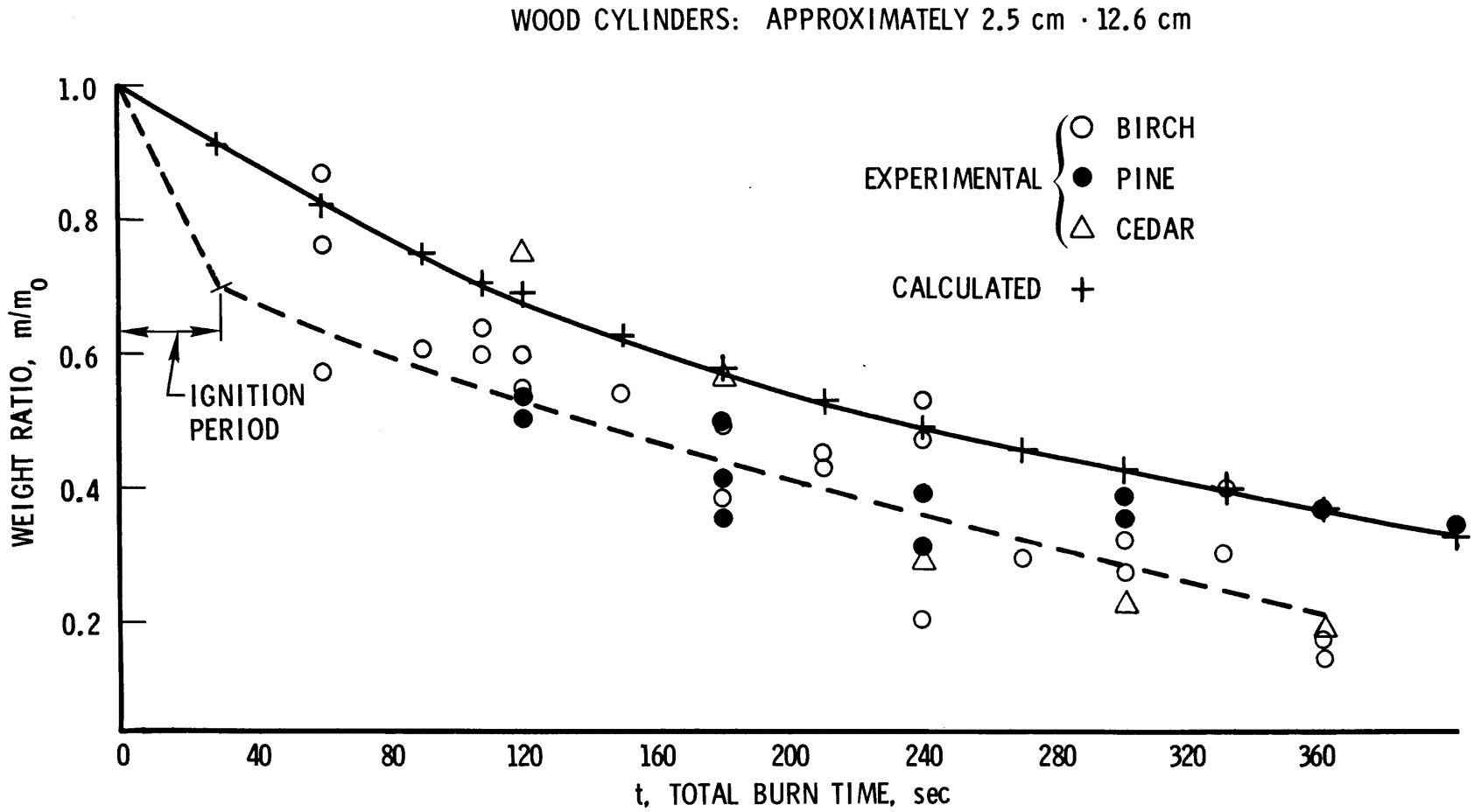


Fig. 5. Comparison of Experimental and Calculated Values for Weight Ratio of In-Still-Air Burning Firebrands

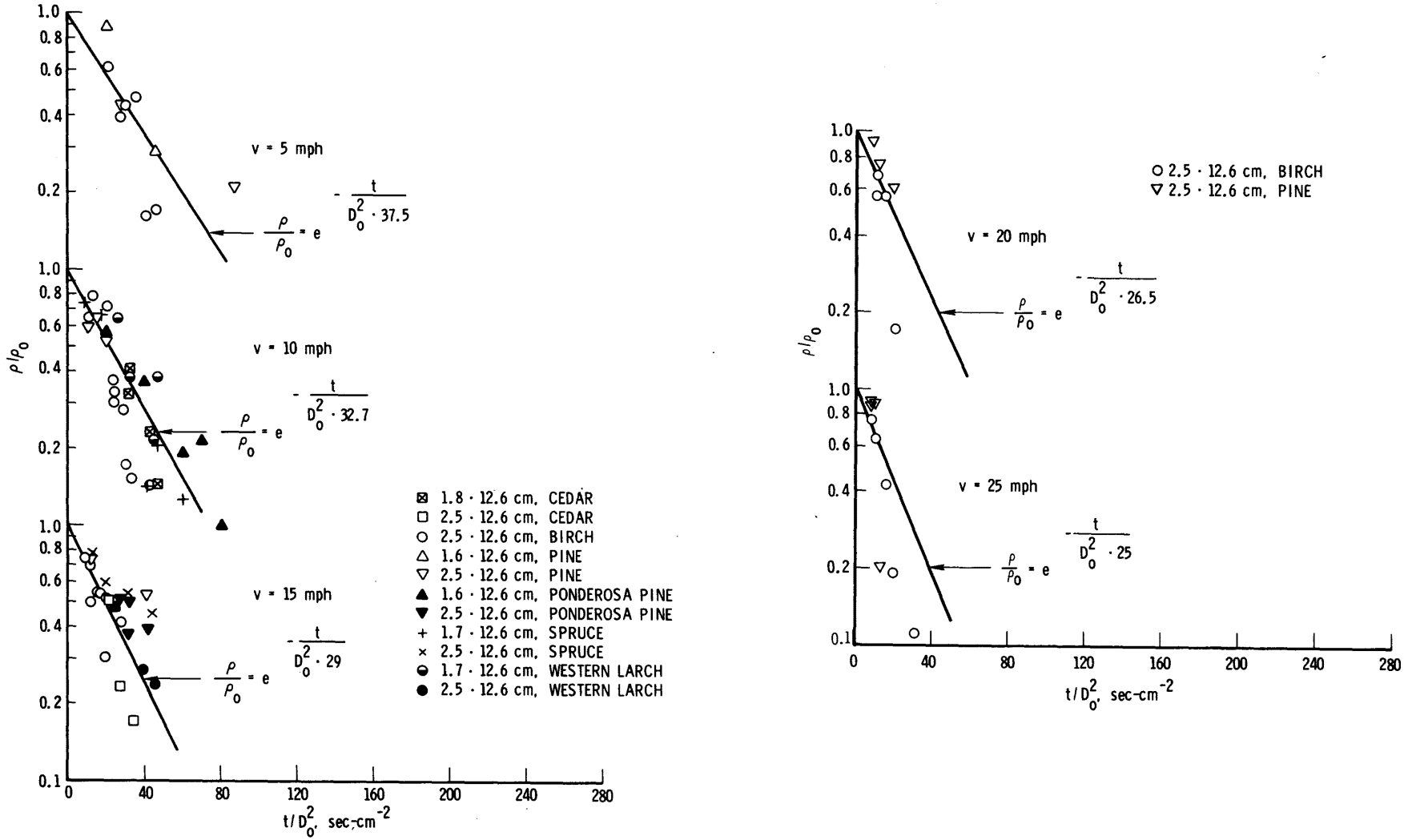
v = 5 mph
$\frac{\rho}{\rho_0} = e^{-\frac{t}{D_0^2 \cdot 37.5}}$
v = 10 mph
$\frac{\rho}{\rho_0} = e^{-\frac{t}{D_0^2 \cdot 32.7}}$
v = 15 mph
$\frac{\rho}{\rho_0} = e^{-\frac{t}{D_0^2 \cdot 29}}$
v = 20 mph
$\frac{\rho}{\rho_0} = e^{-\frac{t}{D_0^2 \cdot 26.5}}$
v = 25 mph
$\frac{\rho}{\rho_0} = e^{-\frac{t}{D_0^2 \cdot 25}}$
$\rho/\rho_0$
$t/D_0^2$, sec-cm$^{-2}$
1.8 · 12.6 cm, CEDAR
2.5 · 12.6 cm, CEDAR
2.5 · 12.6 cm, BIRCH
1.6 · 12.6 cm, PINE
2.5 · 12.6 cm, PINE
1.6 · 12.6 cm, PONDEROSA PINE
2.5 · 12.6 cm, PONDEROSA PINE
1.7 · 12.6 cm, SPRUCE
2.5 · 12.6 cm, SPRUCE
1.7 · 12.6 cm, WESTERN LARCH
2.5 · 12.6 cm, WESTERN LARCH
2.5 · 12.6 cm, BIRCH
2.5 · 12.6 cm, PINE

Fig. 6. Density Change of Burning of Oven-Dry Wood Cylinders, Wind Velocity, v

with the exponential constant k calculated for each wind velocity as the mean of all test data available. The coefficient of variation (standard deviation/mean) was in the range of 30 to 40% for most of the constants. The greatest divergence between the proposed correlation and the test data occurred at 25 mph and low values of $\rho/\rho_o$. However, this regime has little application to burning firebrands, since once they burn down to low values of $\rho/\rho_o$ their free fall velocity will be of the order of 5, not 25, mph. Furthermore, it is desired that the correlation established will give a rather conservative prediction of the burn rate; thus the slopes of the curves for 15, 20 and 25 mph are less steep (larger k) than could be obtained from a better fit of data.

To establish analytically the effect of wind velocity on the burn rate (rate of density change), a linear regression method was applied to values of exponential constants k previously defined. The result of this calculation for cylindrical firebrands is shown in Fig. 7 with k defined as

$$k = 43.3 - 1.28v + 0.022v^2 \ldots \quad (10)$$

where v is wind velocity in mph. This equation indicates that k will be minimum or the burn rate maximum when $v \sim 29$ mph. With higher wind velocity, the burn rate will be decreasing. No tests were carried out because of tunnel limitation to check this, but it may be of interest to verify this conclusion in some future tests.

To compare the prediction of a firebrand weight loss during burning, calculation was made for a birch cylinder of 2.5 cm diameter and 12.6 cm length in a free flight using the equations developed and experimental data on burning at constant wind velocities.

The results were plotted in Fig. 8 against experimental data for the same cylinder at 5 and 25 mph. The calculation is performed by using Tarifa's equations[5] to obtain the ratio $w_{(t)}/w_o$ (instantaneous to initial fall velocity) as a function of burn time. The ratio $\rho_{(t)}/\rho_o$ from the exponential equation (5a) shown earlier was obtained using appropriate values of k from Eq. (10)

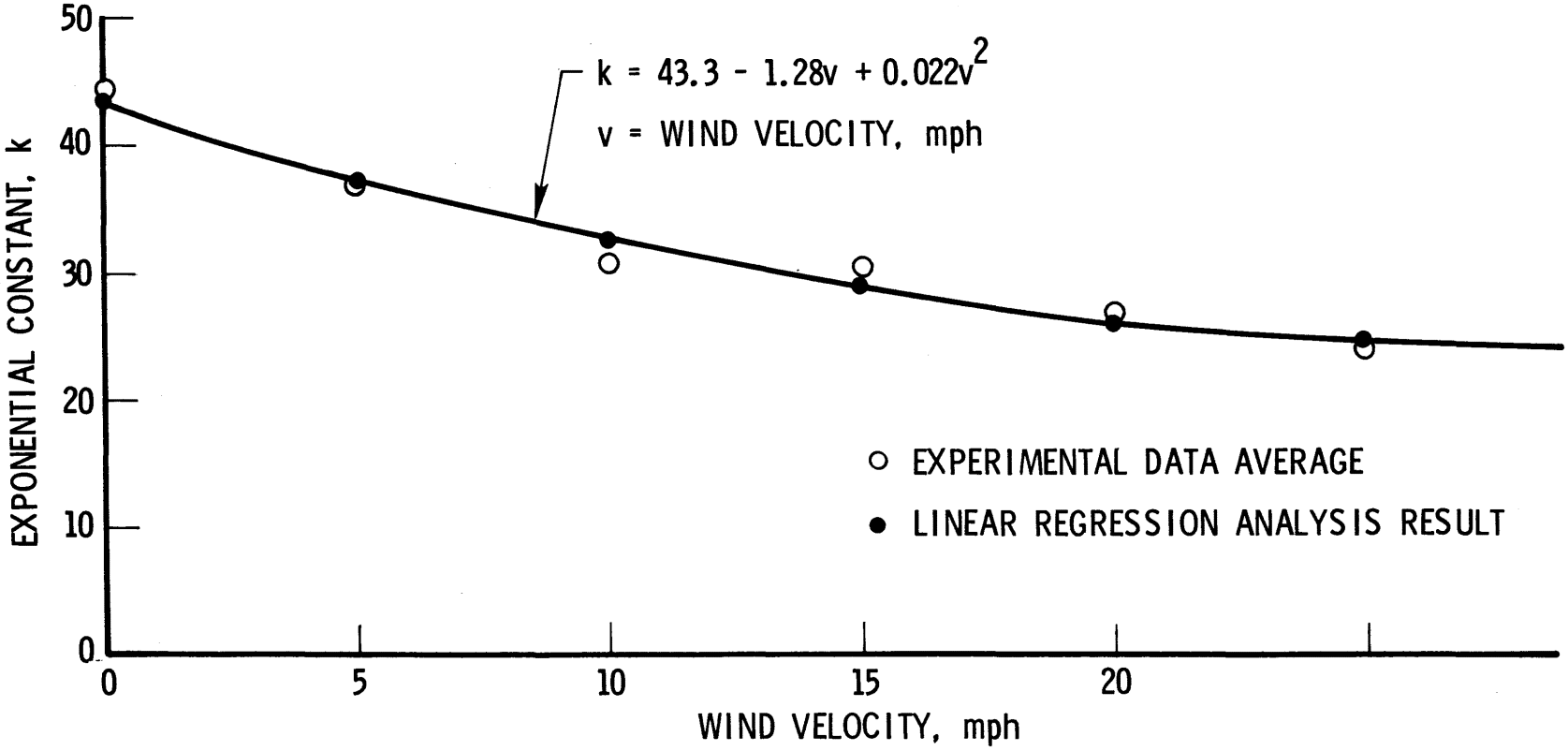


Fig. 7. Change in the Exponential Constant, k, with Wind Velocity

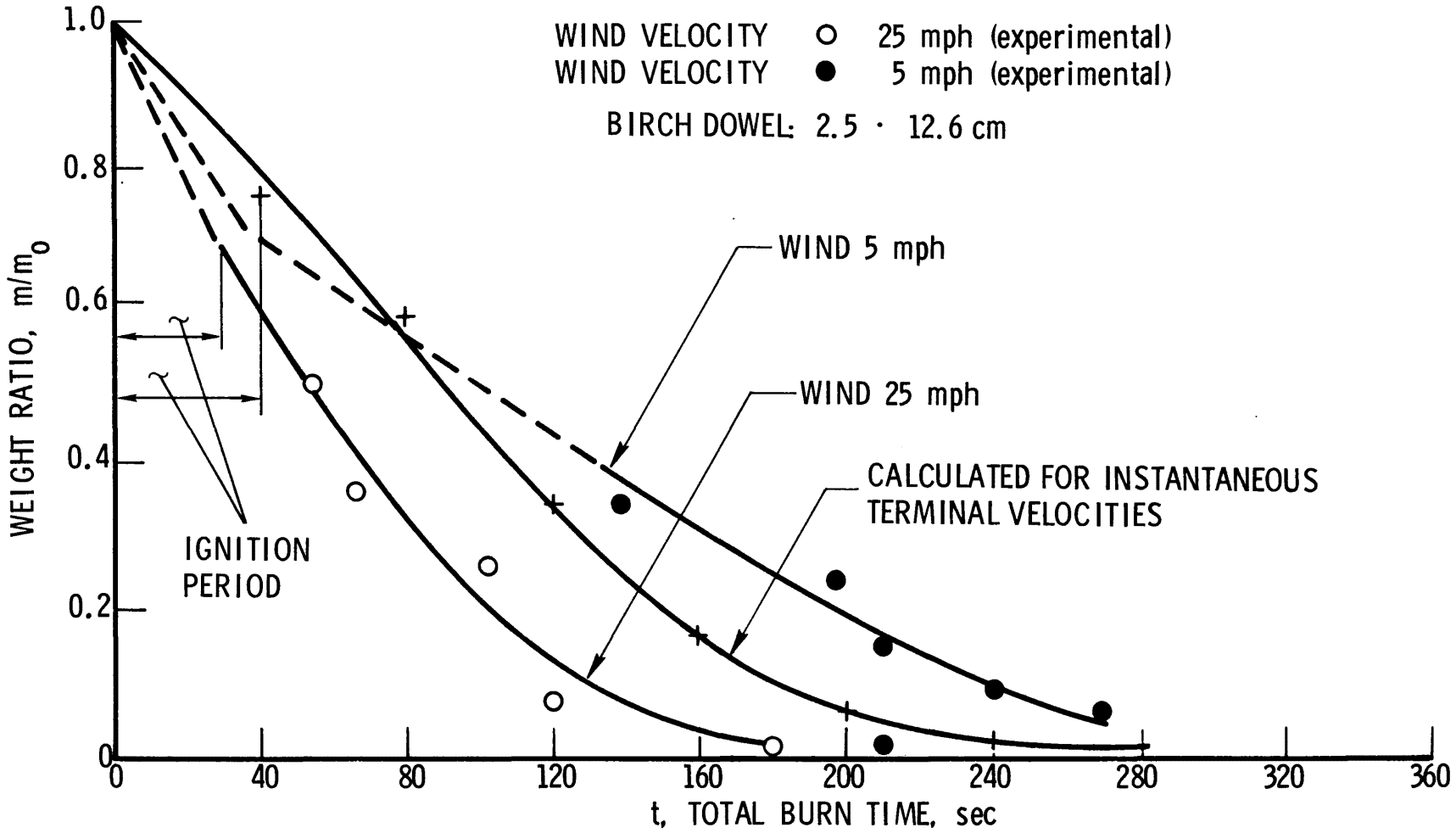


Fig. 8. Comparison of Experimental and Calculated Values for Weight Ratio of In-Flight Burning Firebrands

corresponding to instantaneous $w_{(t)}$. Then, the mass ratio $m_{(t)}/m_o$ could be calculated since

$$\frac{m_{(t)}}{m_o} = \left[\frac{w_{(t)}}{w_o}\right]^4 \cdot \frac{\rho_o}{\rho_{(t)}} \quad \ldots . \tag{11}$$

The calculated values should fall between the two experimental curves since, with the exception of the initial phase when the fall velocity was above 25 mph and the final burn phase when it is below 5 mph, the free fall velocities would be between the two values. Figure 8 confirms this, although in the initial phase the experimental data show a greater weight loss due to the ignition cycle.

Further verification of the equation developed was made by comparing the prediction of mass loss by burning with test data for firebrands which were burning in a wind tunnel at a constant wind velocity, then removed after various burn time periods and allowed to continue burning in still air for a predetermined period of time. These tests simulated a firebrand burning in flight and then continuing its burning after impact in what was assumed to be quiescent air. The weight of samples was measured after the total burn was completed; the weight ratio of final/initial weight obtained from calculations and from measurements is shown in Fig. 9.

The calculation was performed in the following manner: For a known time burn in the tunnel at known wind velocity, the density ratio $\rho/\rho_o$ was determined for the appropriate value of k from the equation

$$\frac{\rho_{f\ell}}{\rho_o} = e^{-\frac{t_{f\ell}}{D_o^2 \cdot k}} \tag{12}$$

where $\rho_{f\ell}$ is the sample density at termination of in-wind burning during time $t_{f\ell}$.

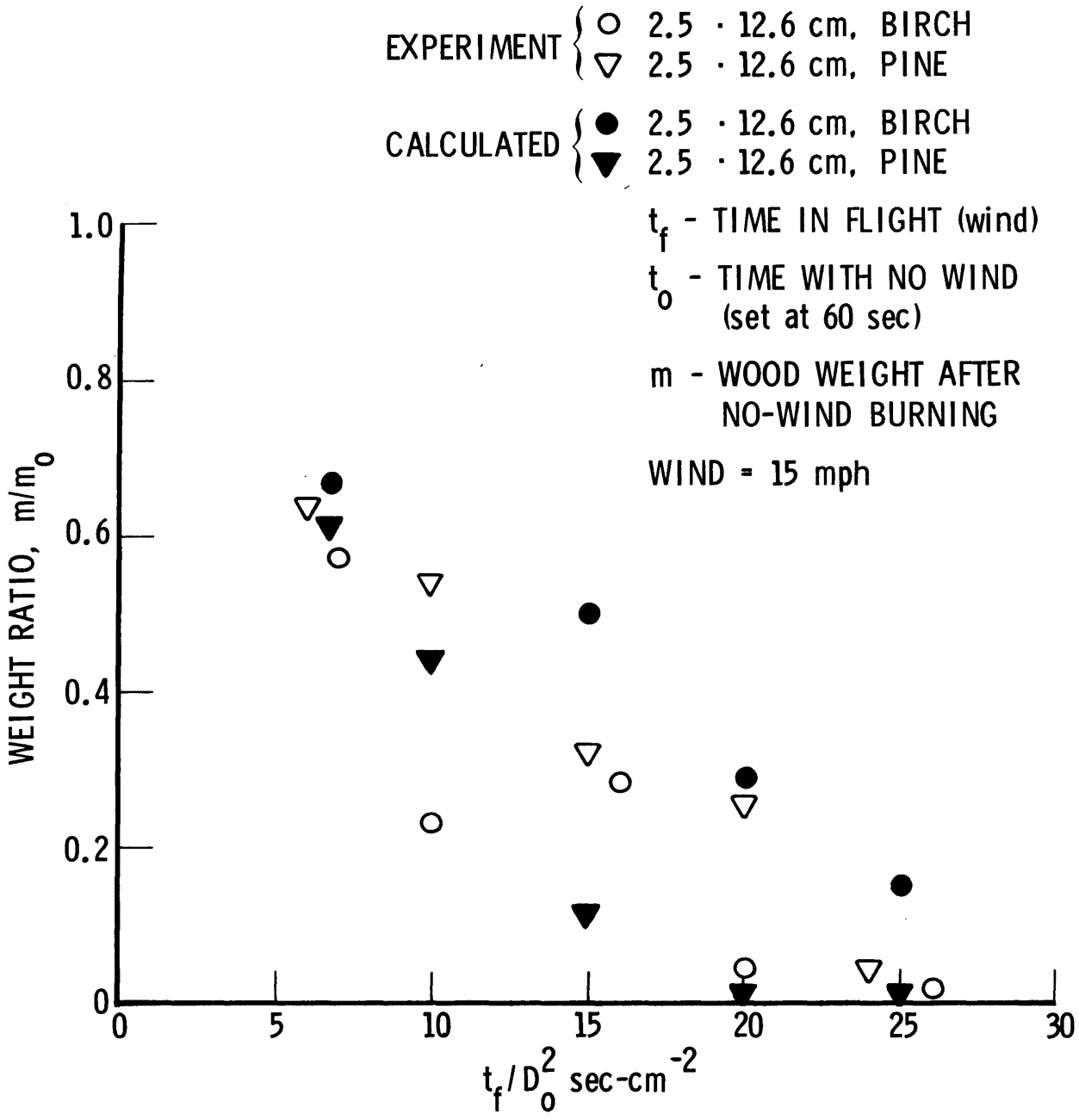


Fig. 9. Simulated Firebrand Burning After Impact

The sample diameter $D_{f\ell}$ (in cm) at that time was determined by using Tarifa's data for the fall velocity ratio and then applying Eq. (2).

The firebrand continues burning on the ground with unchanging diameter $D_{f\ell}$, and the average sample density $\rho$ at the end of ground burning can be calculated from

$$\frac{\rho - \rho_c}{\rho_{f\ell} - \rho_c} = e^{-\frac{t_o}{D_{f\ell}^2 \cdot 43.3}} \tag{13}$$

where $\rho_c$ is the final average sample density (when allowed to burn to extinction) corresponding to diameter $D_{f\ell}$ and calculated from Eq. (8). The time $t_o$ (in sec) is the specified time of burning on the ground.

Finally, the weight ratio can be obtained from the equation

$$\frac{m}{m_o} = \left(\frac{D_{f\ell}}{D_o}\right)^2 \cdot \frac{\rho}{\rho_o} \tag{14}$$

The agreement between the calculated and the experimental data appears reasonable.

The results of flat plate burning in wind are shown in Fig. 3a. The plates were placed in the tunnel with the wind velocity vector parallel to the plate surface. Burning took place at the leading edge, and there was negligible change in plate thickness as the burning progressed. The formulas in Fig. 3 are valid for square or near-square plates with $L/h_o \leq 20$. Plates with high $L/h_o$ ratio will experience very small, if any, change in the average density with burning time. Flat plates of Ponderosa pine bark were also burned and these showed even lower rates of burning than those in Fig. 3a.

To obtain an expression for the change in the exponential constant with wind velocity, a quadratic relationship similar to that for cylinders [see Eq. (10)] was assumed. Since experimental data for 0 and 10 mph were available and observation was made that flat plate maximum burning rate occurs between 20 and 30 mph (Figs. 3a, 3b), an equation was derived

$$k_{plates} = 126 + 86.5v - 1.73v^2 \tag{15}$$

where v is wind velocity in mph.

The observation that the flat plate thickness does not vary during the burning process, coupled with Tarifa's observation[5] that the drag coefficient of a burning firebrand remains constant and the average drag force of a tumbling firebrand can be assumed as equal to the maximum drag orientation value, leads to a conclusion that the instantaneous fall velocity of flat plates will be defined by

$$\frac{w_{(t)}}{w_o} = \left[\frac{\rho_{(t)}}{\rho_o}\right]^{1/2} \tag{16}$$

To calculate the mass of a plate-shaped firebrand on impact, measurements were made of the rate of volume change (equal to the rate of area change at a constant thickness), and the data are presented in Figs. 10a and 10b. Reasonable correlation results from

$$\frac{A}{A_o} = e^{-\frac{t}{h_o \cdot (k)^{1.24}}}$$

where t is in sec, $h_o$ is plate thickness in cm, and k is an exponential constant equal to 126 at 10 mph wind. However, linear regression gives a better fit of

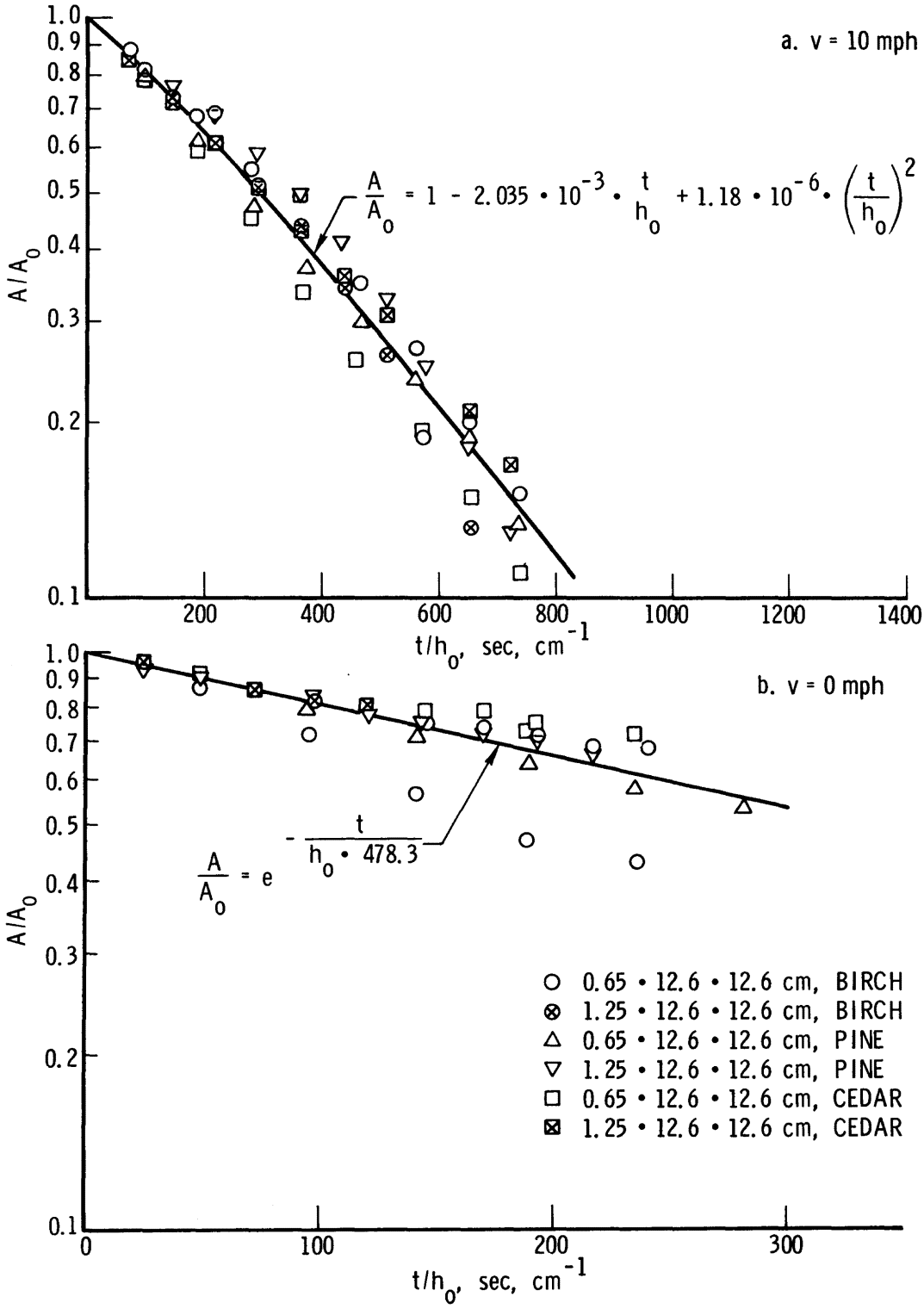
a. v = 10 mph
$\frac{A}{A_0} = 1 - 2.035 \cdot 10^{-3} \cdot \frac{t}{h_0} + 1.18 \cdot 10^{-6} \cdot \left(\frac{t}{h_0}\right)^2$
A/A0
t/h0, sec, cm-1
b. v = 0 mph
$\frac{A}{A_0} = e^{-\frac{t}{h_0 \cdot 478.3}}$
0.65 • 12.6 • 12.6 cm, BIRCH
1.25 • 12.6 • 12.6 cm, BIRCH
0.65 • 12.6 • 12.6 cm, PINE
1.25 • 12.6 • 12.6 cm, PINE
0.65 • 12.6 • 12.6 cm, CEDAR
1.25 • 12.6 • 12.6 cm, CEDAR

Fig. 10. Area (Volume) Change of Burning Oven-Dry Wood Plates

data as given by

$$\frac{A}{A_o} = 1 - 2.035 \cdot 10^{-3} \cdot \frac{t}{h_o} + 1.18 \cdot 10^{-6} \cdot \left(\frac{t}{h_o}\right)^2 \qquad (17)$$

where t is in sec and $h_o$ in cm.

For on-ground burning (see Fig. 10), exponential correlation appears satisfactory

$$\frac{A}{A_o} = e^{-\frac{t}{h_o \cdot 478.3}} \qquad (18)$$

with t in sec and $h_o$ in cm.

Note that 0.65 cm birch plates burn faster than the others but, consistent with the conservatism of our approach, the correlation was based on slower burning samples. Thus, knowing the relationship for density and area change, the mass of a burning plate can be calculated.

The lower rate of flat plate burning coupled with a low density of bark material (typically $0.2 g/cm^3$) allows burning bark to fly large distances (see Fig. 25) and makes it one of the most hazardous firebrand materials. Cheny and Bary[4] stated, for instance: "The bark characteristics of some eucalypt species provide them with a spotting potential unequalled by any other forest type, both in the distance that burning embers are carried and in the number of ignition points per unit area. Spotting distances of 5 to 6 miles are common on many high intensity eucalypt fires and well authenticated spot fires 12 to 15 miles in advance of the main fire front were recorded in Victoria and New South Wales during the January 1939 fires."

3. Effect of Relative Air Humidity

To establish the effect of relative air humidity, wind tunnel tests were run at 10 and 15 mph with humidities of 15, 35, 45 and 55%. Samples of birch and pine material were oven-dried before the test, and it can be assumed that no additional moisture was absorbed by the samples during the short pretest and test time intervals.

Within the spread of experimental data no effect of air humidity on the burning rate was observed. Therefore, it can be assumed that in real life relative air humidity will have only indirect effect by increasing or decreasing fuel moisture content. The effect of fuel moisture is discussed below.

4. Effect of Fuel Moisture

The effect of fuel moisture was studied with respect to the ignition time and to the fuel burning rate. The samples tested were either oven-dry (typically 2% moisture) or preconditioned to ~4% and ~9% moisture. The ambient air conditions were: 25% relative humidity and 85°F temperature.

The ignition time with the same ignition source was unaffected with moisture content up to 4% and was the same as for oven-dry fuels. However, for the 9% moisture content an increase of the ignition time of 50% (from 30 to 45 sec) was observed. The increase of ignition time with increased fuel moisture is to be expected and was experimentally evaluated by Fons[8] and analytically evaluated by Muraszew[1]. The fact that no apparent increase was observed at approximately 4% fuel moisture was probably due to an experimental error in assessment of fuel ignition since the predicted ignition time difference would be of the order of a few seconds only. On the other hand, 50% increase in ignition time for 9% moisture is in agreement with data presented by Muraszew[1].

The change in the burn rate with moisture content of fuel is shown in Fig. 11. The data are scattered, but in all conditions a slowing in the burn rate at 9% moisture content was observed.

Figure 12 shows a proposed correlation of the test data expressed as a change in the exponential constant k

$$k_{(M)} = \frac{k_{(M=2)}}{1.35} \cdot M^{0.44} \qquad (19)$$

where M is fuel moisture content in percent and $k_{(M=2)}$ corresponds to an oven-dry fuel with moisture content approximately 2%. Note that when M = 2%, $k_{(M)} = k_{(M=2)}$.

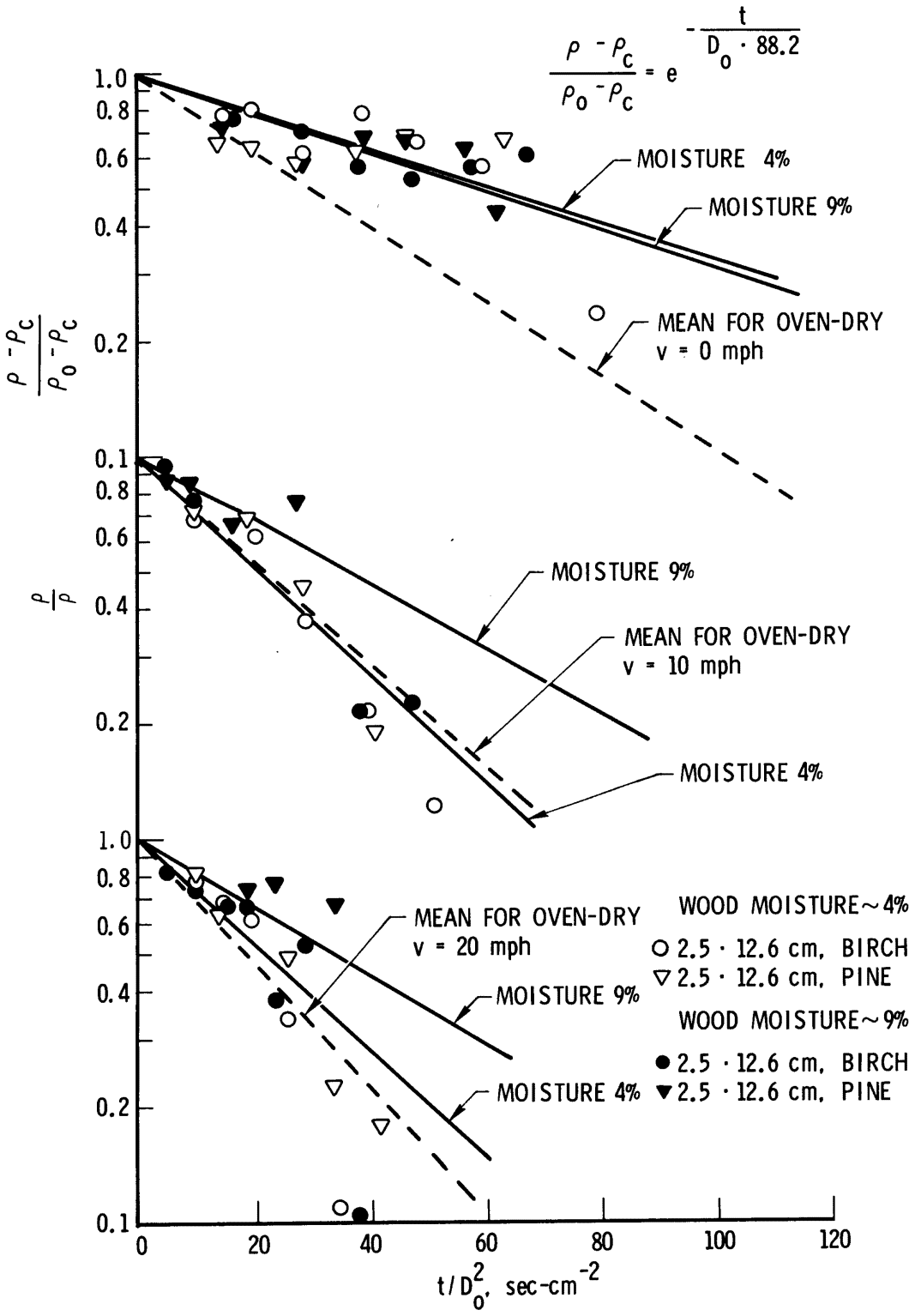


Fig. 11. Effect of Wood Moisture on Burning Rate

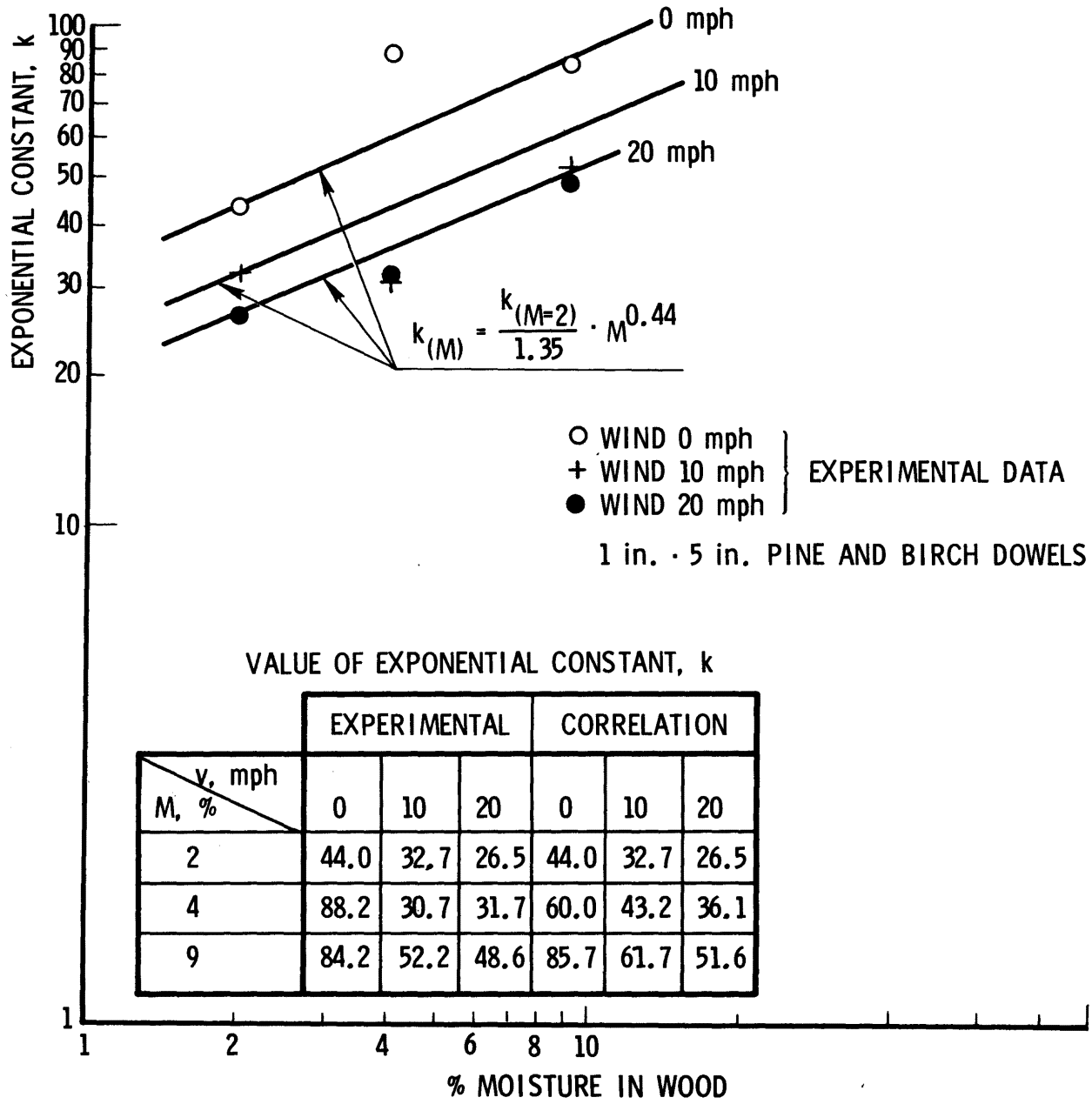


VALUE OF EXPONENTIAL CONSTANT, k

| | EXPERIMENTAL | | | CORRELATION | | |
|---|---|---|---|---|---|---|
| V, mph / M, % | 0 | 10 | 20 | 0 | 10 | 20 |
| 2 | 44.0 | 32.7 | 26.5 | 44.0 | 32.7 | 26.5 |
| 4 | 88.2 | 30.7 | 31.7 | 60.0 | 43.2 | 36.1 |
| 9 | 84.2 | 52.2 | 48.6 | 85.7 | 61.7 | 51.6 |

Fig. 12. Correlation Between Experimental and Analytical Expression for the Effect of Moisture on Wood Burning Rate

It was also observed in wind tunnel tests that oven-dry fuels or fuels with moisture content up to 4% burned up completely ($\rho_c \sim 0$), but fuels with 9% moisture content stopped burning at different wind speeds with up to 50% of the weight still remaining. This effect of fuel moisture was not further investigated quantitatively.

It appears, therefore, that fuels with approximately 10% moisture or more will not form good firebrands because of the longer ignition time required, lower burning rate as compared to dry fuels, and a tendency for premature extinction.

5. Flaming Versus Glowing Combustion

The combustion process of firebrands can result either in flaming or in glowing combustion. It is important to know, in determining the recipient fuel ignition, whether the firebrand will be flaming or glowing on impact and in ground burning.

a. In Still Air

In Ref. 1, the problem of flaming versus glowing ignition was discussed and an empirical formula for firebrand flaming in still air was derived in the form $t_{f\ell} = 80 \cdot D_o^{1.25}$ where $t_{f\ell}$ is flaming time in sec and $D_o$ is initial firebrand diameter in cm. Further experimental work performed at the NFFL indicated a great spread in flaming time even for the same type and size of wood. For the various woods tested (birch, pine, Ponderosa pine, Western larch, cedar, spruce), in cylindrical shapes of approximately 1 in. diameter and 5 in. long, the flaming time in still air was between 3 and 5 min. For similar wood cylinders of 1/2 in. diameter and 5 in. long, the flaming time in still air was between 2 and 3.5 min. There was still a dependence on the sample size, but it was not as strong as indicated by the above equation.

Burning of flat plates of birch, pine and cedar 1/4 and 1/2 in. thick in still air has shown a small dependence of flaming time on plate thickness but larger dependence on the type of wood. The flaming time for pine plates was 2.5 to 4 min. and for birch and cedar from 1 to 2.5 min. The orientation of

the wood grain with respect to the burning edge would probably have a significant effect on plate burning, although this was not investigated experimentally.

b. In Wind

The observations have shown that burning in wind reduces the flaming time in almost all of the tests performed. This is to be expected. Increased air flow velocity around a burning sample increases the heat transfer rate into the solid, thereby increasing the burn rate, but it also dilutes the products of pyrolysis. The mixture of air and gases becomes too lean to sustain flaming combustion as soon as the rate of mass loss is below some critical value. The higher the air velocity, the shorter was the flaming time. At 10 mph wind, the flaming time was reduced by a factor of 2 to 5 when compared with still air burning, and at 20 mph none of the samples continued flaming after the igniter was withdrawn, although they continued glowing until all material was consumed.

From the above data, some conclusions can be drawn regarding the combustion mode of firebrands in flight. From the work of Tarifa[5] and the trajectory analysis presented in Section IV-D-3 of this report, it appears that when a firebrand is ejected out of a fire whirl or from any convection column it reaches ambient wind velocity within a few seconds. That is, the firebrand moves with the wind except that it has a relative vertical velocity equal to its instantaneous terminal velocity. It is, therefore, this velocity which will affect the flaming time of a firebrand, assuming that it is initially ignited to a flaming stage.

The initial free fall velocity of various wood samples is shown in Table 1. It can be seen from this table that firebrands will be flaming only for a short time in flight and for the trajectories shown, for instance, in Section IV-D-3, all will be in a glowing stage at impact.

Table 1. Fall Velocity of Wood Samples (Oven-Dry)

| Shape | Diameter or Thickness, in. | Wood Type | Wood Density, $lb/ft^3$ | Initial Fall Velocity, mph | Probable Flaming Time, min |
|---|---|---|---|---|---|
| Cylinder | 1 | Pine | 25 | 23.0 | 0 |
| | 1 | Birch | 41 | 29.7 | 0 |
| | 1/2 | Pine | 25 | 16.4 | < 0.5 |
| | 1/2 | Birch | 41 | 21.0 | 0 |
| Flat Plate | 1/4 | Cedar | 20 | 11.7 | < 1.5 |
| | 1/4 | Pine | 25 | 13.1 | < 1.0 |
| | 1/4 | Birch | 41 | 16.7 | < 0.5 |

c. After Impact Burning

To reproduce the conditions of firebrand burning after impact, a series of tests was performed at the NFFL in which wood samples were burning in the tunnel and then removed from the tunnel after various in-wind burning periods, varying from 30 to 210 sec, to continue burning in still air. An interesting phenomenon was observed in that most of the samples glowing in the tunnel, when removed from the wind, burst into flames for a short period of 1 to 5 sec and resumed glowing to extinction at some remaining weight which was a function of initial size of the sample and in-wind burning time. This phenomenon could be reproduced two or three times on any one sample by returning it to the wind tunnel and then removing it into the still air. If a firebrand with such characteristics impacts into recipient fuel composed of fine, dry particles or punkie wood, the probability of starting a fire will be high.

The method for calculating post-impact burning time and burn rate is shown in Section III-C-2. For calculation of post-impact burn time to practical extinction, an assumption can be made that $\rho = 1.2\rho_c$ (see Fig. 4) and the time can be calculated from Eq. (13) where $\rho$ represents a condition of very low rate terminal burning.

d. Moisture Effect on Flaming Time

The effect of moisture on flaming time was investigated experimentally on 1-in. pine and birch dowels preconditioned to 3 to 4% and 8 to 9% moisture burning in still air and at 10 mph wind.

Increase in wood moisture reduced the flaming time as expected. At 10% moisture, the flaming time in still air was reduced by a factor of approximately 2 when compared with oven-dry wood. The moisture effect was even more pronounced for in-wind burning. No flaming at all, or very short flaming of 1 sec only, was observed at either 3 to 4% or 8 to 9% moisture. This observation confirms the statement previously made as to a reduced firebrand fire hazard with higher moisture fuels.

# IV. ANALYSIS OF FIRE WHIRL AND FIREBRAND INTERACTION

## A. GOALS

This section is concerned with the prediction of fire whirl fluid mechanical properties, the lifting of firebrands within the core, and their subsequent trajectories. The methodology employed to model the core was presented earlier in Ref. 2. While the fire whirl analysis presented there was applicable to liquid fuels (e.g., acetone), the extension to wood fuels is direct. However, in order to make this present report self-contained, the main features of the approach, as applicable to wood fuels, will be presented here.

Fire whirls are tornado-like regions of hot, swirling gas which can be generated by intense fires. In the absence of swirl, large fires create thermal convection columns of hot, rising air. This upward flow is maintained by a horizontal flow of air into the column driven by the small pressure differential between the hot, buoyant column and the surrounding air. This inflow, as well as turbulent diffusion, along the vertical extent of the column rapidly diffuses the column, limiting its height and upward gas velocity.

However, in the presence of ambient circulation, or vorticity, the centrifugal force, due to the circulation, limits any bulk motion into the column. Meanwhile, the ambient vorticity is initially turbulently mixed into the column, creating a thin, swirling core which then inhibits the turbulent diffusion at the core-ambient air boundary. Thus, the steady-state core can be concentrated into a long, narrow core of swirling hot gas. This vortex core region can be maintained by the influx of air into the core from the ground boundary layer with little influx of ambient air along its vertical extent. Above the ground, the centrifugal forces balance the radial pressure gradient and prevent the inflow of air into the core. Very near the ground, the swirling motion is inhibited. The radial pressure gradient which is impressed onto the ground boundary layer is thus unimpeded within the boundary layer and produces a radial inflow of ground boundary layer air (and fuel) into the core, thus maintaining a high upward flow within the core.

Since the core spreading is inhibited by the ambient circulation, large uplift velocities are maintained up to large heights. Thus, fire whirl uplift velocities can be much higher than those of a conventional convection column because the presence of ambient circulation induces a strong radial inflow of mass at the ground into the vortex core and also inhibits the spreading and weakening of the core.

The large vertical velocities associated with a full-scale fire whirl can cause burning debris (firebrands) to be lifted up into the core. The firebrands that are light enough to be lifted to large heights in the core can penetrate the upper boundary of the core or be centrifuged out the side of the fire whirl, where they can be carried far away from the fire area by the prevailing winds, often forming another fire front.

The objective of the work of this section is to analytically characterize the fire whirl parameters which are relevant to the uplift of firebrands and to predict their ensuing trajectories. Included in the determination of the trajectory of a burning firebrand is the prediction of where it will land (or whethe it burns up in flight) and its density and size upon landing. The goal is to obtain this characterization in terms of quantities which would be available to fire managers in the field.

The quantities which determine the properties of the fire whirl, and thus are the controlling variables for the generation of firebrands, are the properties of the burning fuel, and the strength and size of the ambient circulation. The characterization of the firebrand trajectory also depends on the location (radial position) within the core where the firebrand is uplifted and on the prevailing winds. It is anticipated that subsequent studies will provide for statistical determination of the strength and vertical extent of the ambient circulation and its probability of generating a fire whirl in terms of terrain, fuel, and wind conditions. Using this type of information, the current model may then be used to predict the probable landing location of dangerous firebrands. Coupling this with the probability of incipient fuel ignition results in a statistical model for the prediction of spot fires.

The fire whirl and firebrand trajectory models are developed in Sections IV-B and IV-C, respectively, and are correlated with the subscale experiments conducted at the University of California, Santa Barbara (UCSB), reported in Section V. Two parameters inherent in the analytical fire whirl model are obtained experimentally using the UCSB data. The analysis is then applied to full-scale whirls, and calculations for a wide range of the input variables which characterize the core are given in Section IV-D-2. Firebrand trajectories for various firebrand sizes, shapes, and density are given in Section IV-D-3.

## B. FIRE WHIRL ANALYTICAL MODEL

The occurrence of a fire whirl depends on the presence of ambient vorticity, an intense fire which creates a rising hot column that interacts with the ambient vorticity to form a vortex core, and the presence of a ground plane which slows the rotational motion of the swirling ambient air and thus allows a radial mass inflow within the ground boundary layer to feed the vortex core.

The fully coupled fire whirl problem is very complex. Past fire whirl analyses have circumvented attack of the fully coupled problem by solving for the core's properties[9] or their radial average[10] in terms of their unknown values near the ground (just above the ground boundary layer). Thus, both studies eliminated the need for coupling the ground boundary layer and fuel surface heat transfer to the core flow.

Both Lee[9] and Emmons and Ying[10] conducted laboratory fire whirl experiments (using acetone and Bunsen burner exhaust gases, respectively, as the fuel) from which these unknown values at the core base could be obtained. However, while these core base parameters can be measured readily in a controlled laboratory experiment, they are not available to fire managers in the field.

The purpose of this current effort is to obtain a model in a form which is easy to use in the field and which requires only inputs which the fire manager can readily obtain. While the coupling between the ground boundary layer, fuel heat transfer, and the core flow must be considered in order to obtain a self-contained fire whirl theory, a high degree of numerical accuracy is not required. Reasonable estimates of the core properties (such as the upward gas velocity) are acceptable. This allows various simplifications to be introduced into the analysis in order to make the problem tractable. The pertinent physical processes are retained, but the mathematical description of these processes is simplified where appropriate.

The approach used for wood as the fuel is essentially the same as for acetone, as described in Ref. 2. The main features will be presented here in order to make the present report self-contained. The reader may refer to the earlier report for additional details.

The fire whirl geometry and nomenclature are shown in Fig. 13. The defining parameters are the ambient circulation $\Gamma$ (tangential velocity · radius) and its vertical extent $z_e$. These are taken as known parameters in a given problem. This swirling region outside the fire whirl is one of irrotational flow where there is no vertical velocity, $\Gamma$ is constant, and the swirl (azimuthal) velocity is independent of z and is given by $W = \Gamma/r$, for $r \geq a$. The fire whirl itself is assumed to be in solid body rotation (as, for example, in Ref. 6), where the rotation angular velocity $\omega$ is independent of r but is a function of height. Matching the azimuthal velocity at the fire whirl (e.g., core)-ambient air boundary (at $r = a$) at a given height gives $\omega = \Gamma/a^2$. Thus, the tangential (azimuthal) velocity inside the core is $W = r\omega = \Gamma r/a^2$, for $r \leq a$. The core radius a increases with height, and according to Byram and Martin[6]

$$\frac{a}{a_o} = \left(1 - \frac{z}{z_e}\right)^{-1/2} \tag{20}$$

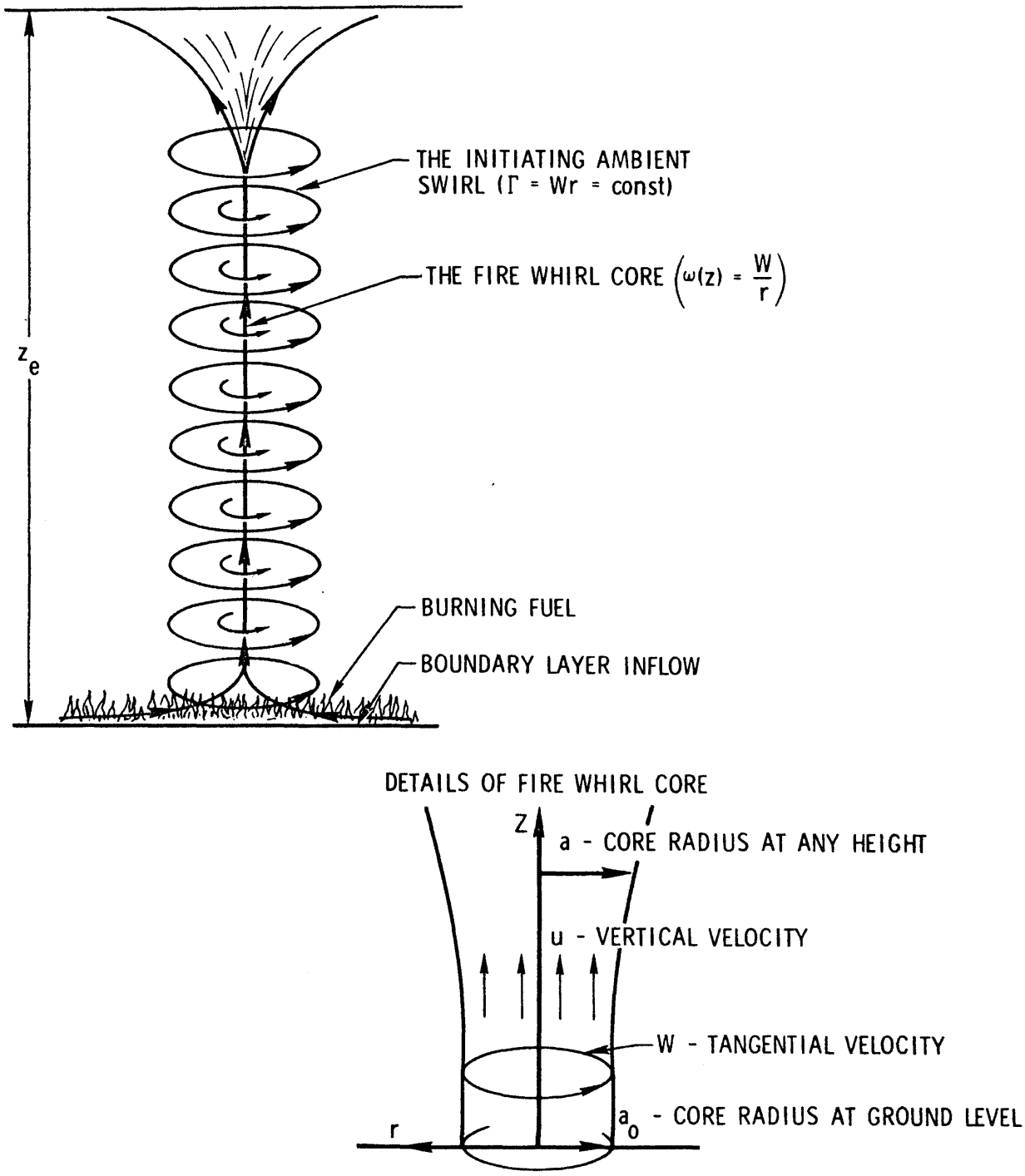
THE INITIATING AMBIENT SWIRL (Γ = Wr = const)
THE FIRE WHIRL CORE (ω(z) = W/r)
$z_e$
BURNING FUEL
BOUNDARY LAYER INFLOW
DETAILS OF FIRE WHIRL CORE
Z
a - CORE RADIUS AT ANY HEIGHT
u - VERTICAL VELOCITY
W - TANGENTIAL VELOCITY
r
$a_0$ - CORE RADIUS AT GROUND LEVEL

Fig. 13. Fire Whirl Geometry

where $a_o$ is the core radius at the ground just above the ground boundary layer. The Byram and Martin analysis, being a static model, did not include a method of obtaining the core vertical velocity u. This is obtained by incorporating the Byram and Martin results for W and a into the core fluid mechanics conservation equations.

The steady-state conservation equations are given below, in the cylindrical coordinate system shown in Fig. 13, with the variables having their usual fluid mechanical meaning.

Core mass conservation:

$$\frac{\partial}{\partial r} \rho r v + \frac{\partial}{\partial z} \rho r u = 0 \tag{21}$$

Core radial momentum equation:

$$\frac{\partial p}{\partial r} = \rho \frac{W^2}{r} \tag{22}$$

Core axial momentum equation:

$$\frac{\partial}{\partial z} \rho r u^2 + \frac{\partial}{\partial r} \rho r u v + \frac{\partial}{\partial z} p r + r \rho g = 0 \tag{23}$$

Equation of state:

$$p = \rho R_g T \tag{24}$$

The set of equations includes an overall conservation of mass equation, balancing the boundary layer mass inflow into the core and the mass loss by the burning fuel with the upward core mass flow. The burning fuel is further coupled to the core flow through the convective heat transfer at the fuel surface, which causes fuel ignition and combustion, and through an overall energy balance that relates the core temperature increase to the heat released by the combusting fuel. Before presenting these equations, it is instructive to first simplify Eqs. (21) through (24).

A major simplification results by solving for radially averaged core quantities. In terms of ultimately utilizing a fire whirl model for the statistical prediction of spot fires, radially averaged values of the core gas density and vertical velocity, for example, should suffice. Thus, the core conservation equations are radially integrated from the core centerline to the core-ambient air interface, removing the radial dependence from the equations and leaving only the height z as an independent variable.

Integrating Eq. (21) with respect to r from r = 0 to r = a, taking the outer ambient flow ($r \geq a$) to be a pure vortex flow, and neglecting lateral entrainment of the ambient circulatory air into the core results in

$$\int_0^a \rho r u dr = \text{constant} \tag{25}$$

From Byram and Martin[6], the axial mean density between the core base and the upper surface $z = z_e$ is practically constant. Assuming that the radial mean density is also constant

$$\rho = \overline{\rho} = \text{constant} \tag{26}$$

and assuming that a top-hat radial profile for u is appropriate (or that u is a radial mean average), then Eq. (25) results in

$$\rho u a^2 = \text{constant} \tag{27}$$

which, neglecting lateral entrainment, states simply that the mass flux through the core is constant (independent of z).

The degree of entrainment depends on the intensity of the ambient circulation and decreases rapidly with increasing values of $\Gamma$. The greater the circulation, the greater the centrifugal forces, and the smaller the steady-state turbulent diffusion of air across the core boundary. Emmons and Ying[10], employing the entrainment hypothesis of Morton, Taylor, and Turner[12], showed that entrainment decreases with increasing circulation.

For more details, the reader is referred to Ref. 2, particularly Fig. 11 of that report. For the values of $\Gamma$ associated with the current analysis, the uplift velocity through the major portion of the core height is not expected to be greatly influenced by entrainment. Thus, the effect of entrainment is neglected in the present analysis.

From Eq. (27), the core vertical velocity at a given height is given in terms of its initial value at the base of the core above the ground boundary layer $u_o$, as $ua^2 = u_o a_o^2$. Using Eq. (20)

$$\frac{u}{u_o} = 1 - \frac{z}{z_e} \tag{28}$$

Next, integrating Eq. (22) (the radial momentum equation), from a point r within the core to $r \to \infty$ and using the expressions preceding Eq. (20) for W within and outside of the core results in the following expression for the pressure in the core

$$p = p_\infty - \rho_\infty gz - \frac{\Gamma^2}{2a^2}(\rho_\infty + \rho) + \frac{\rho\Gamma^2}{2a^2}\frac{r^2}{a^2} \tag{29}$$

Radially integrating Eq. (23) from r = 0 to r = a, employing Eqs. (20) and (29), and neglecting the inertia term relative to the buoyancy and vortex pressure terms gives

$$(\rho_\infty - \rho)\, ga_o^2 = \frac{\rho_\infty \Gamma^2}{2z_e} \tag{30}$$

As shown in Ref. 2, this equation can also be deduced from the Byram and Martin[6] paper. For small z, the neglect of the inertial term relative to the vortex pressure field requires that $2(\rho/\rho_\infty)(u_o/W_o)^2$ be small compared to one. For the UCSB acetone tests previously reported, the value of this expression was approximately 0.1 to 0.2. For the wood tests reported in Section V of this report, the value is about 0.3. While not as small as in the

acetone tests, it is still less than unity. Although some error may result from this approximation, it should not be predominant. Emmons and Ying[10] show that the neglect of the inertia term results in a core radius variation of the form given by our Eq. (20), and that this variation is consistent with their experimentally measured core size growth over the upper portion of the core. The neglect of the inertia term appears to be a reasonable, useful, and consistent simplification.

The azimuthal momentum equation is not needed here and is not presented. It is redundant since, upon radial integration, it reproduces Eq. (27).

While the decrease in the core pressure from ambient is sufficient to influence the dynamic behavior of the fluid, its percentage change is small compared to the change in core temperature or density. Equation (24) can then be simplified to

$$\frac{T}{T_\infty} = \frac{1}{\left(\frac{\rho}{\rho_\infty}\right)\left(\frac{R_{g,T}}{R_{g,\infty}}\right)} \tag{31}$$

Furthermore, the changes in the core gas constant from $R_{g,\infty}$ are small, so that $R_{g,T}/R_{g,\infty}$ can be taken as unity. (For a stoichiometric mixture of air and wood particles, $R_{g,T}$ is less than $R_{g,\infty}$ by less than 2%, and by less than 1% for 100% excess air.) Thus, the temperature given by Eq. (31) is constant and is the core mean temperature. It is now convenient to introduce the remaining equations.

The use of constant mean core density and temperature facilitates the application of an overall core energy equation in which the energy released by the combusting fuel heats the rising core gases. Equating the increase in temperature of the rising core gases with the effective heat released by the combustion of the fuel results in

$$\pi\rho u_o a_o^2 \left(C_p T - C_{p_\infty} T_\infty\right) = \dot{M}_f Q_c \tag{32}$$

where $\dot{M}_f$, the fuel burn rate within the core with swirl ($lb_m$/sec), is one of the unknown variables in the problem. The $Q_c$ is the net heat of combustion of the fuel which is effective in heating the core gas (Btu/$lb_m$). A value of 7000 Btu/$lb_m$ was used in the calculations[13]. This includes the consideration that energy is required to pyrolyze the fuel and that some energy is lost due to radiation.

A separate energy balance relating the steady-state fuel ignition to the heat convected to the burning wood surface is employed. In the absence of swirl and wind, with the energy required for steady-state fuel ignition being supplied by the heat convection from the thermal convection column immediatel above the fuel

$$(T - T_s)h_o = \rho_b R_o Q_i$$

In the presence of swirl, with the energy required for ignition supplied by the swirling core just above the fuel

$$(T - T_s)h = \rho_b R Q_i, \qquad h = h_o + h_w$$

where

| | | |
|---|---|---|
| $T_s$ | = | fuel surface burning temperature ($\sim 1080^oR$ for wood) |
| $h$ | = | heat transfer coefficient with swirl (Btu/$ft^2$-sec-$^oR$) |
| $h_o$ | = | heat transfer coefficient without swirl (Btu/$ft^2$-sec-$^oR$) |
| $h_w$ | = | $h - h_o$ (see Note 1) |
| $\rho_b$ | = | bulk density of the wood fuel ($lb_m/ft^3$) |
| $R$, $R_o$ | = | linear burn rate of the fuel (ft/sec) in the presence of swirl and without swirl and wind, respectively (see Note 2) |
| $Q_i$ | = | effective heat of ignition of wood (250 Btu/$lb_m$) |

Note 1: The values h and $h_o$ are effective total heat transfer coefficients which include radiative terms. It is assumed that the radiative term is the same with and without swirl, so that the added contribution of swirl is the convective heat transfer coefficient $h_w$ (see Ref. 2, Appendix II).

Note 2: The term $\rho_b R_o$ is the rate of wood mass loss due to burning, per unit ground area, in a quiescent environment. Thus, $\rho_b R_o$, as used here, is a property only of the fuel, depending on the wood type, size, depth, and loading. In the UCSB subscale tests this rate is measured. In an actual full scale case the Rothermel formulation[3] can be used to calculate it. The fuel burn rate per unit area with swirl, $\rho_b R$, is one of the unknown variables in the problem.

When $h_o$ is eliminated one finds

$$\frac{R}{R_o} = 1 + \frac{h_w(T - T_s)}{\rho_b R_o Q_i} \tag{33}$$

The swirl contribution to the convection coefficient is related to the ambient circulation as follows: The heat transfer coefficient is defined in terms of the Stanton number $(S_t)^*$ by $h_w = \rho_\infty V_c C_p (S_t)^*$. The * signifies that the Stanton number is to be evaluated at the mean temperature between the core and the fuel surface $(T + T_s)/2$. The characteristic velocity $V_c$ is taken as the swirl velocity at the core-ambient air interface just above the fuel surface $V_c = \Gamma/a_o$. The Stanton number is related to the swirl variables by utilizing Reynolds' analogy between heat transfer (molecular energy transfer) and skin friction (molecular momentum transfer) which gives, for a Prandtl number $(P_r)$ near one, $S_t = (1/2)C_f P_r^{-2/3}$, where $C_f$ is the skin friction coefficient at the wood surface within the ground boundary layer. The skin friction coefficient is related to the wood surface shear stress $\tau_o$ by definition as

$$C_f = \frac{2\tau_o}{\rho_\infty V_c^2}$$

and

$$\tau_o = \nu\rho \frac{\partial W}{\partial z}\bigg|_{\text{at ground fuel surface}}$$

where the relevant velocity for determination of $\tau_o$ is the azimuthal component within the boundary layer at the wood surface. The boundary layer azimuthal velocity is related to the core variables by using a procedure similar to that employed in Schlichting[7] for the ground boundary layer developed by a constant $\omega$ flow above a ground plane. Introducing the nondimensional boundary layer vertical coordinate

$$\eta = \frac{z R_{e_c}^{1/2}}{d}$$

where, for our case of flow over wood sticks and brush

$$R_{e_c} = \frac{\left(\frac{\Gamma}{a_o}\right) d}{\nu}$$

where the characteristic Reynolds number $R_{e_c}$ for this flow is given by the characteristic core swirl velocity $\Gamma/a_o$, the characteristic wood fuel diameter d, and the kinematic viscosity $\nu$. In terms of $\eta$, the boundary layer velocity needed to determine $\tau_o$ is $W = \Gamma N(\eta)/a_o$, where $N(\eta)$ is a nondimensional boundary layer azimuthal velocity profile variable. Thus

$$C_f = 2\left(\frac{\rho}{\rho_\infty}\right)\left(\frac{\nu a_o}{\Gamma d}\right)^{1/2} N'(o)$$

and

$$St^* = N'(o)\left(0.5\,\frac{\rho}{\rho_\infty} + 0.5\,\frac{\rho_s}{\rho_\infty}\right)P_r^{*-2/3}\left(\frac{\nu_\infty a_\infty}{\Gamma d}\right)^{1/2}$$
$$\left[0.5\left(\frac{T}{T_\infty}\right)^{0.6}\frac{\rho_\infty}{\rho} + 0.5\left(\frac{T_s}{T_\infty}\right)^{0.6}\frac{\rho_\infty}{\rho_s}\right]^{1/2}$$

since $\rho^* = 0.5\rho + 0.5\,\rho_s$, and the viscosity was taken to vary as the 0.6 power of temperature so that

$$\nu^* = 0.5\nu_\infty\left[\frac{\rho_\infty}{\rho}\left(\frac{T}{T_\infty}\right)^{0.6} + \frac{\rho_\infty}{\rho_s}\left(\frac{T_s}{T_\infty}\right)^{0.6}\right]$$

The temperature variation of the specific heat $C_p$ is given by

$$C_p = C_{p_\infty}\left(\frac{T}{T_\infty}\right)^{0.14}$$

Equation (33) is written specifically for the case of constant molecular properties; the variation of $C_p$ is also incorporated into Eq. (33) by considering the static enthalpy ($C_pT$) difference instead of the temperature difference.

The value of N'(o) from Schlichting for the case of a rotating flow over the ground, with no burning or combustion, is about 0.76. For the present case of burning near the ground plane and a hot buoyant core, it is expected that the vertical gradient of the characteristic azimuthal velocity will be different from the case considered in Schlichting. It will be considered an unknown parameter (dependent on $\Gamma$ and $\rho_b R_o$) to be determined from the experiments. If this parameter is called a' [instead of N'(o)], Eq. (33) becomes

$$\frac{R}{R_o} = 1 + \frac{a' C_{p_\infty} T_\infty \rho_\infty P_r^{*-2/3} \sqrt{\frac{\nu_\infty \Gamma}{2a_o d}}}{\rho_b R_o Q_i} \left[ \left( \frac{T}{T_\infty} \right)^{1.14} - \left( \frac{T_s}{T_\infty} \right)^{1.14} \right] \cdot$$

$$\cdot \left( 0.5 \frac{\rho}{\rho_\infty} + 0.5 \frac{\rho_s}{\rho_\infty} \right) \left[ \left( \frac{T}{T_\infty} \right)^{0.6} \frac{\rho_\infty}{\rho} + \left( \frac{T_s}{T_\infty} \right)^{0.6} \frac{\rho_\infty}{\rho_s} \right]^{1/2} \tag{34}$$

The set of equations is completed with the addition of an overall mass balance between the radially inward ground boundary layer flow into the core, the burning fuel mass loss into the core, and the upward core flow.

$$2\pi a_o \rho_\infty \int V_{BL} dz = \pi \rho u_o a_o^2 - \dot{M}_f \tag{35}$$

Following Schlichting's analysis for a constant $\omega$ flow over a fixed surface, the nondimensional profile variable $M(\xi)$ for the radial velocity $V_{BL}$ is introduced so that, at $r = a_o$, $V_{BL} = \Gamma M(\xi)/a_o$ where

$$\xi = \left( \frac{z}{a_o} \right) \sqrt{\Gamma / \nu_\infty}$$

Thus, the integral in Eq. (35) can be written as

$$2\pi a_o \rho_\infty \int V_{BL} dz = b' \pi \rho_\infty a_o \sqrt{\Gamma \nu_\infty}$$

where b' is the resulting integral of M. Again, the value of b' is expected to be modified from the constant value of 1.38 for the case presented in Schlichting. The velocity profiles in the hot, combusting ground boundary layer are expected to change as the fuel characteristics $\rho_b R_o$ and the swirl intensity $\Gamma$ change. The unknown parameter b' is also taken (as was a') to be a function of $\rho_b R_o$ and $\Gamma$ to be determined from the Section V experiments.

Equation (35) can now be written as

$$b'\pi a_o \rho_\infty \sqrt{\Gamma \nu_\infty} = \pi \rho u_o a_o^2 - \dot{M}_f \tag{36}$$

The mass loss rate of the burning wood $\dot{M}_f$, which appears in Eqs. (32) and (36), can be replaced by the variable R (or $\rho_b R$) since, by definition

$$\dot{M}_f = \rho_b R \pi a_o^2 \tag{37}$$

Equations (30) through (36), with Eq. (37), form a complete set for the unknowns $\rho$, T, $u_o$, $a_o$, and R (or equivalently, $\rho_b R$, or $\dot{M}_f$). These quantities are constant for given values of $\Gamma$, $z_e$, $\rho_b R_o$, and d, which are the primary input variables. The vertical profiles for a and u are given by Eqs. (20) and (28), respectively. The determination of the parameters a' and b' and the solution to this set of equations are given in Section IV-D-1.

## C. FORMULATION OF FIREBRAND TRAJECTORY MODEL

Given the core fluid mechanical properties, the next step is to determine the trajectory of a given firebrand that is lifted up into the core from a specified ground location within the core. The determination of this trajectory includes the firebrand motion in the core region, in the region just outside the core where the ambient swirl is dominant, and then the region beyond the swirl where the prevailing winds determine the firebrand motion. The in-flight burning characteristics of a firebrand are coupled to the firebrand trajectory and must be considered. Results from Section III of this report are used to model the size and density change of firebrands with cylindrical shapes (representing wood sticks or branches) and flat plates (representing bark platelets).

The flight of a firebrand is divided into three regions: Region I is the fire whirl or core region, Region II is the ambient swirl region where the driving force is the purely swirling ambient circulation, and Region III is beyond the swirl region where the firebrand driving force is the prevailing wind.

Looking down at the ground, the very narrow core region (Region I) appears as a relatively small circle surrounded by a larger circle which comprises the outer boundary of Region II. Everything outside this second circle is Region III. The Region II-III boundary is located at that radius where the azimuthal velocity of the ambient swirl ($W = \Gamma/r$) is equal in magnitude to the wind velocity at a height of $z_e/2$. [Actually, the computation has been set up so that the boundary occurs when the swirl velocity is any specified fraction of the wind velocity, but for simplicity all the calculations that have been carried out (and reported in Section IV-D-3) have located the boundary at a velocity ratio of unity.] Thus, the location of this boundary is a function of both the swirl intensity $\Gamma$ and the wind. The vertical extent of Regions I and II is from the ground to $z = z_e$, with the boundary between them specified by Eq. (20). Everything above $z = z_e$ or at a radius larger than the Region II outer boundary radius is Region III.

The general model developed here allows for subdivision of Region III into ten zones in the vertical direction and four in the horizontal, and allows for a horizontal and a vertical wind component in each zone. The wind is taken to have only one horizontal component, which is in the x-direction, with y being normal to the wind and z being positive upward. The x-values giving the location of the boundaries between the four zones in the horizontal direction are arbitrary and are specified as inputs; likewise, with the ten vertical zones the boundary values of z are inputs. Thus, Region III is divided into 40 separate subzones. The vertical and horizontal wind components within each subzone can be independently specified. Within each of the four horizontally separated zones, a mean ground slope can be specified. For the purpose of illustrating typical trajectory results, the calculations shown in Section IV-D-3 are for a constant wind which has only a horizontal component and for the case of level ground.

Firebrand burning is considered to be taking place in Region III only because, as is shown in Section IV-D-3, the total time a firebrand spends in Regions I and II is small compared to its total flight time. Therefore,

although ignition has taken place, the size and density of the firebrand are taken to be constant in Regions I and II, with burning continuing as the firebrand enters Region III.

The equations of motion for a firebrand in Region I are written in terms of the drag coefficient $C_D$ of the firebrand. The drag force appropriate to the firebrands and acting in a given direction is given by $(1/2)\rho C_D A \left| V_r \right| V_{rc}$, where $V_r$ is the relative velocity between the core flow (in Region I) and the firebrand, $V_{rc}$ is the component of the relative velocity in that direction, and A is the drag area. The wind tunnel and drop test experiments of Tarifa[5] demonstrate that the flight of a firebrand can be predicted by assuming that the firebrand flies in its maximum drag orientation with constant drag coefficient. Cylindrical and flat plate shaped firebrands are of interest here. The drag area A is then the maximum drag or broadside area, and the drag coefficient is based on that reference area.

In cylindrical coordinates the axial, radial, and azimuthal equations of motion for Region I are

$$m\ddot{z} = \left(\frac{1}{2}\right)\rho C_D A\left[(u-\dot{x})^2 + \dot{r}^2 + (W-r\dot{\theta})^2\right]^{1/2}(u-\dot{x}) - mg \tag{38}$$

$$m(\ddot{r}-r\dot{\theta}^2) = \left(\frac{1}{2}\right)\rho C_D A\left[(u-\dot{x})^2 + \dot{r}^2 + (W-r\dot{\theta})^2\right]^{1/2}(-\dot{r}) \tag{39}$$

$$m(r\ddot{\theta} + 2r\dot{\theta}) = \left(\frac{1}{2}\right)\rho C_D A\left[(u-\dot{x})^2 + \dot{r}^2 + (W-r\dot{\theta})^2\right]^{1/2}(W-r\dot{\theta}) \tag{40}$$

where r, θ, z are the coordinates of the firebrand and u and W are the axial and swirl velocities of the core gases as given in Section IV-B.

It is convenient to cast Eqs. (38) through (40) in nondimensional form. If one uses $u_o$ as the characteristic velocity, $z_e$ as a characteristic length, $z_e/u_o$ as a characteristic time, and $u_o^2/z_e$ as a characteristic acceleration, the equations become

$$\ddot{\tilde{z}} = \alpha\left[(\tilde{u}-\dot{\tilde{z}})^2 + \dot{\tilde{r}}^2 + (\tilde{W}-\tilde{r}\dot{\tilde{\theta}})^2\right]^{1/2}(\tilde{u}-\dot{\tilde{z}}) - \beta \tag{41}$$

$$\ddot{\tilde{r}} - \tilde{r}\dot{\tilde{\theta}}^2 = \alpha\left[(\tilde{u}-\dot{\tilde{z}})^2 + \dot{\tilde{r}}^2 + (\tilde{W}-\tilde{r}\dot{\tilde{\theta}})^2\right]^{1/2}(-\dot{\tilde{r}}) \tag{42}$$

$$\tilde{r}\ddot{\tilde{\theta}} + 2\dot{\tilde{r}}\dot{\tilde{\theta}} = \alpha\left[(\tilde{u}-\dot{\tilde{z}})^2 + \dot{\tilde{r}}^2 + (\tilde{W}-\tilde{r}\dot{\tilde{\theta}})^2\right]^{1/2}(\tilde{W}-\tilde{r}\dot{\tilde{\theta}}) \tag{43}$$

where

$$\alpha = \rho C_D A z_e / 2\rho_w V$$

$$\beta = g z_e / u_o^2$$

$$\tilde{u} = 1 - \tilde{z}$$

$$\tilde{W} = \Gamma z_e \tilde{r}(1-\tilde{z})/u_o a_o^2$$

and $\rho_w$ and V are the density and volume of the firebrand.

The initial conditions for these differential equations are $\tilde{t} = 0$, $\dot{\tilde{r}} = \dot{\tilde{\theta}} = \dot{\tilde{z}} = 0$, $\tilde{z} = \tilde{z}_o$, $\theta = \theta_o$, $\tilde{r} = \gamma a_o / z_e$. The firebrand is taken to be at rest (no velocity) when lifted up into the fire whirl. For the full-scale case, where $z_e$ can be thousands of feet, the firebrand is taken to be lifted up at $\tilde{z}_o = 0$. For the UCSB core firebrand experiments, they are introduced into the core at a given height $z_o$ ($z_o$ = 45 in.), so that $\tilde{z}_o = z_o / z_e$. The initial radial position is taken to be at a given fraction $\gamma$ of the initial radius $a_o$. As shown in Section IV-D-3, the range and time of flight of a firebrand are very strongly dependent on $\gamma$, the initial radial position. Firebrands lifted up away from the centerline of the whirl will be centrifuged out the side of the whirl very quickly and will not achieve as large a height as a firebrand which is initially closer to the center of the whirl. The greater the height at which a firebrand enters the prevailing wind pattern, the greater its range.

The initial azimuthal position $\theta_o$ is arbitrary as far as the Regions I and II results are concerned, since these regions are azimuthally symmetric. In Region III however, since the wind is in the x-direction, the firebrand's

range is a function of $\theta_o$. The increase in range between a firebrand entering Region III at a positive value of x and moving in the x-direction compared to that for a firebrand entering Region III at a negative value of x and initially moving against the wind can be several hundred feet. Note that rotating $\theta_o$ by a given angle will rotate the angular position at which the firebrand enters Region III by that same angle.

Equations (41) through (43) describe the motion of a firebrand in the core. If the firebrand leaves the side of the core, it will enter Region II. The motion in Region II is described by the same equations as in Region I, except that in Region II there is no gas vertical velocity, only a swirl velocity described by

$$\tilde{W} = \frac{\tilde{\Gamma}}{u_o z_e \tilde{r}}, \qquad \text{with } \tilde{u} = 0 \tag{45}$$

In addition, the gas density appearing in $\alpha$[Eq. (44)] is replaced by $\rho_\infty$.

Once in Region II the firebrand will generally begin to fall due to gravity. It will also be centrifuged outward by the swirl until it enters Region III. A firebrand may also enter Region III directly from Region I by passing through the top of the whirl ($z > z_e$). (Provisions are also made in the calculation for a firebrand to pass from Region I to Region III if it attains a sufficiently large radial position while in the very upper heights of the core.) In Region III, the firebrand burns and its density and size decrease. Tarifa[5] found that in a wind environment a firebrand (having typically a large drag to weight ratio) quickly attains a horizontal velocity equal to that of the wind and falls at its instantaneous fall velocity. Furthermore, the change in density and size of the burning firebrand is dependent on its relative velocity with respect to the wind, which, quickly after introduction into the wind, becomes the instantaneous fall velocity $W_f$.

In our case, the Region II equations are used upon first entering Region III. It was found that the velocity condition observed by Tarifa was quickly attained (within one or two sec after entering Region III). For cylinders

the change in density in flight is given by Eqs. (5a) and (10), with t being replaced by $t-t_3$ ($t_3$ is the time the firebrand enters Region III). The instantaneous fall velocity is given as a function of time (and of the initial density and diameter of the firebrand) as given by Muraszew[1], based on the Z-function of Tarifa[5]. From the fall velocity and the density, the instantaneous diameter is given by Eq. (2). [The $\rho$'s in Eqs. (2) and (5a) are wood densities.] These relationships for $\rho_w$ and D, as functions of time, are used in the equations of motion ($\alpha$ depends on $\rho_w$ and, through A/V, on D), with the velocity used in the density law being the relative velocity. For flat plates, Eqs. (5a) and (15) describe the density, Eq. (16) the fall velocity, and the ratio of A/V is unchanged. [Equations (10) and (15), as used here, are suitably modified so that the velocity used in them is input in units of ft/sec rather than mph.] Once the firebrand has reached Tarifa's velocity conditions, the relative velocity is $W_f$, and the full equations of motion are no longer necessary. Then the following equations are appropriate

$$\dot{z} = u_{z_{i,j}} - W_f \tag{46}$$

$$\dot{x} = u_{x_{i,j}} \tag{47}$$

where $u_z$ and $u_x$ are the vertical and horizontal wind components. The subscripts i,j identify the horizontal and vertical wind zones. In the computational results presented in Section IV-D-3, the wind is taken to be constant and in the horizontal x-direction only; Eqs. (46) and (47) are employed once the firebrand downward vertical velocity is within 10% of its instantaneous fall velocity and the horizontal velocity is within 10% of the wind velocity. The equations are integrated until the firebrand hits the ground or until its density or diameter becomes less than 5% of the original (at which point the firebrand is no longer assumed to be a threat). The firebrand density, size, and instantaneous fall velocity are determined as described above.

## D. ANALYTICAL RESULTS AND DISCUSSION

### 1. Correlation of Fire Whirl Analysis and Experimental Data

The fire whirl analytical model was presented in Section IV-B, with Eqs. (30) through (32), (34) and (36) determining the unknowns $\rho$, $T$, $u_o$, $a_o$, and $R/R_o$. The temperature dependence of the kinematic viscosity $\nu$ and the specific heat $C_p$ are incorporated into the equations. The Prandtl number factor appearing in Eq. (34), $P_r^{*-2/3}$, has a weak dependence on temperature. For simplicity, a value of unity is taken in the calculations; small departures from unity can be considered to be incorporated into the parameter a'.

Systematically eliminating the variables $\rho$, $T$, $u_o$, and $R/R_o$ from the equations results in the following equation for $a_o$

$$\frac{b' C_{p_\infty} T_\infty \rho_\infty \sqrt{\nu_\infty T_\infty}\left(\Lambda^{1.14} - 1\right)}{(\rho_b R_o) Q_c \left[1 - \left(C_{p_\infty} T_\infty / Q_c\right)\left(\Lambda^{1.14} - 1\right)\right] a_o} =$$

$$1 + \frac{a' C_{p_\infty} T_\infty \rho_\infty P_r^{*-2/3} \sqrt{\nu_\infty \Gamma}}{\left(\rho_b R_o\right) Q_i \sqrt{8 a_o d}} \left(\frac{R_{g,\infty}}{\Lambda R_{g,T}} + \frac{T_\infty R_{g\infty}}{T_s R_{g,s}}\right)\left[\Lambda^{1.14} - \left(\frac{T_s}{T_\infty}\right)^{1.14}\right] \cdot$$

$$\cdot \left[\frac{\Lambda^{1.6} R_{g,T}}{R_{g,\infty}} + \left(\frac{T_s}{T_\infty}\right)^{1.6} \frac{R_{g,s}}{R_{g,\infty}}\right]^{1/2} \tag{48}$$

where

$$\Lambda = \frac{(R_{g,\infty}/R_{g,T})}{[1 - (\Gamma^2/2 g z_e a_o^2)]} \tag{49}$$

As stated previously, the variation of the mixture gas constant from its ambient air value $R_{g,\infty}$ is insignificant. Thus, the mixture gas constant at the fuel surface $R_{g,s}$ and in the core $R_{g,T}$ are taken to be $R_{g,\infty}$ in Eqs. (48) and (49).

The primary input variables are $\Gamma$, $z_e$, $\rho_b R_o$, and d. Data from the UCSB subscale experiments are used to determine a' and b'. Once this is done and the input variables are specified, Eq. (48) can be solved for $a_o$. Once $a_o$ is obtained, the other variables can be easily obtained from the equations. For instance, $\rho$ can be obtained from Eq. (30), and T from Eq. (31), followed by $R/R_o$ from Eq. (34) and $u_o$ from Eq. (32).

Equation (48) is solved for $a_o$ using a Newton's divided difference iteration procedure. This procedure solves the equation f(x) = 0 for x, given the function f. Starting with an initial guess of the solution $x_o$, the slope $f'(x_o)$ is computed and its intercept with the x-axis found. This intercept value of x becomes the next guess for the solution. This process is repeated until the departure of f from zero is less than a specified value.

The experimental effort is described and presented in Section V. The data from various configurations were selected for the analytical-experimental correlation. Five configurations were selected as being most representative and having the most complete, consistent, and reliable data. These configurations consist of the set with a 9-in. crib diameter and $\beta = 0.5$ ($\beta$ = volume packing ratio), with stick lengths of 2.5, 5, and 7.5 in. The other configurations were a 6-in. crib diameter and a stick length of 5 in., with packing ratios of 0.25 and 0.5. The latter configuration was the primary one used in the experimental phase, and data averaged over two tests for that configuration were used in the correlation.

The principal correlation variables used in the determination of a' and b' are T and $u_o$. The bulk of the data was taken at z = 45 in., including axial velocity radial profiles. From these data, a radial mean velocity was obtained at z = 45 in. Using Eq. (28), $u_o$ is obtained. The mean temperature T is obtained from the temperature radial profile at z = 45 in. While Fig. 38, which is for one given test, shows that the core centerline temperature is less at z = 17 in. than at z = 45 in., the mean temperature at 17 in. is actually slightly higher than at 45 in., as shown by Fig. 39. Similarly, there is a

slight decrease in the mean temperature at z = 71 in. compared to z = 45 in., but this decrease is not as large as the centerline temperature decrease shown in Fig. 38. Since the measured radial mean temperature does not change much with height, it is reasonable to obtain the mean temperature from the abundant z = 45 in. data.

The circulation $\Gamma$ was measured, and varied from 3.9 to 6.5 $ft^2/sec$ for the five configurations used here. The values of $z_e$ and d are 18 ft and 1/4 in., respectively. The values of $\rho_b R_o$ are obtained by dividing the no-swirl burn rate data given in Table 10 by the crib area.

No burn rate data without swirl were available for the case with the 9-in. crib diameter and the 7.5-in. long sticks. In addition, the indicated no-swirl burn rate for the 2.5-in. long sticks was greater than that obtained with swirl. The no-swirl burn rate data for the 5-in. long sticks (with the same crib diameter and packing ratio as for the 2.5- and 7.5-in. long sticks) were used to infer the no-swirl burn rate for the 2.5- and the 7.5-in. sticks. The measurements reported by Harmathy[14] indicated that for large packing ratios (dense configuration, or fuel surface controlled regime), the mass burn rate is directly proportional to the exposed surface area of fuel. Thus, for the cases of 9-in. crib diameter, $\beta = 0.5$, and varying stick height, the mass burn rate should be directly proportional to the stick height. In this manner, the no-swirl burn rate (and hence $\rho_b R_o$) for the 2.5- and 7.5-in. sticks was obtained from that of the 5-in. long sticks. Also, for a constant value of the product of $\beta$ and stick length, the mass burn rate should vary with the crib area and $\rho_b R_o$ should be constant. For the two cases where only the crib diameter varied, this was found to hold to within a few percent, which is well within the experimental uncertainty for measuring the burn rate. Thus, for these two cases $\rho_b R_o$ was taken to be the same (equal to the value for the 6-in. crib).

Calculations were made for each of the five configurations for varying values of a' and b'. The values of a' and b' which were appropriate for each of the five cases were those which resulted in a calculated T and $u_o$ which

matched those obtained experimentally. The values of a' and b' determined for the five cases are given in Table 2, as are the experimentally obtained values of $\Gamma$, $\rho_b R_o$, T, and $u_o$ and the calculated values of $R/R_o$ and $a_o$. Also shown are the measured and estimated ratios of fuel mass loss with swirl to that without swirl. The estimated value was obtained as follows: The crib radius is larger than the core radius. The burn rate of the wood within the core is enhanced, relative to the no-swirl case, by the ratio $R/R_o$. Outside the core, it is assumed that the burn rate is the same as without swirl. Thus

$$\left(\frac{\dot{M}}{\dot{M}_o}\right)_{est.} = 1 + \left(\frac{a_o}{r_c}\right)^2 \left[\left(\frac{R}{R_o}\right) - 1\right]$$

where $r_c$ is the radius of the wood crib. Actually, outside the core there is still an ambient swirl environment which should increase the burn rate above the no-swirl quiescent value. Hence, the estimated value is expected to be on the low side. As seen in Table 2, the estimated ratio is below the measured ratio in four of the five cases. The average difference is 25%, which is reasonable given the uncertainty in the burn rate measurement and in the estimated value.

The following trends are evident from Table 2: Increasing $\Gamma$ increases T, $u_o$, $R/R_o$, and $a_o$. Increasing $\rho_b R_o$ (for near constant $\Gamma$) increases T and $u_o$ and decreases $R/R_o$. The greater the no-swirl quiescent burn rate, the greater the burn rate with swirl but the smaller the percentage of burn rate enhancement due to the swirl.

The core analysis involves various assumptions. The UCSB data can be used to check the appropriateness of some of them. As mentioned previously, the measured radial mean temperature changed little with height. (Also, as seen from Fig. 39, the temperature does not vary strongly with radius over the inner portion of the core.) The assumption of a constant mean temperature seems reasonable. The calculated core radius is slightly

Table 2. Fire Whirl Parameters for UCSB Experiments

| Configuration Parameters: | | | | | |
|---|---|---|---|---|---|
| Crib Diameter (in.) | 6 | 6 | 9 | 9 | 9 |
| Packing Ratio | 0.25 | 0.5 | 0.5 | 0.5 | 0.5 |
| Stick Length (in.) | 5 | 5 | 2.5 | 5 | 7.5 |
| $\Gamma$ ($ft^2$/sec) | 3.9 | 4.6 | 6.1 | 6.3 | 6.5 |
| $\rho_b R_o$ ($lb_m/ft^2$-sec) | 0.376 | 0.0194 | 0.0097 | 0.0194 | 0.0291 |
| T($^oR$) | 2050 | 2100 | 1500 | 2150 | 2250 |
| $u_o$ (ft/sec) | 35.2 | 32.8 | 29.6 | 35.9 | 36.8 |
| a' | 0.25 | 0.58 | 1.5 | 0.64 | 0.44 |
| b' | 45.15 | 44.35 | 71.35 | 54.6 | 54.1 |
| $R/R_o$ | 1.28 | 2.34 | 3.5 | 2.58 | 1.8 |
| $a_o$ (ft) | 0.133 | 0.156 | 0.223 | 0.213 | 0.218 |
| $(\dot{M}/\dot{M}_o)_{measured}$ | 1.10 | 1.88 | 1.33 | 2.53 | 1.68 |
| $(\dot{M}/\dot{M}_o)_{estimated}$ | 1.08 | 1.52 | 1.89 | 1.51 | 1.27 |

larger than the inferred measured radius. For the $\Gamma = 4.6$ ft$^2$/sec case, the optically inferred core radius is about 1.5 in., while the calculated (shown in Table 2) is 1.8 in. The effective core radius obtained from the core tangential velocity (Fig. 36) is larger than predicted, while the effective radii based on the vertical velocity and temperature radial profiles (see Figs. 35 and 39) are smaller. Considering all the data, the prediction of the core radius appears to be on the high side, but realistic.

The model predicts an azimuthal velocity in the core which varies radially from zero at the centerline to a maximum at the core-ambient air boundary. The wood data (Fig. 36) and the acetone data (Fig. B-7) bear this out. The mean vertical velocity is predicted to be a maximum at the core base and to decrease with height z according to Eq. (28). The data (Fig. 37) show that the maximum centerline velocity was at the 45-in. measurement station, rather than at the 17-in. station, but that the velocity then decreased beyond 45 in. The centerline velocity decrease from 45 to 71 in. shows quantitative as well as qualitative agreement between the model and the data. Figure 35 shows that the vertical velocity radial profiles in one given wood test were similar at 17 and 45 in. Radial profiles of the vertical velocity at all three heights were taken for the acetone tests and are shown in Fig. B-12. The mean vertical velocity for the acetone tests shows a monotonic decrease with height as expected, although quantitatively the comparison is better at the higher locations. While there is some discrepancy with the vertical velocity comparison, it does not appear to be serious and occurs only in the lower portion of the core. Thus, the azimuthal and vertical velocity behavior predicted by the model seems reasonable.

The boundary layer measurements of the radial velocity in the ground boundary layer, made with the boundary layer rakes described in Section V, provide for another check on the analysis. The purpose of the rakes is to measure the profile of the boundary layer radial inflow velocity. The analysis is not in terms of the radial inflow velocity, but rather in terms of the boundary layer mass inflow, which is proportional to the product of the mean radial

velocity and the boundary layer thickness. From Byram and Martin[6], an estimated boundary layer thickness of 0.1 ft in the vicinity of the core is used, which results in a radial boundary layer velocity of up to 8 ft/sec at entrance to the core. The boundary layer rake measurements were taken during the acetone tests described in Appendix B. The measurements were taken at a distance of 6 in. from the core centerline for values of $\Gamma$ of about 3-1/2 $ft^2$/sec and core radii of about 1.7 in. Since the boundary layer radial inflow velocity varies inversely with distance from the core centerline, the velocity at 6 in. is less than the velocity at the core entrance by more than a factor of three. In addition, the velocity is directly proportional to the circulation raised to a power slightly greater than one. Thus, the expected radial inflow velocity for the acetone tests at the measurement location is approximately 1 ft/sec. No measurable velocity was picked up by the rakes. Since the velocity sensitivity of the rakes is 2 to 3 ft/sec, the rake data are consistent with the results indicated by the analysis.

The fire whirl results show reasonable trends. For instance, it is to be expected that as the strength of the ambient circulation increases, the core temperature and velocity will also increase. Likewise, as the energy that would be released by the burning fuel in a quiescent environment increases (as $\rho_b R_o$ increases), it is reasonable that the core temperature and velocity will increase. On the basis of the reasonableness of the results, it is anticipated that the analysis can be used as a predictive tool. Toward this end, it is necessary to express a' and b' as a function of $\Gamma$ and $\rho_b R_o$. Figure 14 is a log-log plot of a' and b' versus $\rho_b R_o$, with the values of $\Gamma$ also indicated. Table 2 and Fig. 14 show that a' increases with $\Gamma$ and decreases with $\rho_b R_o$. The trends for b', while not as easily discernible, seem to be similar to those for a'. From Fig. 14, the variation of a' and b' with $\Gamma$ and $\rho_b R_o$ is taken as a', b' = $c\Gamma^{\ell}(\rho_b R_o)^n$. Fitting this form to the results

$$a' = 0.00513\Gamma^{0.313}(\rho_b R_o)^{-1.085} \tag{50}$$

$$b' = 10.97\Gamma^{0.661}(\rho_b R_o)^{-0.097} \tag{51}$$

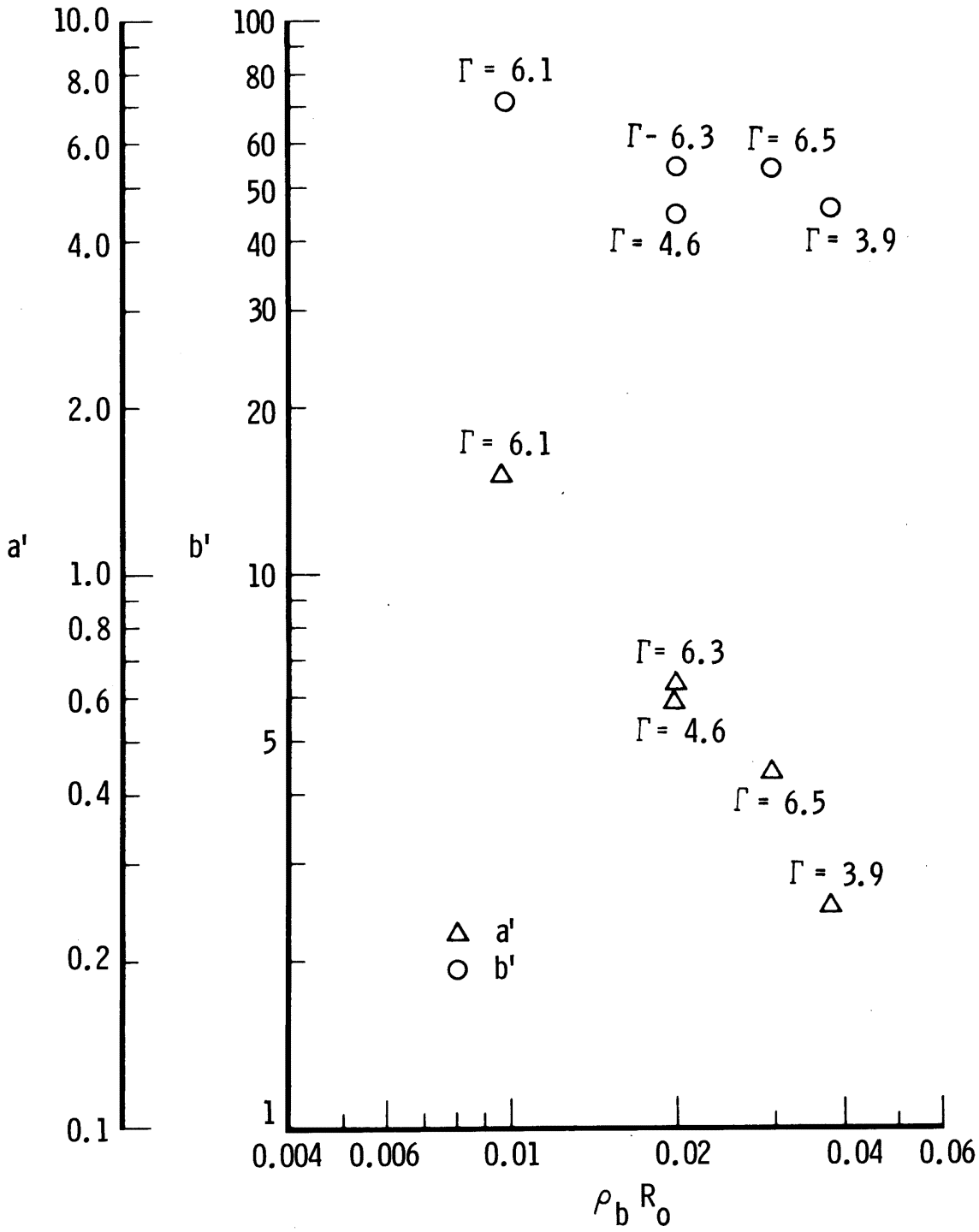


Fig. 14. Variation of Experimental Constants (a',b') with Burn Rate and Circulation Intensity

The variance of a' as determined from Eq. (50) from the actual value of a' is about 5%, with a maximum difference for any one case of about 9%. The variance and maximum difference for b' are about 10 and 23%, respectively, indicating that the a' fit has less scatter than the b'.

The incorporation of Eqs. (50) and (51) into Eqs. (34) and (36), in conjunction with Eqs. (30) through (32), provides for a self-contained set of equations pertinent to the subscale tests.

## 2. Extrapolation of the Model to Full-Size Fire Whirl

The preceding section described the correlation of the fire whirl analysis with the subscale experiments. The subscale whirl was created by the interaction of ambient vorticity with a hot buoyant column produced by an energy source comprised of burning wood, with the resulting core being fed, or supplied, by a radial inflow of air from a ground boundary layer. These same physical processes drive a full-scale fire whirl. If the physical mechanisms which determine the properties of a full-scale and a subscale whirl are the same, then it is expected that the same theory will apply to both. Thus, the analysis of the preceding section was applied to full-scale whirls.

Calculations were made for full-scale fire whirls for various values of $\Gamma$ and $\rho_b R_o$ at a given value of d and $z_e$. It was found that much lower values of b' than those indicated by Eq. (51) were needed in order to obtain reasonable results for T and $u_o$. On the other hand, the sensitivity of the results to a' was not as large. It was noted in the preceding section that the scatter in b' was larger than for a'. Therefore, it was decided to retain Eq. (50) for a' but to discard Eq. (51). The temperature measurements are considered to be among the most reliable data obtained in the subscale experiments, so the temperature T was used as the experimentally derived input parameter rather than b'. Fitting a function of the form $T = c\Gamma^a(\rho_b R_o)^b$ to the UCSB data in Table 2 results in

$$T = 7883\Gamma^{0.07475}(\rho_b R_o)^{0.378} \tag{52}$$

with a mean variance from the data of about 7%, with four of the five cases differing by 5.5% or less.

Now, the mean core temperature is expected to decrease with increasing total core height $z_e$ for constant $\Gamma$ and $\rho_b R_o$. As $z_e$ increases, the core base area decreases as $1/z_e$, keeping the core volume constant. As the core base area decreases, the amount of fuel burning within the core decreases, as does the heat input into the core. (It will be seen later that the burn rate enhancement due to swirl decreases with increasing $z_e$, so the heat input decreases because both the amount of fuel burning and its rate of burning decrease.) Since a smaller amount of heat is input into the same volume, the mean core temperature is expected to decrease.

The UCSB experiments, performed with the one experiment rig, had a fixed $z_e$ of 18 ft. When Eq. (52) is rewritten to include the dependence of T on $z_e$, $T = c z_e^n \Gamma^{0.07475} (\rho_b R_o)^{0.378}$, where $c(18)^n = 7883$. To determine c and n, the temperature at another value of $z_e$ must be known or assumed, preferably for a full-scale case. The combustion temperature of wood containing 2% moisture in a mixture having 50% and 100% excess air (above that needed for a stoichiometric mixture) is approximately 3300 and 2800°R, respectively. Radiation losses from the core would lower the temperature. Remembering that T is a mean core temperature, a value of T of 2000-2500°R for a moderate whirl is not unreasonable. (For instance, the UCSB subscale tests had calculated mean core air to fuel mixtures which contained approximately 100% excess air, and their mean core temperatures were generally around 2000°R or slightly higher.)

Most of the preliminary full-scale calculations were made for a whirl with $\Gamma = 3000$ ft$^2$/sec, $z_e = 2000$ ft, $\rho_b R_o = 0.1165$ lb$_m$/ft$^2$-sec and d = 0.00444 f
(These are reasonable values for forest slash areas.) The calculations indicated that the mean fuel-air mixture contained approximately 100% excess air. Various temperatures in the 2000-2500°R range were taken for the mean core temperature for this case, and the corresponding c's and n's obtained. Calculations were then made for several values of the input parameters. The

most reasonable set of calculations occurred when the temperature for the above $\Gamma = 3000\ ft^2/sec$ reference case was taken to be $2200^oR$. The sensitivity of the results to changes in this reference temperature and further discussion of why this value was selected will be presented after the results of the full-scale calculations are given. This produces the following equation for T ($^oR$)

$$T = 15{,}130\, z_e^{-0.2255} \Gamma^{0.07475} (\rho_b R_o)^{0.378} \tag{53}$$

With Eq. (53), b' is no longer required, and the determination of the unknown parameters is simplified. Equations (53), (30) through (32), (34), and (50) are now self-contained. The primary input quantities are $\Gamma$, $z_e$, $\rho_b R_o$, and d. These quantities are not completely independent. For instance, the value of $\rho_b R_o$ as calculated by Rothermel[3] depends on $\sigma$, the fuel particle surface area-to-volume ratio. For cylindrically shaped fuel materials, $\sigma = 4/d$, where d is the characteristic fuel cross-sectional dimension (d = diameter or width for circular or square cross section cylinders). Hence, $\rho_b R_o$ depends on d, as well as on other fuel characteristics. (The ratio $R/R_o$ is the burn rate enhancement due to swirl relative to the burn rate in a quiescent environment, so that $R_o$, or $\rho_b R_o$, is a property solely of the fuel and of its loading and spacing.)

The swirl equations have a direct dependence on d, apart from its effect on $\rho_b R_o$. Also, the characteristics of the ambient circulation may be a function of the fuel as well as of the local wind and terrain. For instance, a more intense burning may increase $\Gamma$ and $z_e$ beyond that which would be solely determined by the wind and terrain conditions. Thus, $\Gamma$, $z_e$, d, and $\rho_b R_o$ are linked together. It is anticipated that future effort will provide further information on the dependence of the swirl characteristics $\Gamma$ and $z_e$ on the fuel, the wind, and the terrain features.

The determining equations are rewritten here for convenience and completeness. The a' and T are given by

$$a' = 0.00513\Gamma^{0.313}(\rho_b R_o)^{-1.085} \tag{50}$$

$$T = 15{,}130\, z_e^{-0.2255}\Gamma^{0.07475}(\rho_b R_o)^{0.378} \tag{53}$$

With $\rho$ then determined by Eq. (31), $a_o$ is given by

$$(\rho_\infty - \rho)g a_o^2 = \rho_\infty \frac{\Gamma^2}{2z_e} \tag{30}$$

$R/R_o$ is then determined from

$$\frac{R}{R_o} = 1 + \frac{a' C_{p_\infty} T_\infty \rho_\infty P_r^{*-2/3} \sqrt{\frac{\nu_\infty \Gamma}{8a_o d}}}{\rho_b R_o Q_i} \left[\left(\frac{T}{T_\infty}\right)^{1.14} - \left(\frac{T_s}{T_\infty}\right)^{1.14}\right] \cdot$$

$$\left(\frac{T_\infty}{T} + \frac{T_s}{T}\right)\left[\left(\frac{T}{T_\infty}\right)^{1.6} + \left(\frac{T_s}{T_\infty}\right)^{1.6}\right]^{1/2} \tag{34}$$

Equation (32) becomes, with $\dot{M}_f$ written in terms of R by Eq. (37)

$$u_o = \frac{\rho_b R_o Q_c \frac{T}{T_\infty} \frac{R}{R_o}}{C_{p_\infty} T_\infty \rho_\infty \left[\left(\frac{T}{T_\infty}\right)^{1.14} - 1\right]} \tag{54}$$

The change in core size and mean upward velocity with z are given in terms of $a_o$ and $u_o$ by Eqs. (20) and (28).

The above equations were utilized to make calculations for full scale fire whirls, which are given in Tables 3 through 7. The tabulated values for core properties--i.e., core base radius $a_o$, mean core temperature T, core base mean velocity $u_o$, ratio of fuel to total mass flow rate $\dot{M}_f/\dot{M}_T$ and burn rate enhancement ratio $R/R_o$--were obtained for various values of ambient circulation $\Gamma$, vertical extent $z_e$ of the circulation, characteristic fuel diameter d, and fuel burn rate per unit area $\rho_b R_o$.

Table 3 gives results for varying $\Gamma$ and $z_e$ for $\rho_b R_o = 0.1165$ $lb_m/ft^2$-sec and d = (4/900) ft. This value of d is for $\sigma = 900$ $ft^{-1}$ ($\sigma$ = fuel particle surface area/particle volume). These values of d and $\rho_b R_o$ are typical of forest slash areas. This table shows that the effect of increasing $\Gamma$, besides increasing T, is to increase $a_o$, $u_o$, $R/R_o$, and $\dot{M}_f/\dot{M}_T$. As expected, the fuel burn rate and the core thermal and kinetic energy increase as the swirl intensity increases. The increase in $\dot{M}_f/\dot{M}_T$ and T with increasing $\Gamma$ are consistent. The mixture is, on the mean, air-rich, but as the fuel-to-air ratio $(\dot{M}_f/\dot{M}_T)/[1 - (\dot{M}_f/\dot{M}_T)]$ increases, the temperature increases as expected. As discussed previously, when $z_e$ increases, the temperature decreases, as does $\dot{M}_f/\dot{M}_T$ and $R/R_o$. For low or moderate values of $\rho_b R_o$, $u_o$ also decreases with increasing $z_e$, as it is dominated by the decrease in burn rate enhancement [see Eq. (54)]. Results for high values of $\rho_b R_o$ will be given later. Some of the Table 3 results are shown in Fig. 15.

The results of Table 3 are representative of what may be expected in an actual full-scale whirl. King[15] has presented cinematographic film data of a fire whirl which occurred during a severe brush fire in 1962 in Australia. The film indicated that the circulation strength $\Gamma = Wr$ was about 10,000 $ft^2/sec$ and that the upward core velocity was about 300 ft/sec. King did not ascertain the height of the fire whirl, except that it was greater than 1000 ft.

Table 4 shows the effect of varying d for given values of $\Gamma$, $z_e$, and $\rho_b R_o$. As d decreases ($\sigma$ increases), both $u_o$ and $R/R_o$ increase. Decreasing d increases the fuel surface area to weight ratio, thereby making the heat transfer to the wood more efficient in producing ignition and burning.

Table 3. Core Properties versus $\Gamma$, $z_e$ for $\rho_b R_o = 0.1165$ $lb_m/ft^2$-sec, d = 4/900 ft

| $z_e$ = / $\Gamma$ = | | 3000 $ft^2$/sec | 5000 | 6000 | 8000 | 10,000 | 12,000 | 15,000 |
|---|---|---|---|---|---|---|---|---|
| 2000 ft | $a_o$ | 9.60 ft | 15.9 | 19.0 | 25.3 | 31.6 | 37.8 | 47.2 |
| | T | 2200°R | 2286 | 2317 | 2367 | 2407 | 2440 | 2481 |
| | $u_o$ | 245 ft/sec | 287 | 304 | 335 | 362 | 385 | 418 |
| | $R/R_o$ | 2.96 | 3.52 | 3.76 | 4.17 | 4.53 | 4.86 | 5.3 |
| | $\dot{M}_f/\dot{M}_T$ | 0.077 | 0.081 | 0.083 | 0.085 | 0.087 | 0.089 | 0.091 |
| 4000 ft | $a_o$ | 6.98 | 11.5 | 13.8 | 18.4 | 22.9 | 27.4 | 34.1 |
| | T | 1882 | 1955 | 1982 | 2025 | 2059 | 2087 | 2122 |
| | $u_o$ | 228 | 265 | 280 | 307 | 331 | 352 | 381 |
| | $R/R_o$ | 2.57 | 3.04 | 3.23 | 3.58 | 3.89 | 4.17 | 4.54 |
| | $\dot{M}_f/\dot{M}_T$ | 0.061 | 0.065 | 0.066 | 0.068 | 0.070 | 0.071 | 0.073 |
| 8000 ft | $a_o$ | 5.11 | 8.43 | 10.1 | 13.4 | 16.7 | 19.4 | 24.8 |
| | T | 1609 | 1672 | 1695 | 1732 | 1761 | 1785 | 1815 |
| | $u_o$ | 209 | 241 | 254 | 278 | 298 | 317 | 342 |
| | $R/R_o$ | 2.16 | 2.55 | 2.71 | 3.0 | 3.25 | 3.48 | 3.79 |
| | $\dot{M}_f/\dot{M}_T$ | 0.048 | 0.051 | 0.052 | 0.054 | 0.055 | 0.057 | 0.058 |
| 10,000 ft | $a_o$ | 4.63 | 7.63 | 9.13 | 12.1 | 15.1 | 18.0 | 22.5 |
| | T | 1530 | 1590 | 1611 | 1647 | 1675 | 1698 | 1726 |
| | $u_o$ | 202 | 232 | 245 | 267 | 287 | 305 | 329 |
| | $R/R_o$ | 2.03 | 2.39 | 2.54 | 2.80 | 3.04 | 3.25 | 3.55 |
| | $\dot{M}_f/\dot{M}_T$ | 0.044 | 0.047 | 0.048 | 0.050 | 0.051 | 0.052 | 0.054 |

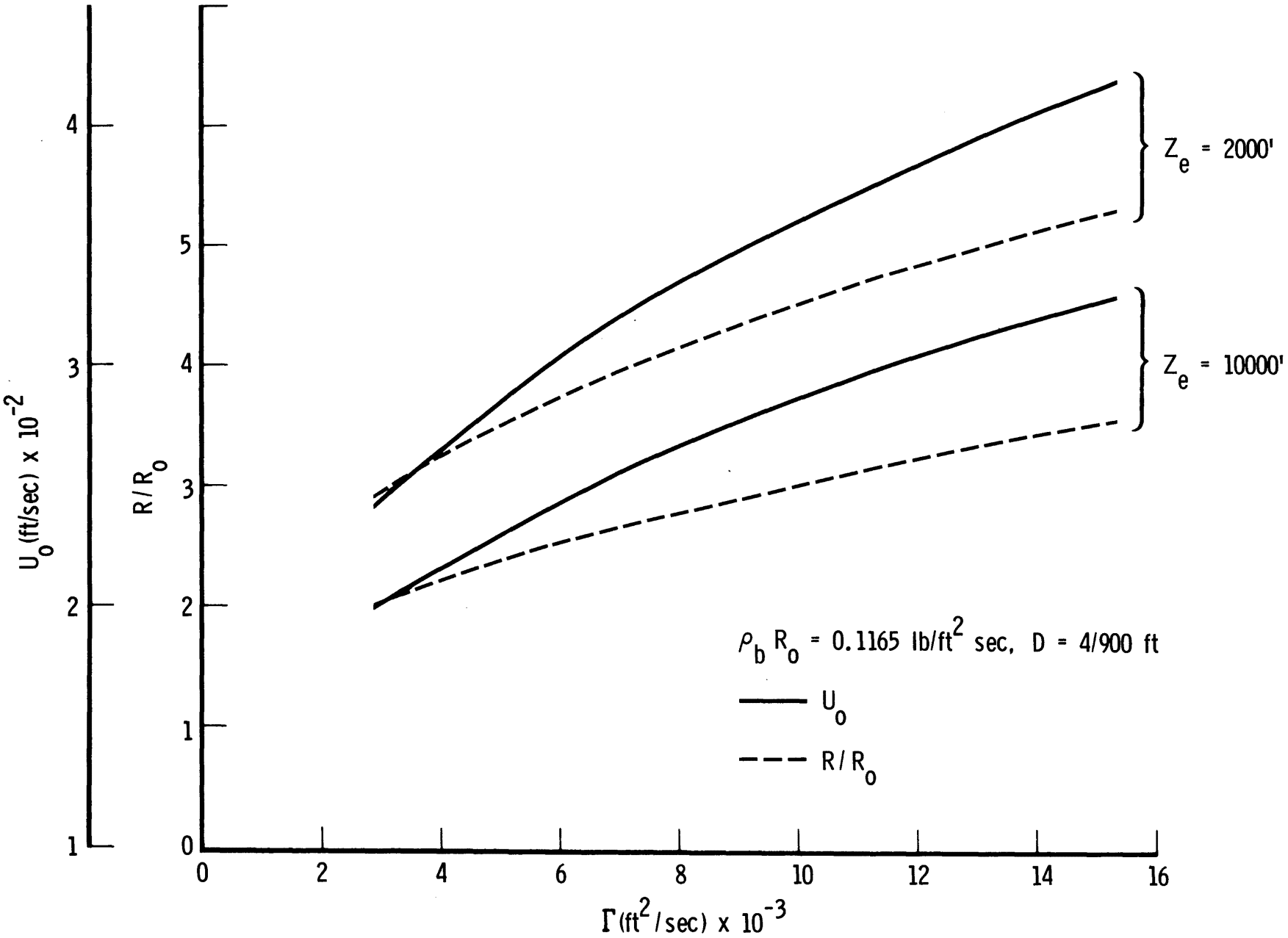


Fig. 15. Variation of Mean Vertical Velocity (at ground zero) and Burn Rate Amplification Factor with Circulation Strength and Height

Equation (34) directly indicates the increase in $R/R_o$ as d decreases, following which Eq. (54) gives the increase in $u_o$.

Table 4. Effect of d (Effective Stick Diameter) on Core Properties for $\Gamma = 3000$ ft$^2$/sec, $z_e = 3000$ ft, and Constant $\rho_b R_o = 0.1165$ lb$_m$/ft$^2$-sec

| d (ft) | $u_o$ (ft/sec) | $R/R_o$ |
|---|---|---|
| 4/300 | 176 | 2.13 |
| 4/900 | 245 | 2.96 |
| 4/1000 | 254 | 3.07 |
| 4/1200 | 270 | 3.27 |
| 4/1500 | 292 | 3.54 |

Tables 5 through 7 show the variation of the core properties with $\Gamma$ and $z_e$ for values of $\rho_b R_o$ of 0.03, 0.3, and 0.7 lb$_m$/ft$^2$-sec, respectively. Averaged over a large area (e.g., one acre), the value of the quiescent air burn rate $\rho_b R_o$ is not expected to be more than approximately 0.15 lb$_m$/ft$^2$-sec. For instance, data provided by Rothermel for a heavily loaded logging slash area (43 tons of fuel per acre) indicated a value of $\rho_b R_o$ of 0.14 lb$_m$/ft$^2$-sec. However, the local value of $\rho_b R_o$ over smaller areas could very well be significantly larger. The values of $\rho_b R_o$ given in Tables 5 through 7 cover a realistic range of low to high $\rho_b R_o$.

Table 5 is for a relatively low value of $\rho_b R_o$ of 0.03 lb$_m$/ft$^2$-sec. For low values of $\rho_b R_o$, the contribution of the fuel in generating large circulation intensities and sizes is small, and the wind and terrain conditions are expected to be dominant in determining the circulation characteristics. A smaller $\rho_b R_o$ indicates that a smaller $\Gamma$ and $z_e$ are more likely. Table 5 bears this out.

Table 5. Core Properties versus $\Gamma$, $z_e$ for $\rho_b R_o = 0.03$ $lb_m/ft^2$-sec, d = 4/900 ft

| $z_e$ = / $\Gamma$ = | | 2000 $ft^2$/sec | 3000 | 5000 | 6000 | 8000 | 10,000 | 12,000 |
|---|---|---|---|---|---|---|---|---|
| 2000 ft | $a_o$<br>T<br>$u_o$<br>$R/R_o$ | 7.29 ft<br>1278°R<br>154 ft/sec<br>5.30 | 10.8<br>1317<br>196<br>6.90 | Burn rate enhancement ratio ($R/R_o$) too high (nonphysical) → | | | | |
| 4000 ft | $a_o$<br>T<br>$u_o$<br>$R/R_o$ | No whirl obtained (velocities too low) | 8.13<br>1127<br>76<br>2.33 | 13.3<br>1170<br>127<br>4.1 | 15.9<br>1187<br>149<br>4.8 | 21.0<br>1213<br>189<br>6.2 | 26.1<br>1233<br>224<br>7.5 | 31.2<br>1250<br>256<br>8.64 |
| 6000 ft | $a_o$<br>T<br>$u_o$<br>$R/R_o$ | | | ← | No whirl obtained | 17.8<br>1107<br>71<br>2.1 | 22.1<br>1125<br>100<br>3.1 | 26.4<br>1141<br>127<br>4.0 |
| 8000 ft | | | | | | | ← | No whirl obtained (need $\Gamma \sim 18{,}000$ to get $u_o \sim 75$) |

For small $z_e$, reasonable values are obtained for low $\Gamma$, while unrealistically high burn rate enhancement ratios are obtained for high $\Gamma$. For subscale whirls, enhancement ratios of 1.5 to 5 have been measured by Martin, Pendleton, and Burgess[16]. While this range could be larger for full-scale whirls, a ratio of 9 or 10 was considered excessive and, therefore, nonphysical. For large $z_e$, Table 5 shows that large $\Gamma$ are needed in order to generate a fire whirl (i.e., in order to have high uplift velocities). A velocity of 70 ft/sec was used as a cutoff in the table. Thus, it appears that a large $\Gamma$ or $z_e$ is not generally associated with a low $\rho_b R_o$. The smaller the value of $\rho_b R_o$, the smaller and less intense the fire whirl, if one does occur.

Comparing the results of Tables 3 and 5, it is seen that the velocity and temperature decrease as $\rho_b R_o$ decreases, as expected. While the enhancement ratio $R/R_o$ increases as $\rho_b R_o$ decreases, the actual burn rate with swirl, $\rho_b R$, decreases.

Calculations were also made for $\rho_b R_o = 0.02$ $lb_m/ft^2$-sec, which showed that the applicable range of $z_e$ and $\Gamma$ for realistic fire whirls was further reduced from the $\rho_b R_o = 0.03$ $lb_m/ft^2$-sec case. For instance, uncommonly large $\Gamma$ (a value of $\Gamma$ = 15,000-20,000 $ft^2$/sec may be near a practical upper limit that one can expect in a fire whirl) are needed for $z_e$ above 3000 to 4000 ft. From these results, it appears that a $\rho_b R_o$ of about 0.01-0.02 $lb_m/ft^2$-sec would be a practical lower limit for producing a viable fire whirl. It is to be expected then that the smaller the value of $\rho_b R_o$, the smaller the core velocity and core height, and the smaller the probability of initiating a spot fire a large distance away.

It is not surprising that intense fire whirls are associated with conditions of intense burning. Full-scale fire whirls seem to occur where the burning is most intense, for favorable wind and terrain conditions. In the UCSB experiments, strong fire whirls could not be obtained with low packing ratios and low values of $\rho_b R_o$. Initially, wood tripods were used as the fuel bed, with maximum packing ratios in the 0.1 to 0.2 range. These did not

produce strong whirls. For this reason the wood configurations shown in Fig. 26, with packing ratios of 0.25 and 0.5, were used for the experiments to obtain $\rho_b R_o$ values up to 0.04 $lb_m/ft^2$-sec.

Tables 6 and 7 present calculations for $\rho_b R_o$ = 0.3 and 0.7 $lb_m/ft^2$-sec, respectively. Again the trend of increasing T, $u_o$, and $\rho_b R$ with increasing and $\rho_b R_o$ is seen. The change in $u_o$ and $R/R_o$ with changing $\Gamma$, or $z_e$, is not as pronounced for the higher $\rho_b R_o$ as it was with the smaller. Tables 6 and 7 show that a very large circulation intensity $\Gamma$ but a small circulation height z is not realistic, since unreasonably high mean core temperatures occur. For large $\rho_b R_o$, temperatures up to and exceeding 3000°R are predicted. The high temperatures are consistent with the high fuel to total mass flow (air plus fuel) ratios ($\dot{M}_f/\dot{M}_T$) shown in Table 7. The stoichiometric value of $\dot{M}_f/\dot{M}_T$ is about 0.15 to 0.16, which is close to the results predicted in Table 7. For $\dot{M}_f/\dot{M}_T$ = 0.14, which is about a 10% excess air mixture, the combustion temperature for average wood with 2% moisture is about 4000°R. With radiation and thermal diffusion losses, an upper limit on T of 3500°R or less is not unreasonable. Thus, the results in Tables 6 and 7 have been cut off where T exceeded 3500°R.

Tables 3 through 7 illustrate that larger values of $\Gamma$ and $z_e$ can be expected to be associated with larger $\rho_b R_o$. For $\rho_b R_o$ = 0.7 $lb_m/ft^2$-sec (Table 7), a $z_e$ of 4000 ft or less is not realistic, while a $z_e$ of more than 2 mi can occur. For a given $z_e$ there is a $\Gamma$ above which the temperature is too high, indicating that if the $\Gamma$ were actually that high, the fuel would be burning with enough intensity to promote a larger $z_e$. With the high temperatures indicated in Table 7, it appears that 0.7-1.0 $lb_m/ft^2$-sec is a practical upper limit for $\rho_b R_o$. While fuel loadings in the forest are not expected to produce this high an average value of $\rho_b R_o$, it is conceivable that there may be such values occurring locally over small areas, but areas which are nevertheless large enough to maintain a fire whirl. With the large temperatures there is a slight increase in $u_o$ with increasing $z_e$, while for the smaller temperatures associated with Table 3, for instance, $u_o$ decreases with increasing $z_e$.

Table 6. Core Properties versus $\Gamma$, $z_e$ for $\rho_b R_o$ = 0.3 $lb_m/ft^2$-sec, d = 4/900 ft

| $z_e$ \ $\Gamma$ = | | 3000 $ft^2$/sec | 5000 | 6000 | 8000 | 10,000 | 12,000 | 15,000 |
|---|---|---|---|---|---|---|---|---|
| 2000 ft | $a_o$ | 9.17 ft | 15.2 | 18.2 | 24.3 | 30.3 | 36.3 | T too high ($t > 3500^oR$, non-physical) |
| | T | $3146^oR$ | 3268 | 3313 | 3385 | 3442 | 3489 | |
| | $u_o$ | 300 ft/sec | 327 | 338 | 359 | 375 | 391 | |
| | $R/R_o$ | 1.6 | 1.77 | 1.84 | 1.96 | 2.06 | 2.16 | |
| 4000 ft | $a_o$ | 6.6 ft | 10.9 | 13.1 | 17.4 | 21.8 | 26.1 | 32.5 |
| | T | $2691^oR$ | 2795 | 2834 | 2895 | 2944 | 2984 | 3035 |
| | $u_o$ | 298 ft/sec | 322 | 332 | 350 | 365 | 379 | 398 |
| | $R/R_o$ | 1.51 | 1.66 | 1.72 | 1.82 | 1.91 | 1.99 | 2.10 |
| 8000 ft | $a_o$ | 4.77 ft | 7.90 | 9.46 | 12.6 | 15.7 | 18.8 | 23.4 |
| | T | $2301^oR$ | 2391 | 2424 | 2476 | 2518 | 2552 | 2595 |
| | $u_o$ | 299 ft/sec | 319 | 328 | 344 | 357 | 370 | 386 |
| | $R/R_o$ | 1.43 | 1.55 | 1.60 | 1.69 | 1.77 | 1.84 | 1.94 |
| 10,000 ft | $a_o$ | 4.30 ft | 7.11 | 8.52 | 11.3 | 14.1 | 16.9 | 21.1 |
| | T | $2188^oR$ | 2273 | 2305 | 2355 | 2394 | 2427 | 2468 |
| | $u_o$ | 299 ft/sec | 319 | 327 | 342 | 355 | 367 | 383 |
| | $R/R_o$ | 1.40 | 1.52 | 1.57 | 1.65 | 1.73 | 1.79 | 1.88 |

Table 7. Core Properties versus $\Gamma$, $z_e$ for $\rho_b R_o = 0.7$ $lb_m/ft^2$-sec, d = 4/900 ft

| $z_e$ = \ $\Gamma$ = | | 3000 $ft^2$/sec | 5000 | 6000 | 8000 | 10,000 | 12,000 | 15,000 |
|---|---|---|---|---|---|---|---|---|
| 4000 ft | | T too high ($T > 3500^oR$, non-physical) → | | | | | | |
| 8000 ft | $a_o$ | 4.58 ft | 7.61 | 9.12 | 12.1 | 15.1 | | |
| | T | $3170^oR$ | 3293 | 3339 | 3411 | 3468 | | |
| | $u_o$ | 500 ft/sec | 512 | 517 | 526 | 534 | T too high → | |
| | $R/R_o$ | 1.15 | 1.19 | 1.21 | 1.23 | 1.26 | | |
| | $\dot{M}_f/\dot{M}_T$ | 0.13 | 0.13 | 0.14 | 0.14 | 0.14 | | |
| 10,000 ft | $a_o$ | 4.12 ft | 6.84 | 8.20 | 10.9 | 13.6 | 16.3 | 20.4 |
| | T | $3014^oR$ | 3133 | 3175 | 3244 | 3298 | 3344 | 3400 |
| | $u_o$ | 505 ft/sec | 515 | 520 | 529 | 537 | 544 | 554 |
| | $R/R_o$ | 1.14 | 1.18 | 1.20 | 1.22 | 1.25 | 1.27 | 1.30 |
| | $\dot{M}_f/\dot{M}_T$ | 0.12 | 0.12 | 0.13 | 0.13 | 0.13 | 0.14 | 0.14 |
| 13,000 ft | $a_o$ | 3.64 ft | 6.04 | 7.23 | 9.62 | 12.0 | 14.4 | 18.0 |
| | T | $2841^oR$ | 2952 | 2992 | 3057 | 3109 | 3151 | 3204 |
| | $u_o$ | 511 ft/sec | 521 | 525 | 533 | 541 | 548 | 557 |
| | $R/R_o$ | 1.13 | 1.17 | 1.18 | 1.21 | 1.23 | 1.26 | 1.28 |
| | $\dot{M}_f/\dot{M}_T$ | 0.11 | 0.12 | 0.12 | 0.12 | 0.12 | 0.13 | 0.13 |

From Eq. (54), $u_o \propto (T/T_\infty)^{-0.14} R/R_o$ for large T. For small $\rho_b R_o$, the decrease in $R/R_o$ with increasing $z_e$ is dominant. For large $\rho_b R_o$, $R/R_o$ changes very little with $z_e$, and the effect of decreasing temperature with increasing $z_e$ is the dominant effect on $u_o$.

The trends displayed in Tables 3 through 7 are consistent with the physics of the problem; namely, a temperature increase with increasing $\rho_b R_o$, increasing $\Gamma$, and decreasing $z_e$, and an increase in $u_o$ with increasing $\rho_b R_o$ and $\Gamma$. The applicability limits of the input variables are also seen to be physically plausible.

The sensitivity of the results to errors or uncertainties in the inputs can also be ascertained from Tables 3 through 7. The effect of an uncertainty in $\Gamma$ or $z_e$ is more pronounced for smaller values of $\rho_b R_o$. For a moderate value of $\rho_b R_o$, such as 0.1165 $lb_m/ft^2$-sec, the uncertainty in $u_o$ is about one-fourth the uncertainty in $\Gamma$. The uncertainty in $u_o$, on the average, is about one-tenth the uncertainty in $z_e$ and of opposite sign. For large values of $\rho_b R_o$, the uncertainty in $u_o$ decreases. For $\rho_b R_o = 0.7$ $lb_m/ft^2$-sec, the entire range of $u_o$ given in Table 7 varies by only 11%. For $\rho_b R_o$ near the lower limit for whirls, the change in $u_o$ with $\Gamma$ or $z_e$ can be very pronounced, as can be seen from Table 5 which shows a near-linear variation of $u_o$ with $\Gamma$. However, it is more likely that fire whirls will be associated with moderate to large $\rho_b R_o$, so that the results of Tables 3 and 6 are more indicative. They show that the uncertainty in $u_o$ is about one-tenth the uncertainty in $\rho_b R_o$. From Table 4, the uncertainty in $u_o$ due to an uncertainty in d is seen to increase as d decreases. On the average, the percentage uncertainty in $u_o$ is about 0.3 that of d.

In summary, the average uncertainty in $u_o$ is one-fourth the uncertainty of $\Gamma$, one-tenth that of $z_e$ and $\rho_b R_o$, and 0.3 that of d. These are rough guidelines. For a specific case, the equations are easy enough to apply to obtain the change in $u_o$ with a change in one of the inputs.

Besides $u_o$, the core density is also important in determining firebrand trajectories. From Eq. (31), the uncertainty in core density is equal in magnitude to the uncertainty in the core temperature, but of opposite sign. The uncertainty in temperature can be easily obtained from Eq. (53). From Eq. (53), $\Delta T/T = 0.07475\ \Delta\Gamma/\Gamma - 0.2255\Delta z_e/z_e + 0.378\Delta\rho_b R_o/\rho_b R_o$. Hence, for instance, the temperature is about five times more sensitive to uncertainties in $\rho_b R_o$ than in $\Gamma$. Similarly, the uncertainty in $a_o$ can be readily obtained from Eq. (30). It will be seen in Section IV-D-3 that the maximum range of a firebrand is largely unaffected by $a_o$.

The results presented in the tables and discussed above arose from using a reference temperature of 2200°R for the reference case where $\Gamma = 3000\ ft^2/sec$, $z_e = 2000$ ft, $\rho_b R_o = 0.1165\ lb_m/ft^2\text{-sec}$ in order to obtain Eq. (53). As stated earlier, this case has a mean fuel-air mixture containing approximately 100% excess air. A mean core temperature near 2000°R or slightly above is expected. Calculations using 2100°R and 2300°R as the reference temperature were performed and compared to the 2200°R calculations. For moderate $\rho_b R_o$ (as in Table 3), the differences in $u_o$ compared to the 2200°R reference calculations were small, being about 7 to 8% on the average for various $\Gamma$ and $z_e$. For low $\rho_b R_o$ (as in Table 5), using 2100°R as the reference temperature, the applicable range of $\Gamma$ and $z_e$ for realistic fire whirls would be greatly reduced. For instance, no whirls are predicted for $z_e > 5000$ ft for achievable $\Gamma$, and the lower $z_e$ results are also greatly restricted. Using 2300°R as the temperature for the reference case, then for small $_bR_o$, the small $z_e$ cases are restricted to low $\Gamma$ in order to avoid unrealistically high burn rate enhancement ratios. In addition, the core velocities for low $\rho_b R_o$ quickly exceed those for moderate $\rho_b R_o$ as $\Gamma$ increases, which is physically unrealistic. At large $\rho_b R_o$, the higher temperatures result in a more restrictive applicable $\Gamma$, $z_e$ range. Hence, it was found that the choice of a reasonable temperature for the reference case does not strongly affect the results for moderate values of $\rho_b R_o$, but the 2100 and 2300°R reference temperatures cause a more restricted range for both low

and high $\rho_b R_o$. For these reasons, 2200°R was chosen for the reference case, leading to Eq. (53). It has already been shown that the resulting calculations give reasonable results relative to observed whirls and produce physically plausible and expected trends.

The results given in Tables 3 through 7 relate the core variables to the input parameters. Also of interest is the ground boundary layer inflow velocity. The analysis used here does not directly contain the radial inflow velocity as a variable. The ground boundary layer mass inflow into the core can be readily obtained, and from this an indication of the expected boundary layer radial inflow velocity can be acquired. The mean radial velocity $v_r$ at the entrance to the core (at $r = a_o$) is given by

$$2\pi a_o \delta \rho_\infty v_r = \pi a_o^2 \rho u_o - \dot{M}_f \equiv Q_m \tag{55}$$

where $\delta$ is the boundary layer thickness at the entrance to the core base. Once $\delta$ is estimated, $v_r$ can be readily obtained for a given case. The results for $v_r$ for the UCSB subscale experiments were discussed in Section IV-D-1.

The theory of Rott and Lewellen[17] is used here to obtain an estimate of $\delta$. For $\rho_b R_o = 0.1165$ $lb_m/ft^2$-sec, $\Gamma = 3000$ $ft^2/sec$, $z_e = 2000$ ft, $d = 4/900$ ft, an estimate of 102 ft/sec was obtained for $v_r$, with $v_r \propto Q_m/a_o^{3/2}$. Estimates for various cases are given in Table 8, showing that $v_r$ is generally in the 100 to 200 ft/sec range. This is large enough to feed air (and new fuel material) into the core. The radial velocity is approximately inversely proportional to the radius (to the distance from the core centerline), so that the boundary layer radial velocity quickly diminishes as the distance from the core increases. Thus, only ground debris close to the fire whirl are expected to be drawn into the core. This implies that a stationary fire whirl is expected to have a shorter life than one that is moving around the fire area.

Table 8. Boundary Layer Radial Inflow Velocity at Core Base, for d = 4/900 ft

| Case | | | |
|---|---|---|---|
| $\Gamma$, $ft^2/sec$ | $z_e$, ft | $\rho_b R_o$, $lb_m/ft^2$-sec | $v_r$, ft/sec |
| 3000 | 2000 | 0.1165 | 102 |
| 3000 | 8000 | 0.1165 | 90 |
| 10,000 | 8000 | 0.1165 | 209 |
| 10,000 | 2000 | 0.3 | 165 |
| 10,000 | 8000 | 0.3 | 164 |
| 3000 | 2000 | 0.3 | 81 |

Sections IV-D-1 and IV-D-2 present the correlation of the fire whirl model to the subscale experiments and its extrapolation to full scale whirls. The correlation of the model to the UCSB experiments enables a' and T to be determined in terms of input quantities. The experiments also help to check the appropriateness of some of the assumptions in the model and to thus increase confidence in its use. The primary input parameters to the problem are $\Gamma$, $z_e$, $\rho_b R_o$, and d. In an actual case these may not all be independent. While $\rho_b R_o$ can presently be obtained using the Rothermel model[3], $\Gamma$ and $z_e$ as functions of wind, terrain, and fuel characteristics need to be determined. The problem addressed here is the determination of the fluid mechanical properties of a given fire whirl (given values of $\Gamma$, etc.), and not the initiation of a fire whirl. While the jump from the subscale UCSB experiments to a full-scale fire whirl is a large one, the results and trends predicted by the full-scale model are reasonable and physically plausible. The model is relatively simple to employ and requires only a small number of input parameters.

3. Firebrand Trajectory Calculations

The formulation of the firebrand trajectory model is given in Section IV-C. The model consists of a core, an ambient swirl, and a wind region. The full equations of motion are used in the first two regions and upon entrance into the latter. The full equations indicate that once the firebrand is out of the high acceleration core and swirl regions and into the wind region, it quickly attains the wind velocity and falls at its instantaneous fall velocity. The simplified equations, Eqs. (46) and (47), are then used.

The core trajectory model was applied to the UCSB firebrand tests described in Section V. One-half-inch long balsa sticks having a density of 16 $lb_m/ft^3$ were released at z = 45 in. at various radial positions within the core, and photographs were taken of their subsequent trajectories. These tests were conducted for a crib diameter of 6 in., a 0.5 packing ratio, and for a 5-in. fuel stick height. Both 1/16- and 1/8-in. square cross section firebrands were used. Trajectory calculations were performed for firebrands released with their lengths in the radial direction, and the results were compared with the photographs.

The photographs show that the firebrand sticks tended to adhere to the holder rod and were given a rotation as they were lifted. For these subscale-sized firebrands in the subscale fire whirl, the Reynolds numbers are low enough so that viscous drag effects need to be considered, indicating that the local orientation is important. For the rotating balsa sticks at low Reynolds number, both the pressure and the viscous drag effects are important. When the results of Hoerner[18] and Delany and Sorensen[19] were used, the drags for broadside and end-on orientations were obtained and averaged, yielding an average value of the drag coefficient of 1-1/4, based on the broadside area as the reference area.

The full set of equations, Eqs. (41) through (43), were cast into six first-order differential equations, which were solved numerically using a fourth-order Adams-Moulton predictor-corrector method with the classical fourth-order Runge-Kutta method used for starting. The core gas vertical

and azimuthal velocity distributions as given by the fire whirl model are used in the equations. The vertical velocity measured at z = 45 in. was 31.6 ft/sec, and this was used as the gas velocity at the core centerline.

Calculations were performed for centerline release of both the 1/8- and the 1/16-in. balsa sticks and compared with the trajectories as inferred from the high speed photography. Figures 16a-f show the flight of a 1/8-in. square cross section balsa stick released at the core centerline. As expected, the balsa is lifted vertically. The frame speed is 48 frames per second. Prior to the tests, a ruler was placed at the rig centerline at approximately z = 45 in. and photographed, allowing for a measurement of distance in the photographs. The trajectories considered were in the first few inches of travel following release of the sticks, so the distortion of distance in the photographs should not be large. The comparison of the calculated and photographed trajectory for this case is shown in Fig. 17. Figure 18 shows the trajectory comparison for a 1/16-in. square cross section stick released at the centerline. The comparison for the 1/8-in. sticks is very favorable, while the predicted rise of the 1/16-in. sticks is faster than indicated by the photographs. For release at the core centerline, the theory predicts the firebrand will remain on the centerline, and this is borne out by the photographs.

Calculations were also performed for a 1/16-in. stick released at r = 1/2 in. (1/2 in. from the core centerline). Away from the centerline, the balsa is expected to be centrifuged outward by the azimuthal component of the core gas velocity, and to eventually leave the core. Figure 19 shows the calculated and photographed trajectory for this case. The mean upward velocity over the outer portion of the core at z = 45 in. is about 23 ft/sec. Calculations were performed for vertical gas velocities of 22.2 and 23.8 ft/sec, and results for both are shown in Fig. 19. The balsa stick leaves the core (r ~ 1.5 in.) approximately 0.15 sec after its release. The computed radial history of the stick agrees well with the photographs. (The radial history computed for both the 22.2 and the 23.8 ft/sec velocities are practically the same, and only one predicted radial history plot is shown in Fig. 19.)

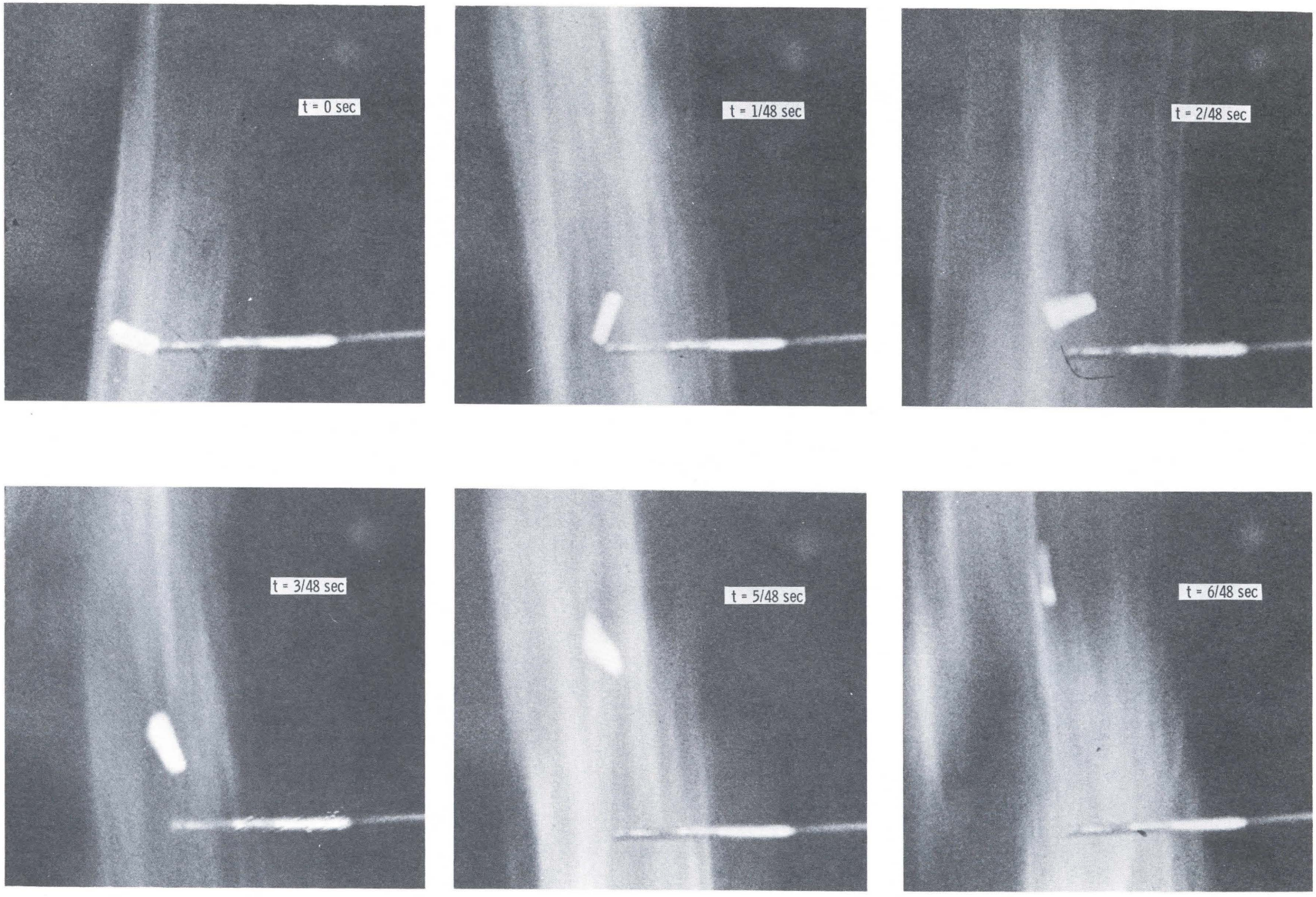


Firebrand - Balsa wood cylinder 1/8" 1/2" in fire whirl core center.
Fire whirl - 6 " crib diameter; 5 " stick height; 0.5 packing ratio.

Fig. 16. Firebrand Trajectory Experiments

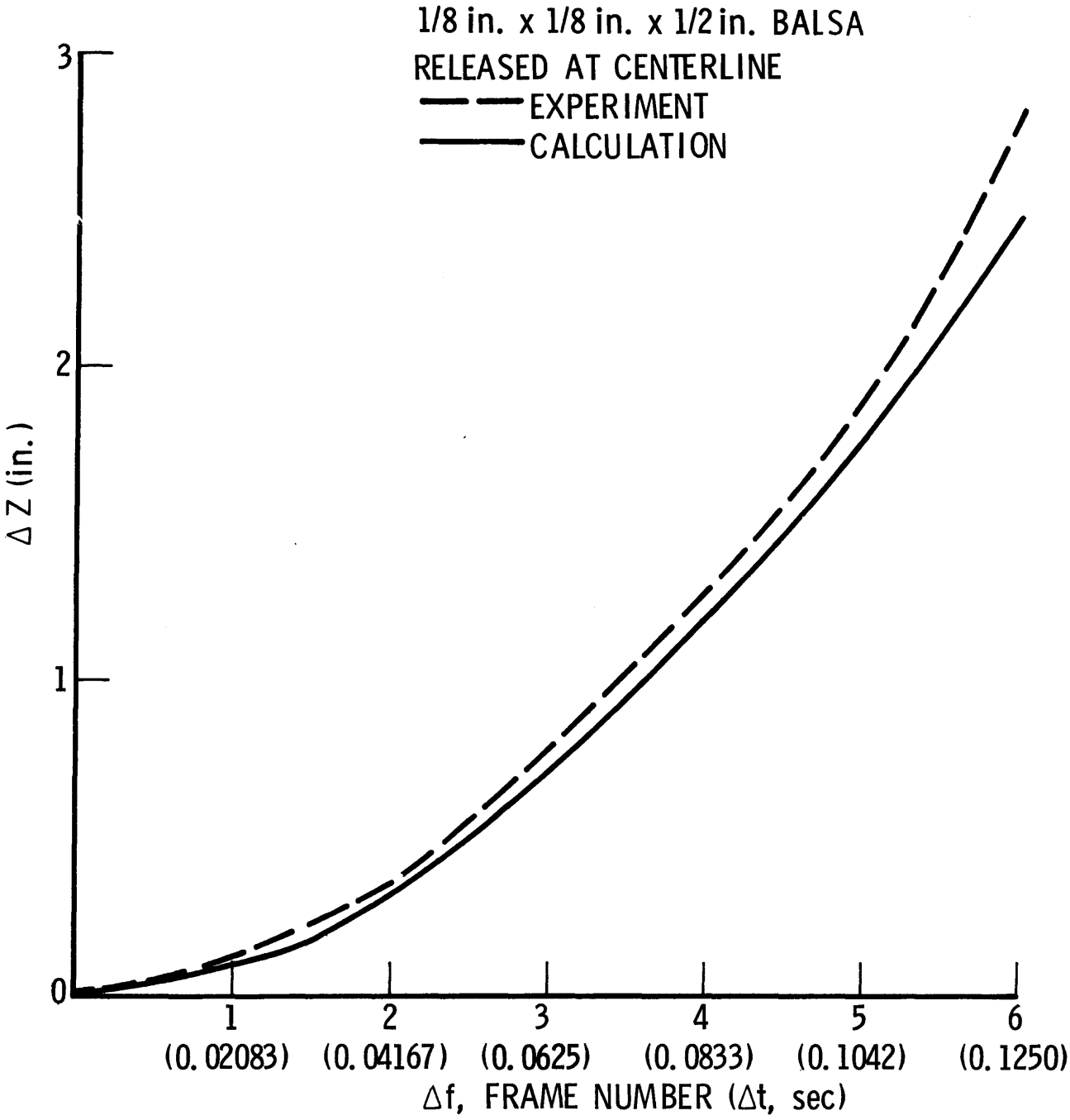


Fig. 17. Firebrand Subscale Trajectory, Height vs Time

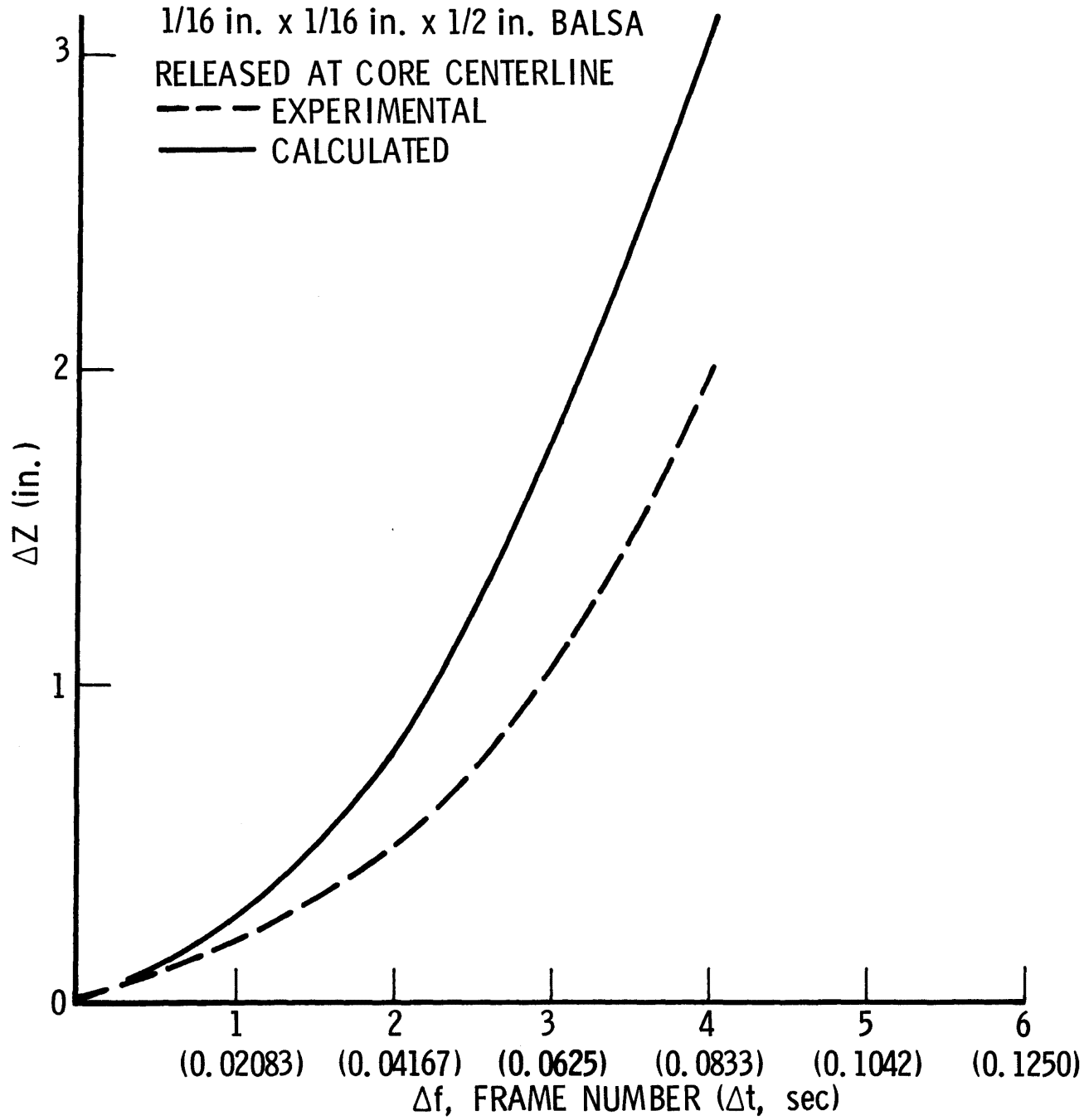


Fig. 18. Firebrand Subscale Trajectory, Height vs Time

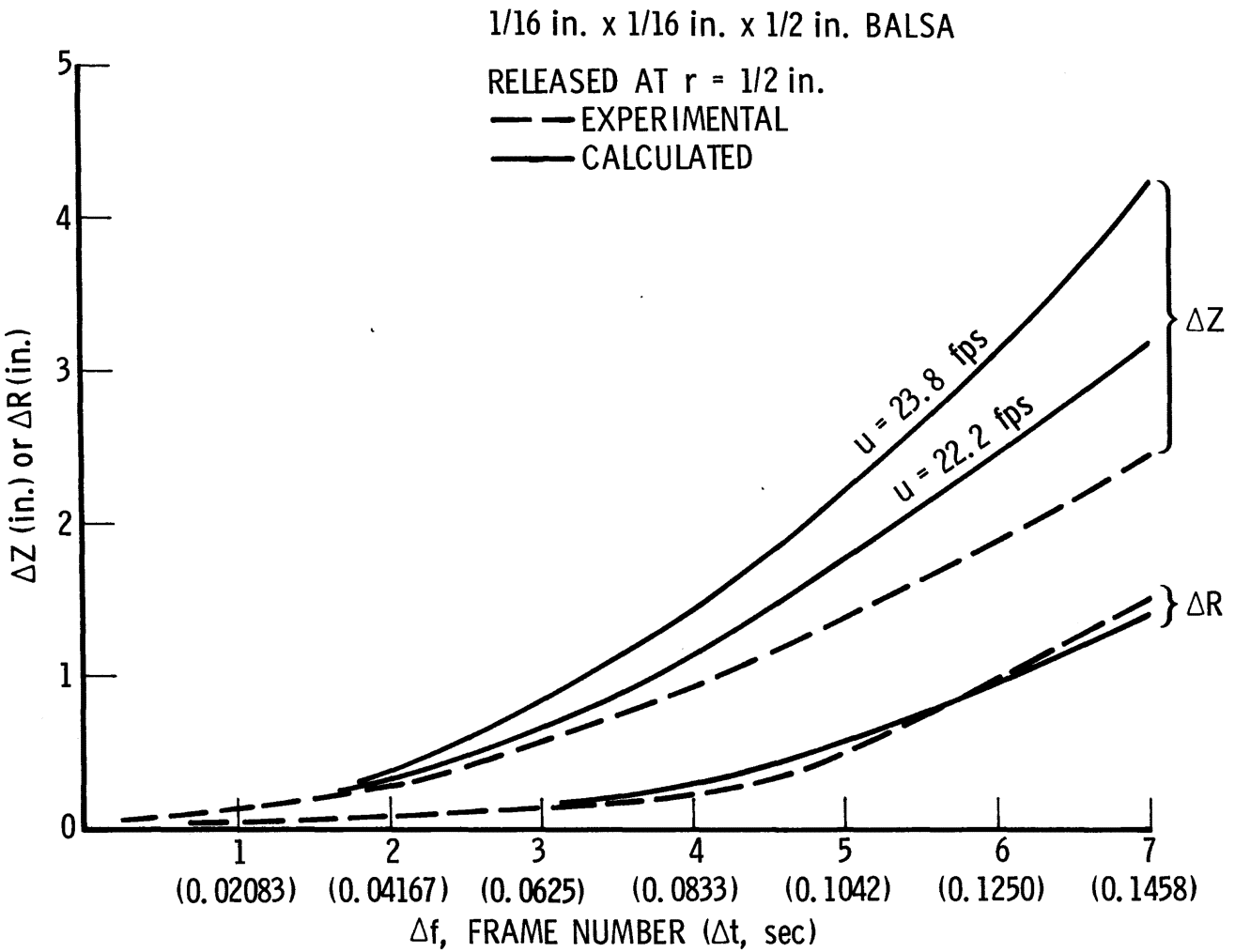


Fig. 19. Firebrand Subscale Trajectory, Height and Radial Position vs Time

The vertical rise of the stick is slightly overpredicted. For this case, it is predicted that the stick will be displaced azimuthally about one-fourth of the circle. While changes in the azimuthal position of the stick cannot be quantitatively ascertained by the photographs, apparently little azimuthal displacement occurred.

The above comparisons show favorable agreement in the lift characteristics of the balsa sticks. The vertical lift characteristics are the most important. Overall, the comparison is favorable. The equations of motion used are standard. Due to the subscale core conditions and the small firebrand size used, low Reynolds number effects must be included in determining the drag of the tumbling firebrand. This leads to some uncertainty in the drag coefficient, so it is gratifying that the comparisons are favorable. For full-scale conditions, the flow Reynolds numbers both in and out of the core are in a regime where the drag can be well characterized.

Full-scale calculations were made for a specified fire whirl and wind. The intent was to demonstrate typical results for cylindrical and for flat firebrands of varying initial size and density. Tarifa[5] found that $C_D = 1.2$ was appropriate for cylinders. This agrees with results found in Hoerner[18], which also shows that $C_D = 1.2$ characterizes the broadside drag of flat plates. Tarifa's observation that the classical broadside drag of firebrands characterized their motion was utilized. These observations are relevant to the relatively high Reynolds number regime applicable to full-scale conditions.

The full-scale calculations were performed for the following core conditions: $\Gamma = 3000$ ft$^2$/sec, $z_e = 2000$ ft, $a_o = 10$ ft, $u_o = 475$ ft/sec. In order to expedite the calculations, they were performed before the fire whirl model was fully developed. Looking back now on the fire whirl calculations, it is seen that these core conditions are indicative of a high fuel loading (high $\rho_b R_o$) and/or a large $\sigma$ (small d). The wind was taken to be horizontal with a velocity of 30 ft/sec. For these conditions, the Region II-III boundary is at a radius of 100 ft. Calculations were performed for birch and pine cylinders of

diameters ranging from 1/4 to 2 in., with a length to diameter ratio of 4, and for birch and pine wood square plates and Ponderosa pine bark square platelets of 2-, 4- and 8-in. widths and a width to thickness ratio of 16.

The firebrands are assumed to be initially at the ground. From Eq. (41) it can be seen that a firebrand can be initially lifted if $\alpha > \beta$. One of the most important parameters in determining the trajectory of the firebrand is its initial radial position within the core at liftoff. Table 9 shows the effect of the initial relative radial position $\gamma [\gamma = r(o)/a_o]$ for a given cylindrical firebrand, for two firebrand orientations. The broadside orientation (maximum drag) is the one seen by Tarifa to be relevant to the flight of a firebrand. In this orientation, the firebrand is broadside to the relative velocity vector. Also shown are results for the firebrand being broadside to the vertical velocity, but end-on to the azimuthal velocity. With this orientation, the firebrand does not experience as large a centrifugal force, enabling it to remain in the core (Region I) longer and to reach a greater height before it crosses the core boundary into Region II. (There is no uplift velocity outside the core.)

For both orientations the maximum range generally decreases as $\gamma$ increases, as expected. The farther away from the centerline the firebrand is initially, the more pronounced the centrifuging effect, since, within the core, the gas azimuthal velocity increases with r. As expected, the range is generally greater for the end-on orientation. However, if the firebrand is initially too close to the centerline, it may reach its maximum height while inside the core, and might be falling within the core as it leaves the core. For $\gamma = 10^{-4}$, this is the case with the end-on configuration, giving a smaller range than for the broadside orientation or for end-on with the larger value of $\gamma$ of 0.01. For $\gamma = 10^{-4}$ (very close to the center of the core), the firebrand reaches a height of 1715 ft (the core is 2000 ft high), and starts to fall, falling to a height of 1528 ft as it moves radially outward. Before it leaves the core, it again starts to rise, leaving the core at a height of 1542 ft. For this case, the end-on orientation produces a smaller range than the broadside. For smaller $\gamma$ the reverse is true.

Table 9. Effect of Initial Core Radial Position and Firebrand Orientation on Maximum Firebrand Range: $D_o = 2$ in., $L = 8$ in., $\rho_{w_o} = 30\ lb_m/ft^3$ (red pine)

| $\gamma$ [$\gamma = r(o)/a_o$] | Maximum Range, ft | | Maximum Cross Range, ft (normal to wind) | |
|---|---|---|---|---|
| | End-on to Swirl | Broadside to Swirl | End-on | Broadside |
| ~centerline | | 1075 | | 175 |
| $10^{-4}$ | 830* | 965 | 100* | 190 |
| 0.01 | 900 | 500 | 245 | 190 |
| 0.10 | 450 | 320 | 210 | 180 |
| 0.25 | 300 | 280 | 175 | 172 |

*Maximum height reached within the core

For the broadside orientation, conditions may also exist (depending on $u_o$, $z_e$, and the firebrand properties) whereby the firebrand may reach its maximum height within the core before it leaves the core. The most favorable radial location (for largest range) is very close to the core centerline, so that the firebrand reaches its maximum height as it leaves the core. Under optimum conditions of firebrand size and weight, and core velocity and height, a firebrand can be lifted close to the full height of the core $z_e$. Table 9 shows that the maximum cross range (normal to the wind) is not strongly dependent on $\gamma$ or orientation, and is roughly twice the radius of the Region II outer boundary. The maximum cross range decreases for less dense or smaller firebrands, becoming closer to the Region II radius. Hence, for a unidirectional wind, the firebrand corridor is relatively narrow. The broadside orientation is the relevant one, according to Tarifa[5], and all subsequent calculations shown here will be for that orientation.

Figures 20 through 23 present results for birch (density = 41 $lb_m/ft^3$) circular cylinders of various sizes for a near-centerline initial radial position. Figure 20 shows the horizontal projection of the trajectory of a typical firebrand, indicating the swirling motion of the firebrand in Regions I and II caused by the centrifugal forces. Figure 21 shows the core and the firebrand vertical velocity as a function of height. The firebrand is quickly accelerated to a peak velocity within the core, following which its upward velocity decreases. It leaves the fire whirl (Region I) at a height of about 1800 ft still having an upward velocity. It is further decelerated in Region II and begins to fall, leaving the ambient swirl region (Region II) at a height of 1760 ft. At a height of 1705 ft, within Region III, its downward velocity equals its fall velocity. (The firebrand is seen to quickly reach its instantaneous fall velocity and wind velocity after it enters Region III.) As the firebrand continues to fall, it burns as it falls and its downward velocity equals its instantaneous fall velocity as it travels horizontally with the wind. Figure 22 gives the weight change of that firebrand (as well as those of two other sizes) as it falls and is carried by the wind. The firebrand with the initial 1-in. diameter has three-fourths of its initial weight at impact with the ground.

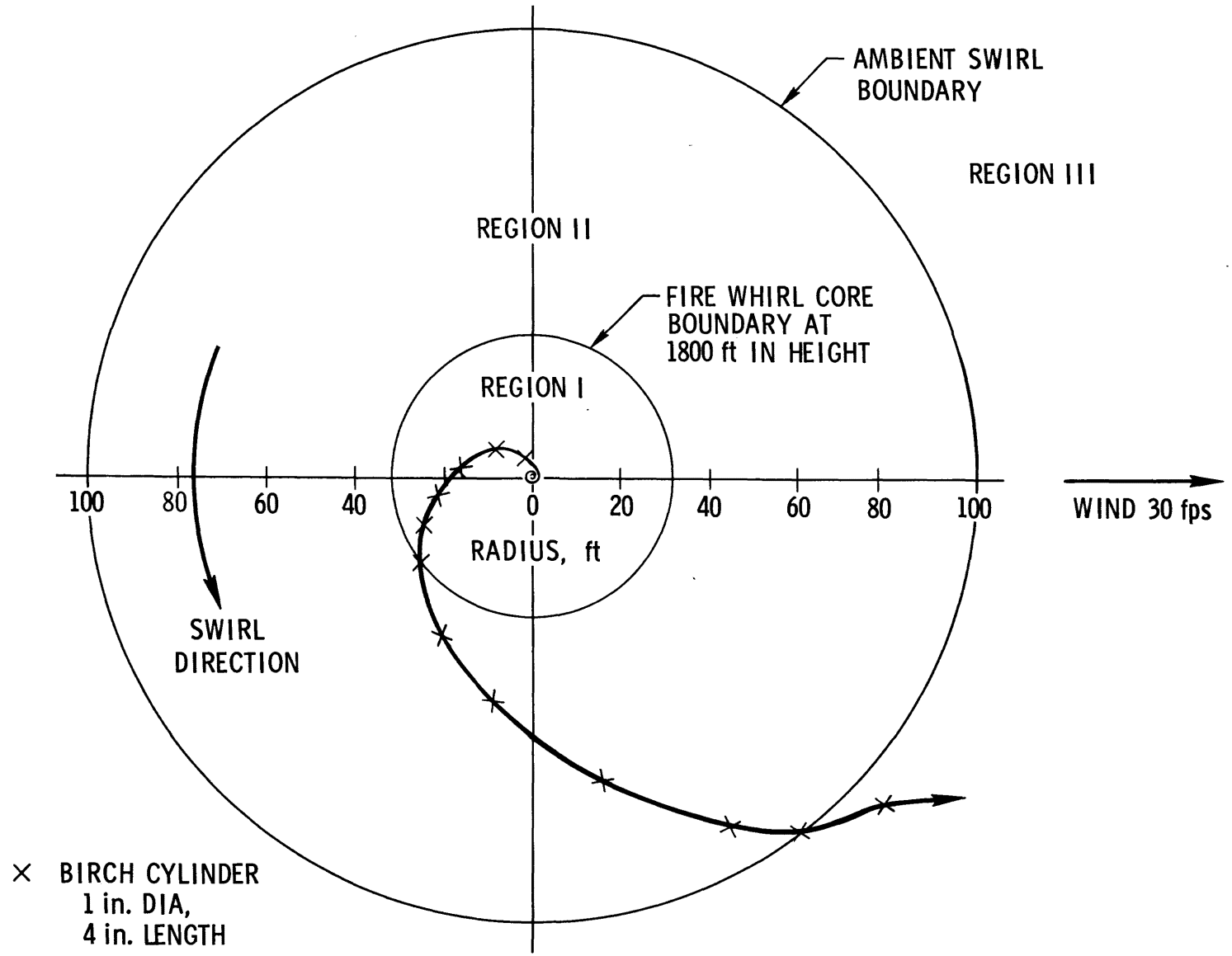


Fig. 20. Azimuthal Trajectory of a Firebrand in the Swirl

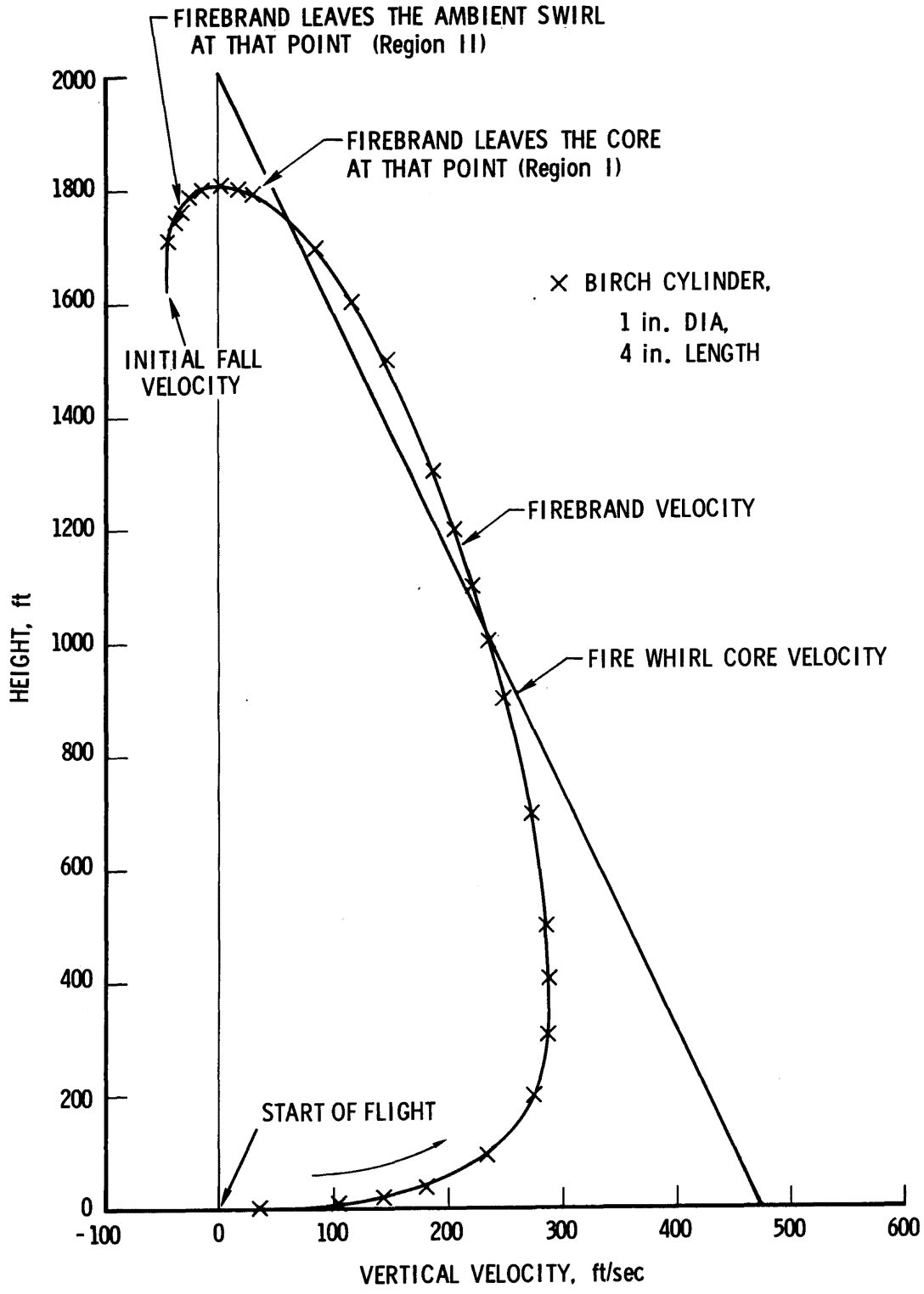


Fig. 21. Fire Whirl Core and Firebrand Vertical Velocity

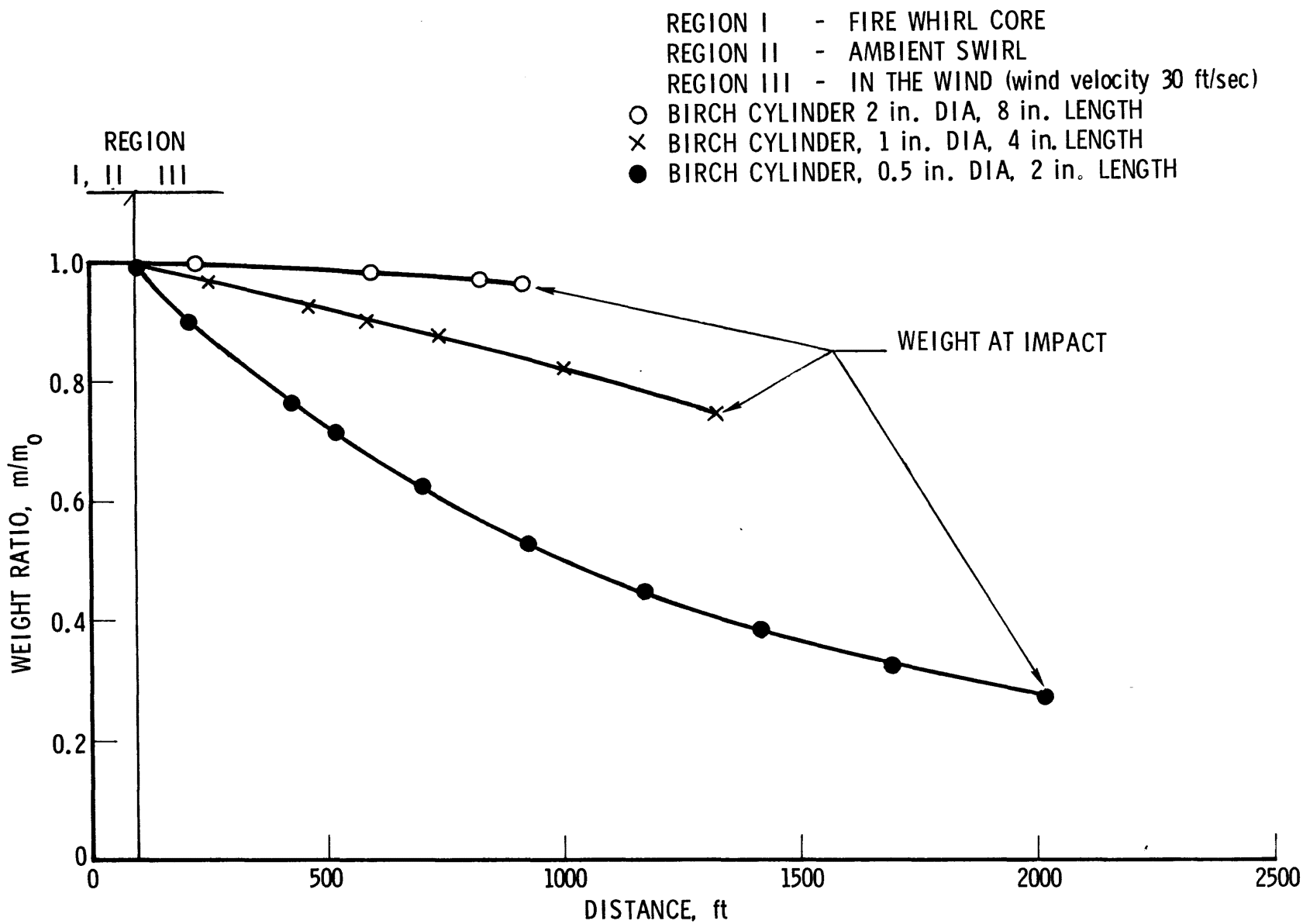


Fig. 22. Firebrand Weight Change in Flight

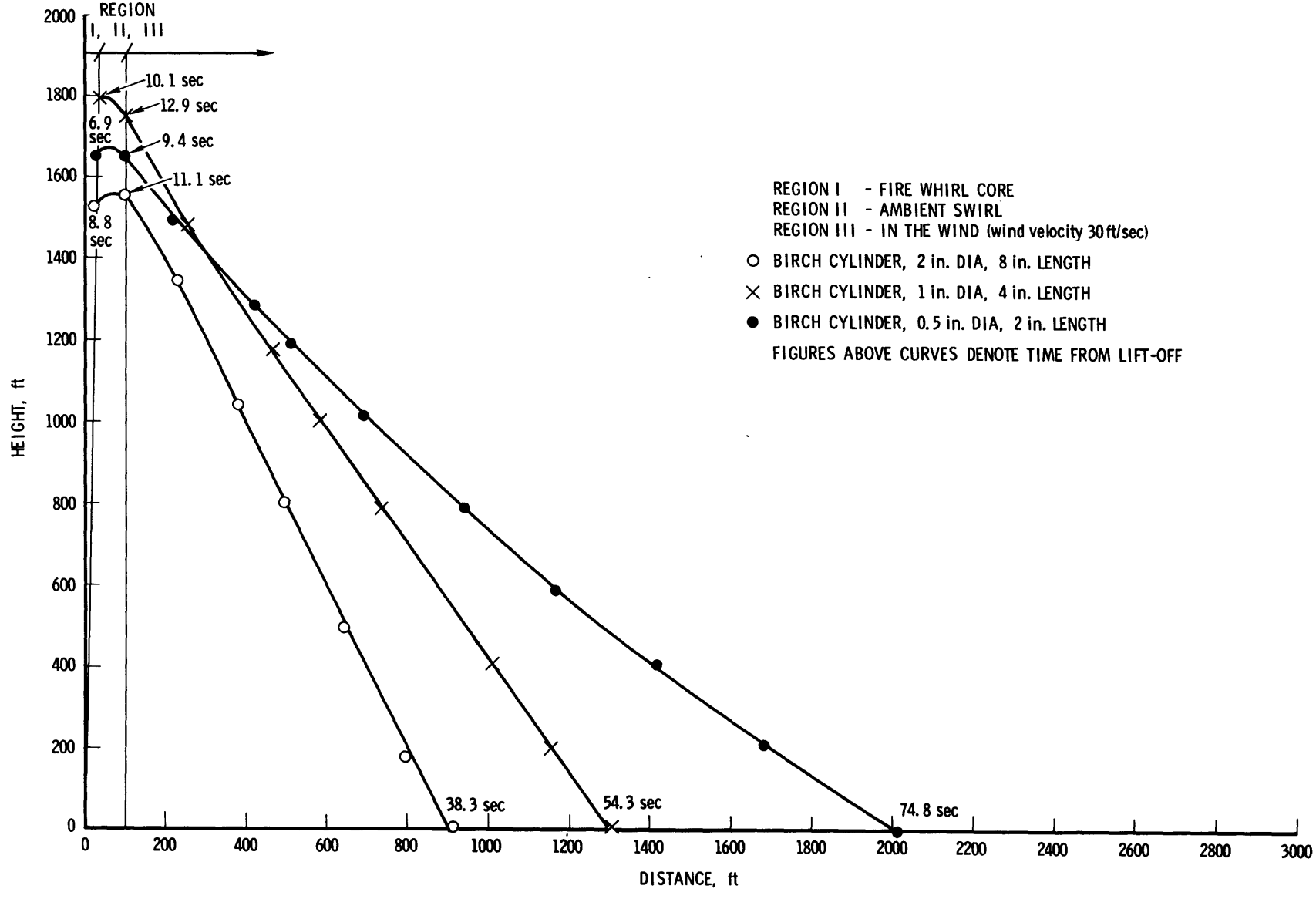


Fig. 23. Firebrand Trajectories In and Out of the Fire Whirl

Figure 23 shows the trajectories of three birch firebrands of 0.5-, 1-, and 2-in. initial diameters. Generally, the smaller the firebrand, the greater its range, unless it burns up in flight. The $D_o$ = 0.5-in. firebrand actually leaves the core before the $D_o$ = 1-in. firebrand. But once into the wind region, the larger broadside area to weight ratio of the $D_o$ = 0.5-in. firebrand gives it a smaller fall velocity and allows it to remain aloft longer, thereby giving it a greater range. At impact with the ground its density was 0.27 of its original density. The density ratio at impact for the $D_o$ = 1- and 2-in. firebrands was 0.77 and 0.96, respectively. Calculations were also made for a 1/4-in. diameter firebrand. It burned up in flight, reaching a density ratio of 0.05 at an altitude of 686 ft at a range of 1450 ft. Thus, for the four sizes calculated, the $D_o$ = 0.5-in. one had the largest range. The maximum range and optimum size depend on the core properties and firebrand density.

The times at which the firebrands leave Regions I and II, and the time at impact, are also given in Fig. 23. The time spent in the core is small, with the time spent in Region II even smaller. (In fact, if Region II were neglected, the error in range would be on the order of one or two Region II radii, which is relatively small.)

Figures 24 and 25 show in-wind firebrand trajectories for flat plate configurations. These firebrands, having a large drag area to weight ratio, can be lifted essentially to the top of the fire whirl if they are initially sufficiently close to the center. For a core height of 2000 ft, Fig. 24 gives trajectories for 4-in. square flat plates of various wood types. The lightest one, representing a piece of bark, has the greatest range. (Bark is known to have a high spot fire potential.) Calculations for a 2 x 2 x 1/8-in. Ponderosa pine bark platelet showed that it burned out in flight after 238.5 sec. The final densities for the firebrands of Fig. 24 are 0.69, 0.83, and 0.88 of their initial densities, for the bark, pine, and birch plates, respectively. Figure 25 shows Ponderosa pine bark trajectories for different core heights. These bark platelets can be carried a long way by the wind, and are a long-range spot fire

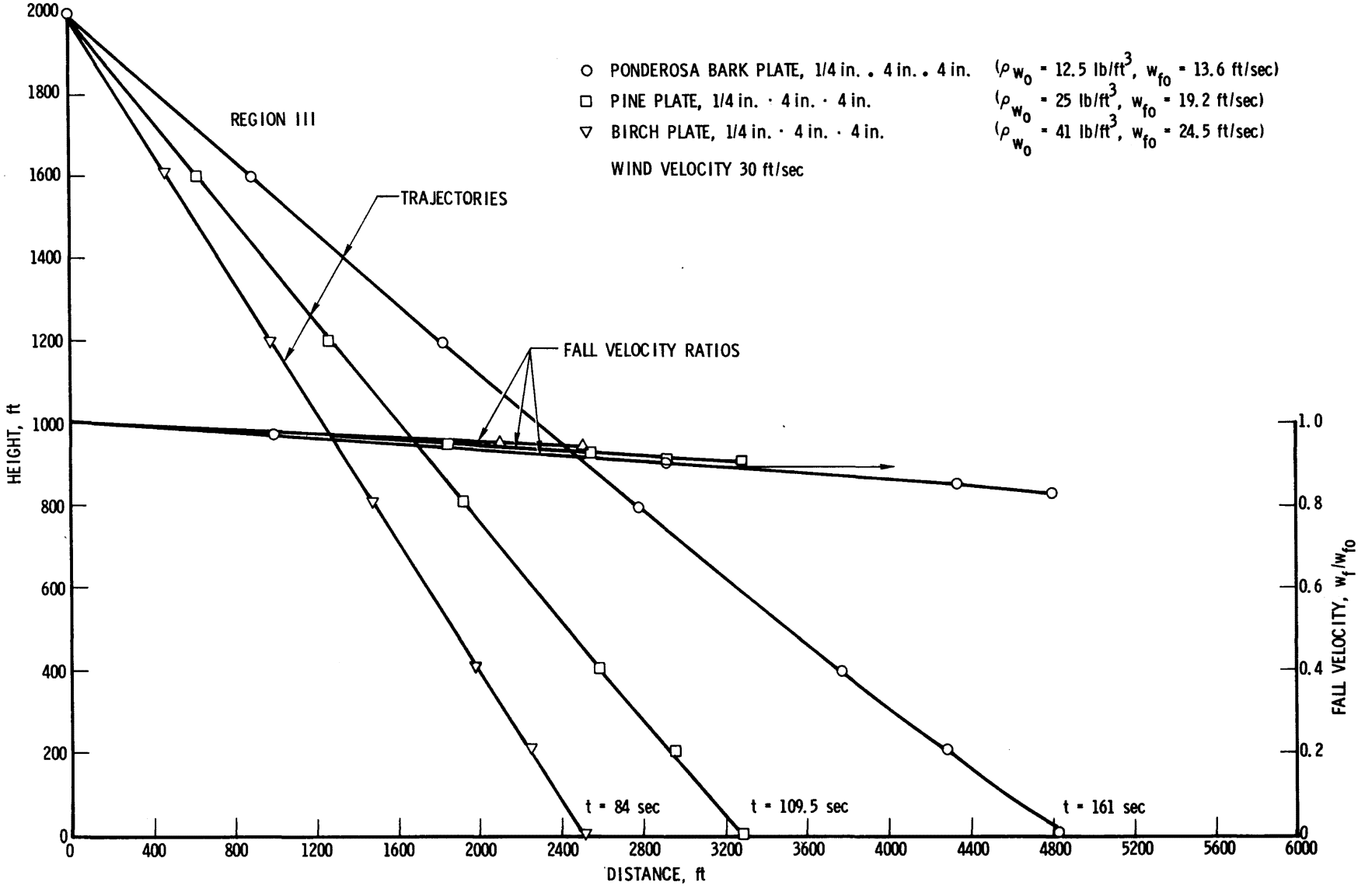


Fig. 24. Firebrand Trajectories In-Wind for Various Woods

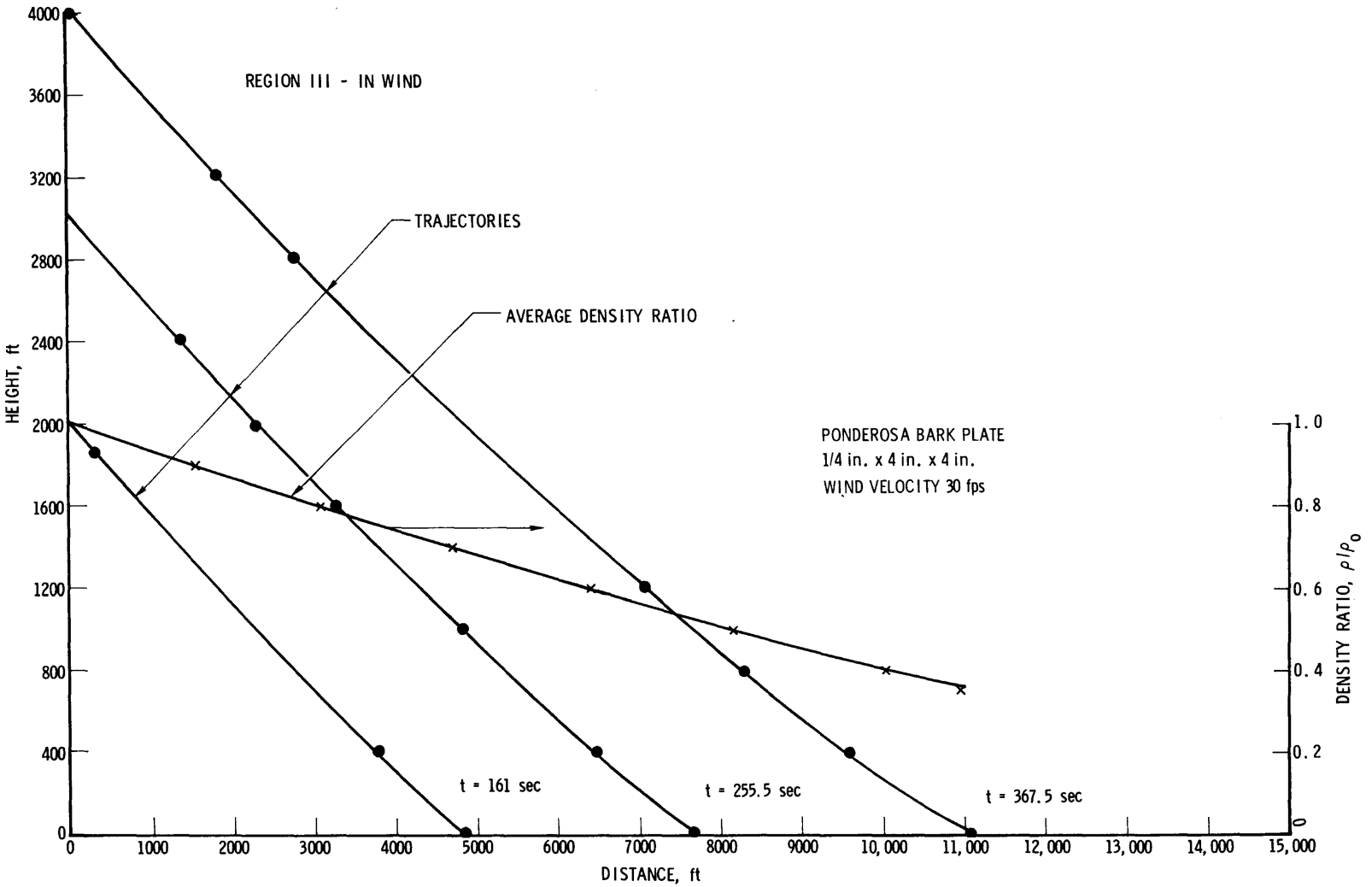


Fig. 25. Firebrand Trajectories In-Wind from Various Initial Heights

threat, with the 4 x 4 x 1/4-in. plate having a range of over 11,000 ft if it enters the wind at a height of 4000 ft. Its impact density is 0.35 of its initial mass, indicating that it can have a greater range, without burnout, if it is lifted to greater heights.

Firebrand trajectory calculations for spherical firebrands have also been reported by Lee and Hellman[20]. While their analysis assumed that the firebrand initially starts out with the local core velocity, they also found that firebrands can have large ranges, and that their initial radial position is very important.

In determining the maximum firebrand range, the most important fire whirl parameter is $z_e$, the vertical extent of the ambient circulation, since this gives an indication of the firebrand lift heights that can be achieved. If the core vertical velocity $u_o$ is large enough initially, then a given firebrand, if it is initially sufficiently close to the core centerline, can leave the core very near its top, giving it a large range. The value of $a_o$ is not critical in determining maximum ranges. The maximum range of a firebrand depends on $D_o$, $\rho_{w_o}$, and $z_e$, for a sufficiently high $u_o$. (The range, of course, also depends on the wind.) If $u_o$ is not large enough to lift a given firebrand size and weight to near the top of the core, then $u_o$ also determines the range. For firebrands initially away from the core centerline, their relative radial position $\Upsilon$ is very critical in determining their range. However, since a fire whirl is moving around, it may be assumed that at any time there will be a number of potential firebrands in a good radial position for lifting.

The firebrand trajectory model can be used independent of the core flow field model. The trajectory equations are basic, and require a core flow field as an input. If desired, another core model could be utilized. Similarly, the core model could be separately used with another trajectory model.

# V. EXPERIMENTAL WORK

## A. INTRODUCTION

In the experimental program described herein, fluid dynamic and thermodynamic variables were measured in a typical fire whirl. These fire whirls were generated using two different fuels; namely, a pool of acetone and a prepared crib of 1/4-in. pine sticks. In general, the variables measured were the mass burn rate of the fuel, the vertical and tangential velocity profiles, and the temperature profiles. Previous results of this program have been reported by Postolka[21] and Muraszew, Fedele and Kuby[2]. Postolka gives details of the experimental apparatus and instrumentation, and this information will only be summarized in this report. Changes and improvements in the instrumentation will be emphasized in Section V-B.

In addition to a description of the improvements in the instrumentation, the test procedures and data acquisition will be reviewed. Also, the results for the two fuels will be presented. The test data with acetone will be shown in Appendix B. Muraszew, Fedele and Kuby[2] give additional details for the acetone tests.

## B. EXPERIMENTAL APPARATUS AND INSTRUMENTATION

The experimental apparatus consists primarily of two 3-ft diameter, 6-ft length cylindrical sections topped by a truncated conical section which is also 6 ft in length and has an outlet diameter of 1.5 ft. The bottom section is fitted with five pairs of tangential forced air inlets (forced air swirl inducers or FASI) which are fed by an air blower. The mass flow rate through these tangential inlets can be controlled, and the total flow measured by measuring the pressure drop across a square-edged orifice. The mass flow is then calculated by the normal procedure.

The second cylindrical section originally was an open-screened section. It was found that this configuration damped the circulation. Later in the program, the screen was covered by a plastic sheet and, with this new

configuration, a larger circulation and more stable fire whirl core were maintained under a variety of ambient conditions.

An 8 x 8 ft flat table is installed directly below the bottom cylindrical section. This table has the capability of being raised or lowered to vary the air gap below the apparatus from zero to seven inches. In this manner, the amount of open boundary layer air space is controllable. During the program, it was determined that the FASI were not capable of sustaining adequate circulation. Therefore, tangential boundary layer inlets (TBLI) were installed similar to those used by Byram and Martin[6]. In the current configuration, there are six of these tangential inlets. This final design required extension of the inlets to minimize the effects of ambient wind. There are two sets of these inlets, each of different height. The thin set of inlets provides an inlet area equivalent to a boundary layer gap of ~0.45 in., compared to ~0.90 in. for the thicker set. They can be used together to give an equivalent boundary layer gap of 1.35 in. With this final configuration, stable whirls have been established and maintained in the experiments.

In the center of the variable height floor, the fuel is placed on a weighing system which will be discussed in more detail. For the acetone tests, a fuel reservoir is mounted at the top of the first cylindrical section, from which fuel can flow at a controllable rate through copper tubing to a dish on the weighing system. This continuous flow system provides the option of running on either of two bases: burning continuously or burning a given amount of fuel placed in the dish. The acetone in the dish is ignited by arcing two electrodes above the surface of the fuel. For the wood crib tests, the cribs are placed on the weighing system, and the excelsior fuel placed in the middle of the sticks. The excelsior and sticks are then sprayed with acetone and ignited manually.

The instrumentation provided for the following measurements. First, the burn rate is obtained by continuous weighing of the fuel during the burning process (for the wood and for a given amount of acetone). Circulation profiles are obtained by measuring the tangential velocity at three heights within

the bottom 6-ft section. These are done by the use of pitot tubes which can be positioned manually at any radius from zero to the wall position. Likewise, at the same three heights, the temperature profile can be obtained using a chromel-alumel thermocouple probe which, again, can be manually positioned at any radius from zero to the wall. Finally, a rotating pitot tube provides measurement of the magnitude and direction of the velocity in the core as a function of radius at the three heights. Additionally, three boundary layer dynamic pressure rakes are used to obtain boundary layer velocity profile data.

The fuel burning rate is obtained by continuous measurement of the fuel weight during the burning process. This is done using a cantilever beam weighing system. The fuel is supported on the end of the aluminum cantilever beam. Strain gages are attached to the cantilever beam to measure the strain. Two gages are used with one on top of the beam in tension and the other on the bottom in compression. The output is fed through a low pass filter before recording in order to filter out the high frequency oscillations the dish undergoes during the burning process.

The cantilever beam system is attached directly below the movable floor, and a support to hold the fuel protrudes up through a circular hole in the center of the floor. The height of the fuel base above the floor is controlled by the use of inserts in the support column. By necessity, there must be some clearance between the floor board and the fuel base so that interference with the weight measurement is avoided. Also, for the acetone tests, maximum flame stability results when the dish lip is approximately 1/4 in. above the floor. Since the pressure just above the fuel in the burning region will be lower than the ambient pressure, air will be sucked through this gap if provisions are not made to exclude it. Consequently, the entire beam apparatus is sealed so that air cannot be admitted through the central hole in the floor. Thus, a constant pressure is maintained below the floor with no net flow into the combustion region from below. However, these two pressures are not identical due to the radial variation in pressure directly above

the burning surface. Consequently, upon ignition there is a shift in the indicated zero of the weight output, and when the flame goes out a shift in the other direction occurs. However, during the steady-state burn period, the slope of the weight curve is constant and unaffected by this variation.

As indicated, both circulation and core velocities are measured using pitot tubes. The swirl velocity pitot tubes are 1/8-in. in diameter and placed at vertical heights of 17, 45, and 71 in. above the floor. The pitot tubes can be manually slid to any position to obtain a radial distribution of circulation velocity in regions where there are no other significant velocity components. For the experiments described in this report, the pitot tubes are long enough to allow a scan all the way to the centerline. The pressure difference output of these pitot tubes is measured using a Decker $\Delta p$ Transducer Type 360.

Chromel-alumel thermocouple probes are also provided at the same three heights as the swirl velocity measurements: 17, 45, and 71 in. above the floor. These probes also can be slid to any radial position from the actual core centerline to the wall. The millivolt output of the thermocouple is referenced to an ice bath and recorded directly.

In order to determine the amount of air being ingested into the flame, the floor boundary layer profile is measured using dynamic pressure rakes. These are referenced to a static pressure directly in line with the dynamic probe inlets. In order to obtain circumferential variation and increase the vertical detail, three probes are installed in the boundary layer 120 deg apart. In a given run, the dynamic pressures as referenced to one of the static pressures are measured sequentially. Additionally, the other two static pressures are referenced to the reference static pressure and included in the sequential record. Thus, the velocity profile can be determined at various heights above the floor and at the three circumferential positions. Obviously, the air entering the column in the vicinity of the core is not entering in a purely radial direction. To compensate for this, the boundary layer rakes can be rotated to line up with the direction of the boundary layer flow, thus maximizing the accuracy of the velocity measurement.

Early in the program, the tangential velocity outside the core (as indicated above) and the vertical velocity in the centerline were measured. However, it was desired to obtain complete profiles of the velocity both in magnitude and direction. Unfortunately, a pitot tube cannot be used to measure the tangential and vertical components of a flow which is spiraling upward since each measurement would be invalidated by the flow entering the static ports. To compensate for this problem, an apparatus was constructed which allowed rotation of the pitot tube about its tip, thus determining the position of maximum $\Delta p$, i.e., the alignment with the actual velocity vector. By measuring the angular position and magnitude, the actual velocity was determined. The pressure difference output of the pitot tube was measured using a Barocel Electronic Manometer Type 1083-57.

The measurements made in a given experiment were recorded using two Hewlett-Packard XY recorders and a Soltec Rikadenki 3-channel strip chart recorder. The XY recorders have their time bases ganged together for simultaneous sweep. Various $\Delta p$'s can be recorded sequentially during a given run through the use of a 12-port solenoid drive Scanivalve system. Thus, several data can be recorded on the five available recorder channels during a given run. Care must be taken that the period of measurement in sequential measurements is sufficiently long compared to fluctuation changes which occur in a given burning situation.

More details on instrumentation and measuring technique development are given in Appendix A.

## C. WOOD CRIB TEST RESULTS AND DISCUSSION

Using basically the same apparatus and instrumentation as used for the acetone burns (see Appendix B), the variables were measured in fire whirls generated with wood cribs. In all cases, these cribs were constructed using 1/4-in. square pine sticks. The final configuration for the wood cribs was to place the sticks in a vertical position, distributing them in a manner to generate a prescribed packing ratio, i.e., volume of wood per space unit

volume. The wood loading, i.e., the mass of wood per unit burn area, was controlled by using different length sticks to make up the crib.

It was found in early tests that cribs with low fuel loading ($\sim 0.5$ lb/ft$^2$) and low no-swirl burn rate could not produce stable fire whirls. Consequently, the fuel loading in the cribs was increased in square cribs to $\sim 1$ lb/ft$^2$ (packing ratio 0.2) and later in circular cribs up to 9 lb/ft$^2$ (with 0.5 packing ratio and 7.5-in. stick height). The resulting no-swirl burn rates varied from 0.75 to 2.27 lb/ft$^2$-min (see Table 10).

The wood sticks were held in the vertical position by inserting them in grooves in an aluminum plate (see Fig. 26), which was then placed on a beam balance similar to that described in Appendix A. In this particular case, since the total weight of the wood plus the supporting plate was much greater than the acetone pools, a new beam was constructed of a heftier cross section. However, the basic principles described previously were followed. Typically, the center of the wood crib was stuffed with excelsior, sprayed with acetone, and ignited. Thus, the wood cribs burned essentially from the center outward maintaining a circular symmetry about the center of the crib (see Fig. 27).

During tests with burning wood, considerable variation in the parameters was observed throughout the run, and these variations had to be considered in the data reduction process. Figure 28 shows a typical time variation of the fire whirl parameters during a run. In particular, each of the important parameters increases with time early in the run. During this time, the mass burn rate is quite low. This is probably due to the slowness of the ignition process as well as the difficulty in drawing air into the combustion zone through the large amount of wood that is not yet involved in the fire. Later, after the fire is well under way, the axial velocity and axial temperatures show a large rise. However, they do not reach their peak until much later in the run. The peak of all the parameters indicated, including the mass burn rate, occurs at the latter part of the run at which time the flame is about 2 in. from the outside circumference of the crib. The maximum occurred at this point regardless of the outside diameter; that is, the 12-in. diameter

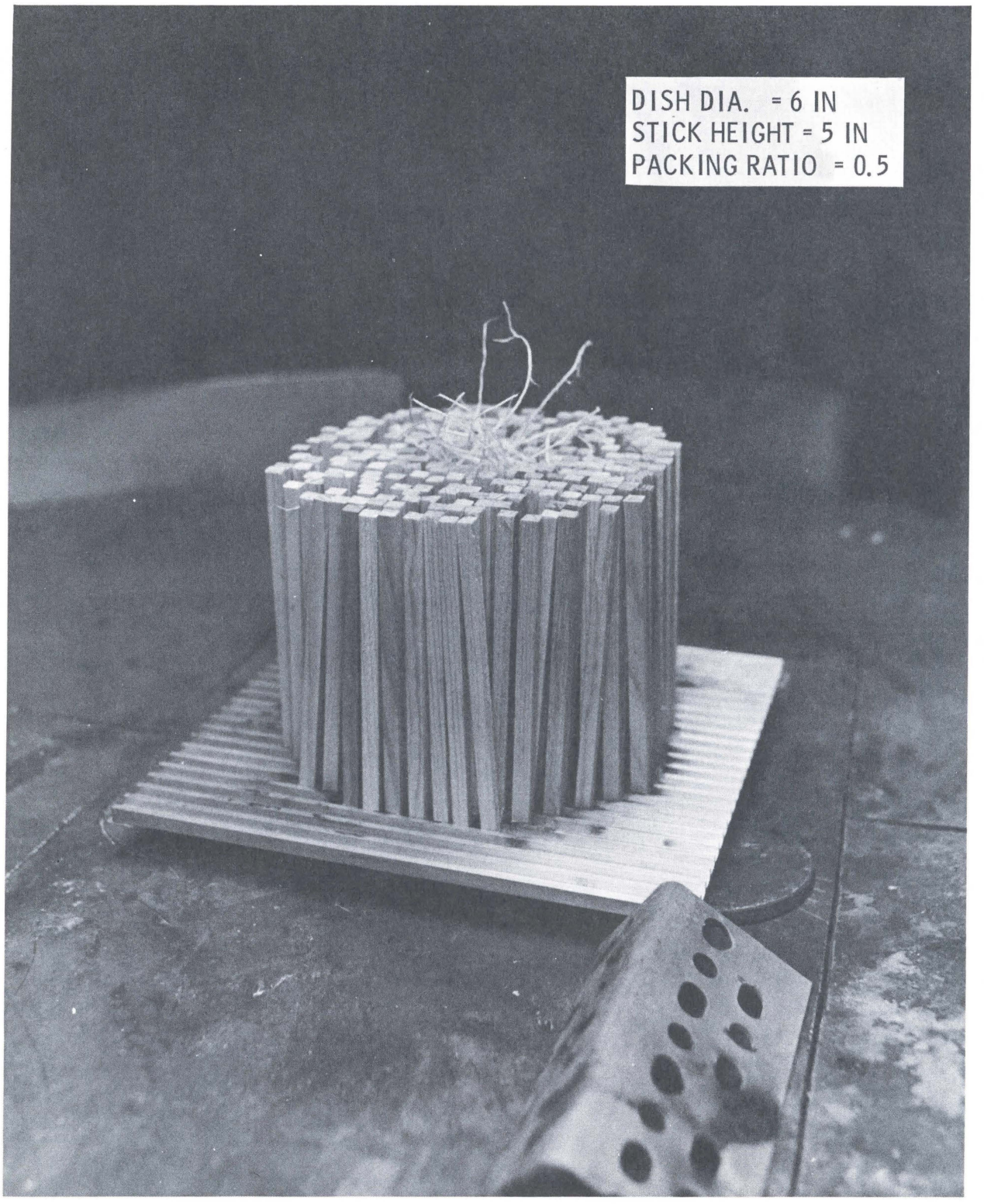


Fig. 26. Wood Crib Configuration

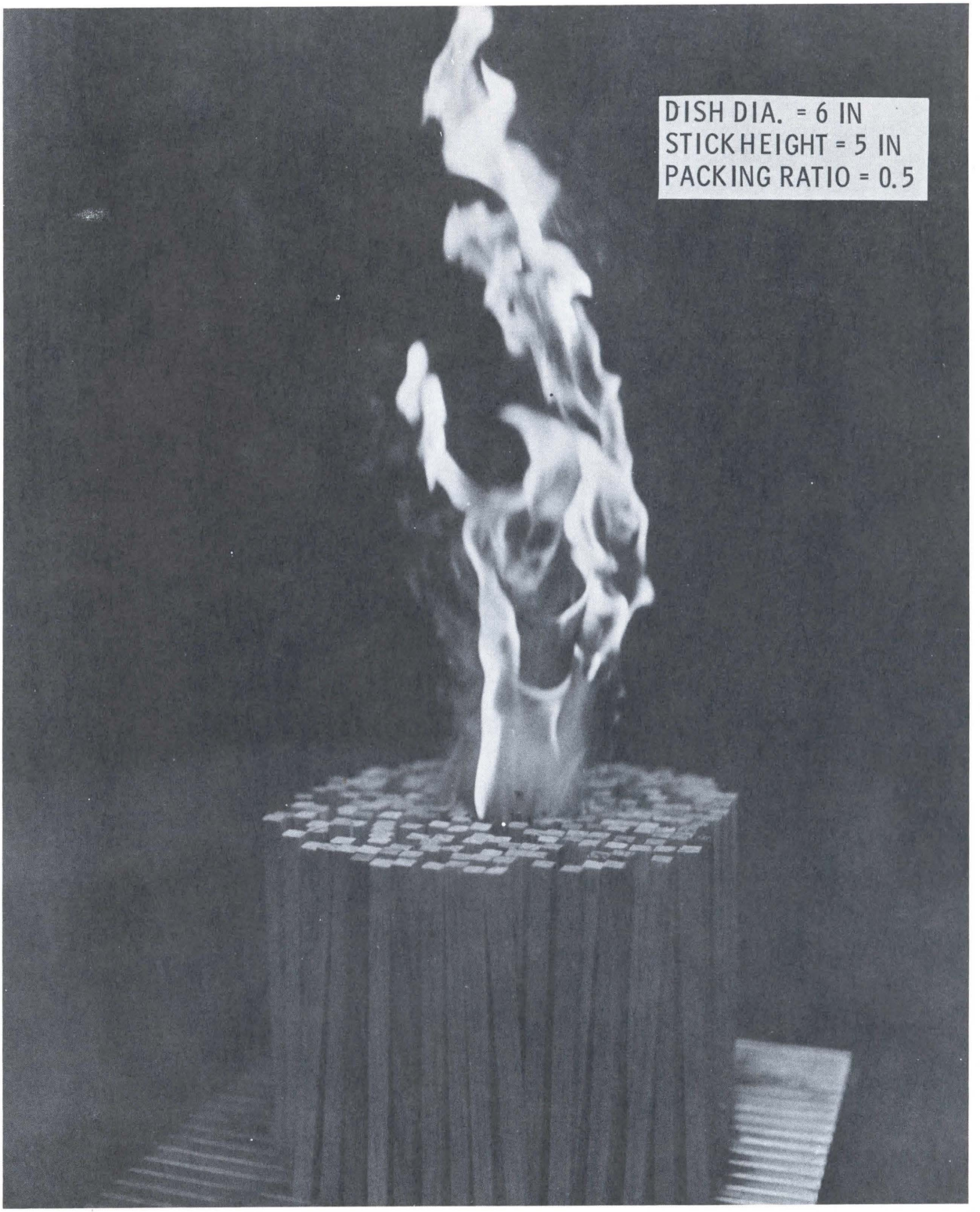


Fig. 27. Wood Crib Ignition

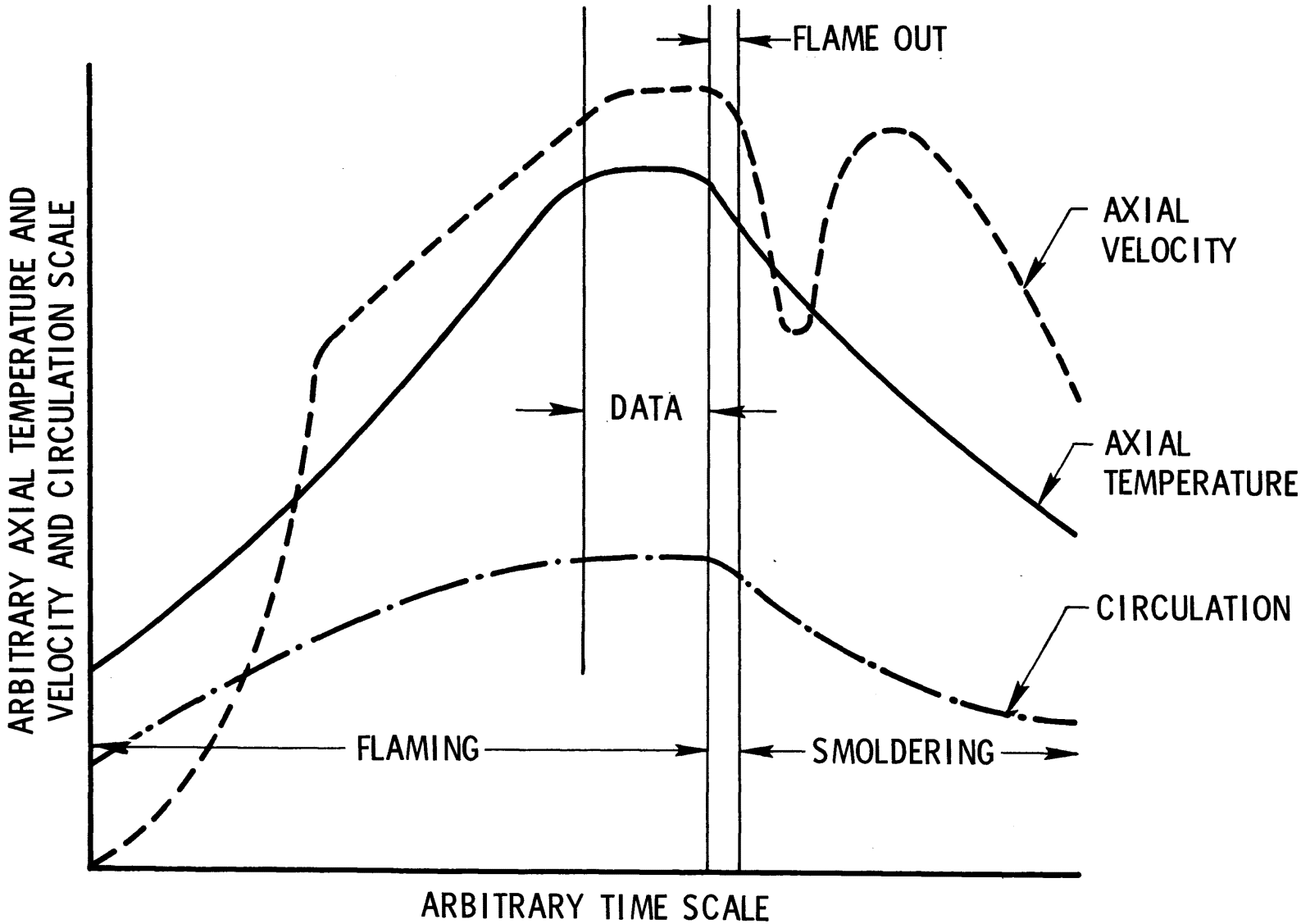


Fig. 28. Typical Time Variation of Fire Whirl Parameters

cribs reached this peak after the flame had progressed to about the 10-in. diameter point, and the 6-in. diameter cribs reached this point after the burn had progressed to about the 4-in. diameter region. Thus, there was a short period of time near the middle of the run in which all the parameters were essentially constant. This region was used for the data acquisition. A developed core for 6-in. cribs is shown in Figs. 29a-c.

Immediately after flameout, the time at which a discernable swirling flame was last visible, there occurred an interesting phenomenon. The ashes formed throughout the burn fell to the inside, presumably because of the sweeping in of the air into the combustion zone. There remained considerable glowing ash which smoldered for a long period of time. A large axial velocity resulted during this smoldering, despite the fact that the axial temperature fell off precipitously during this action. No data were accumulated during this time since it was not typical of the actual fire whirl. It should also be noted that a considerable circulation continued to exist during this period, and at the end of the smoldering region virtually all of the ash was consumed. Also, as the ash became less and less dense, there was evidence of vertical lifting of the ash due to the large axial velocity which still existed above the smoldering region.

The consequences of this very radical time variation of the various parameters throughout the run are obvious. During some of the early runs, for example, data on the velocity vector direction were recorded as a function of radial position. This required data acquisition over a long time period during which the strong variations in the parameters took place. Although some approximations were applied to attempt to correct these data and other data obtained over long time periods, there is an inherent uncertainty in these data due to the variations manifested. Thus, the "best data" are those which were obtained during the essentially constant burn time period, and this will be indicated in the discussion of the results.

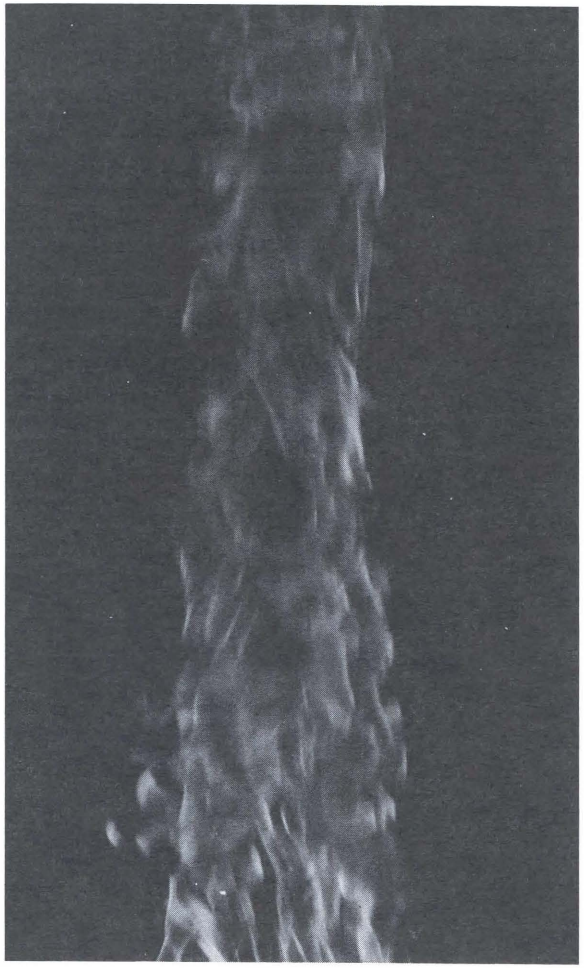

a. MID PART

b. UPPER PART

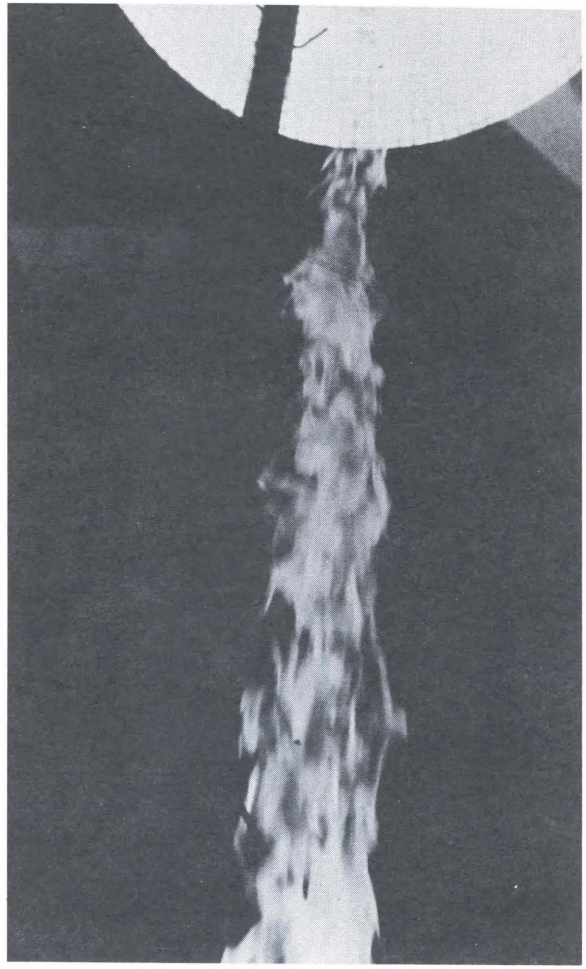

c. MID & UPPER PART

DISH DIAMETER = 6 in.
STICK HEIGHT = 5 in.
PACKING RATIO = 0.5

Fig. 29. Developed Fire Whirl Core

The majority of the measurements were made using a 6-in. diameter crib with a packing density of 0.5 and a pine stick height of 5 in. resulting in fuel loading of approximately 6 lb/ft$^2$. The principal parameter of interest was the centerline vertical velocity. Figure 30 shows the centerline variation with crib diameter for a packing density of 0.25. This curve indicates that the maximum centerline velocity was obtained using 6-in. cribs. Data at z = 45, obtained at a 0.5 packing density with 5-in. sticks, yielded a vertical velocity for the 6-in. crib of 31.6 ft/sec (mean of two runs), 34.6 ft/sec for a 9-in. crib and 35.5 ft/sec for a 12-in. crib. Vertical velocity seems to vary only slightly with crib size. Therefore, the 6-in. crib was primarily used since it is far more expeditious to build.

Figures 31 and 32 show the variation of other parameters with crib diameter, again all for a packing density of 0.25. It is interesting to note that parameters such as the circulation and maximum mass burn rate do increase with crib diameter. The increasing maximum mass burn rate is understandable since it occurs at a larger diameter of flame region. One of the objectives of the experimental setup was to obtain control of the magnitude of circulation. Varying of FASI and TBLI had relatively small effect on circulation, but increasing the crib size from 6 to 12 in. (with constant fuel loading and packing ratio) increased circulation from 3.9 to 7.3 ft$^2$/sec; i.e., almost proportionally to the diameter. Figure 32 displays an interesting result; namely, that the size of the temperature core does seem to increase with the crib diameter. However, the maximum temperature region is still associated with a very small radial region at the center of the core.

The diameter of the test rig limited the maximum diameter of the crib that could be burned without damage to the rig. A larger diameter rig would increase the circulation value of the air flow which is tangentially introduced into the rig at the outer diameter. It appears, therefore, that for larger circulation values a larger diameter test rig is required.

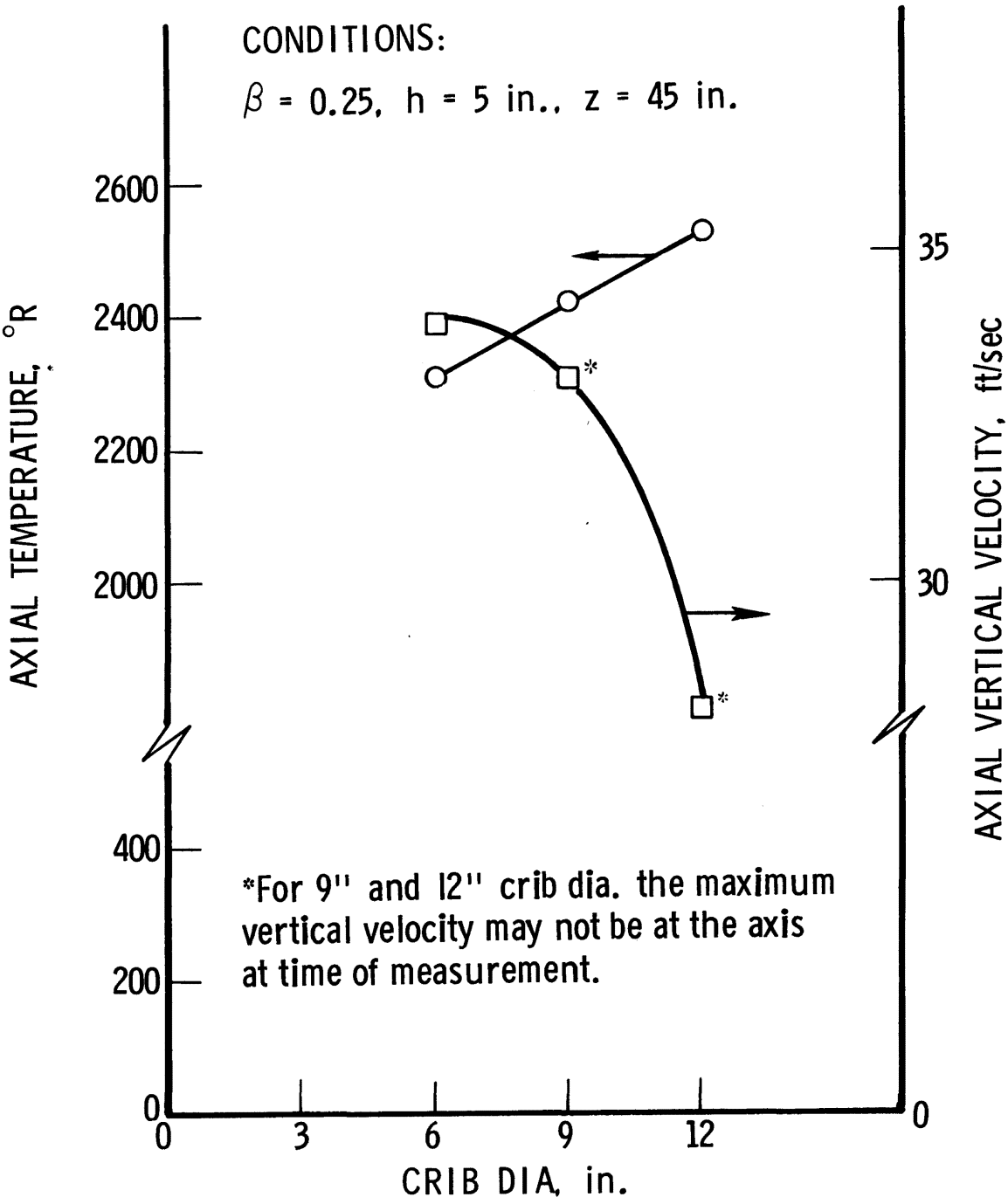


Fig. 30. Axial Temperature and Vertical Velocity Variation with Crib Diameter

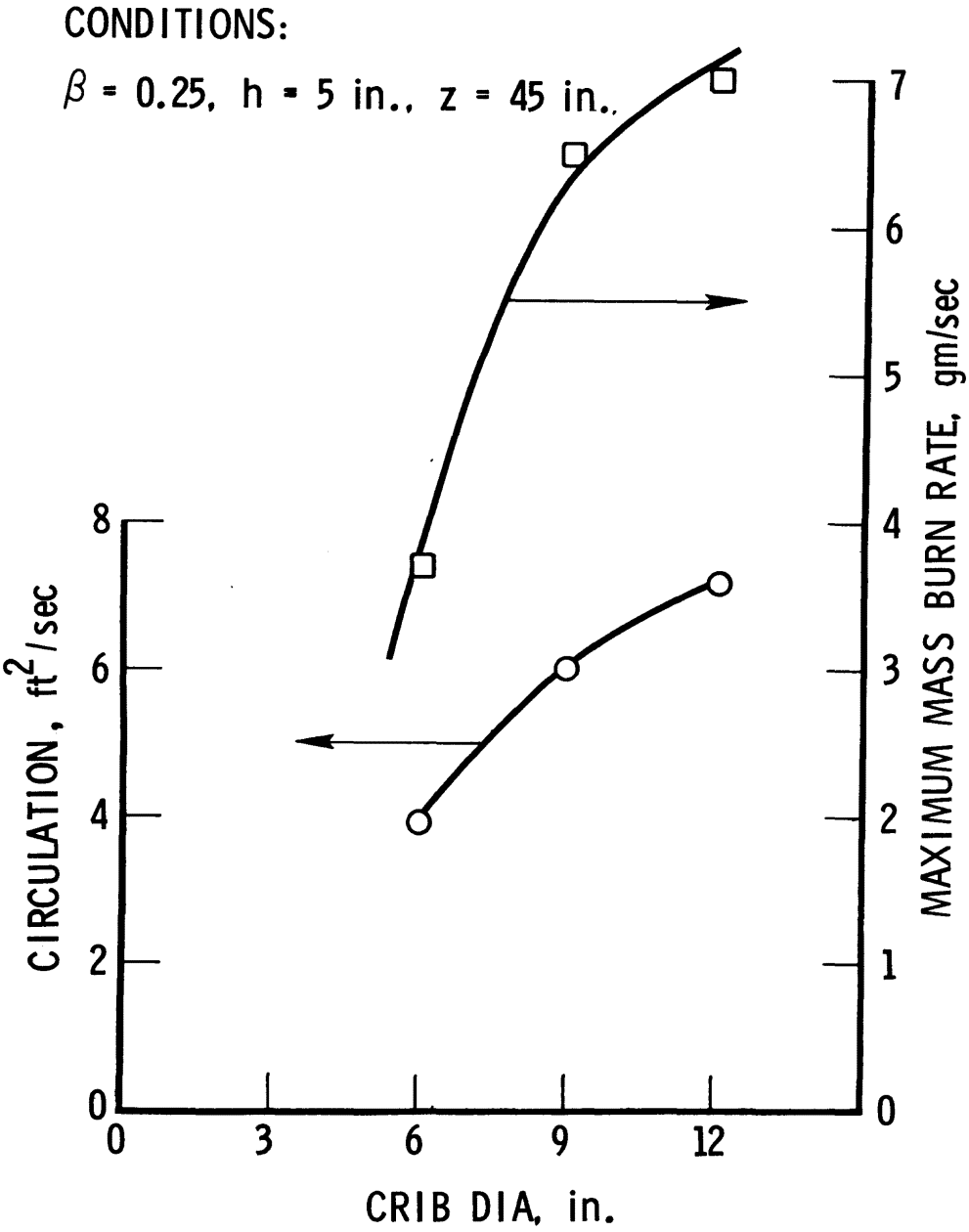


Fig. 31. Circulation and Burn Rate Variation with Crib Diameter

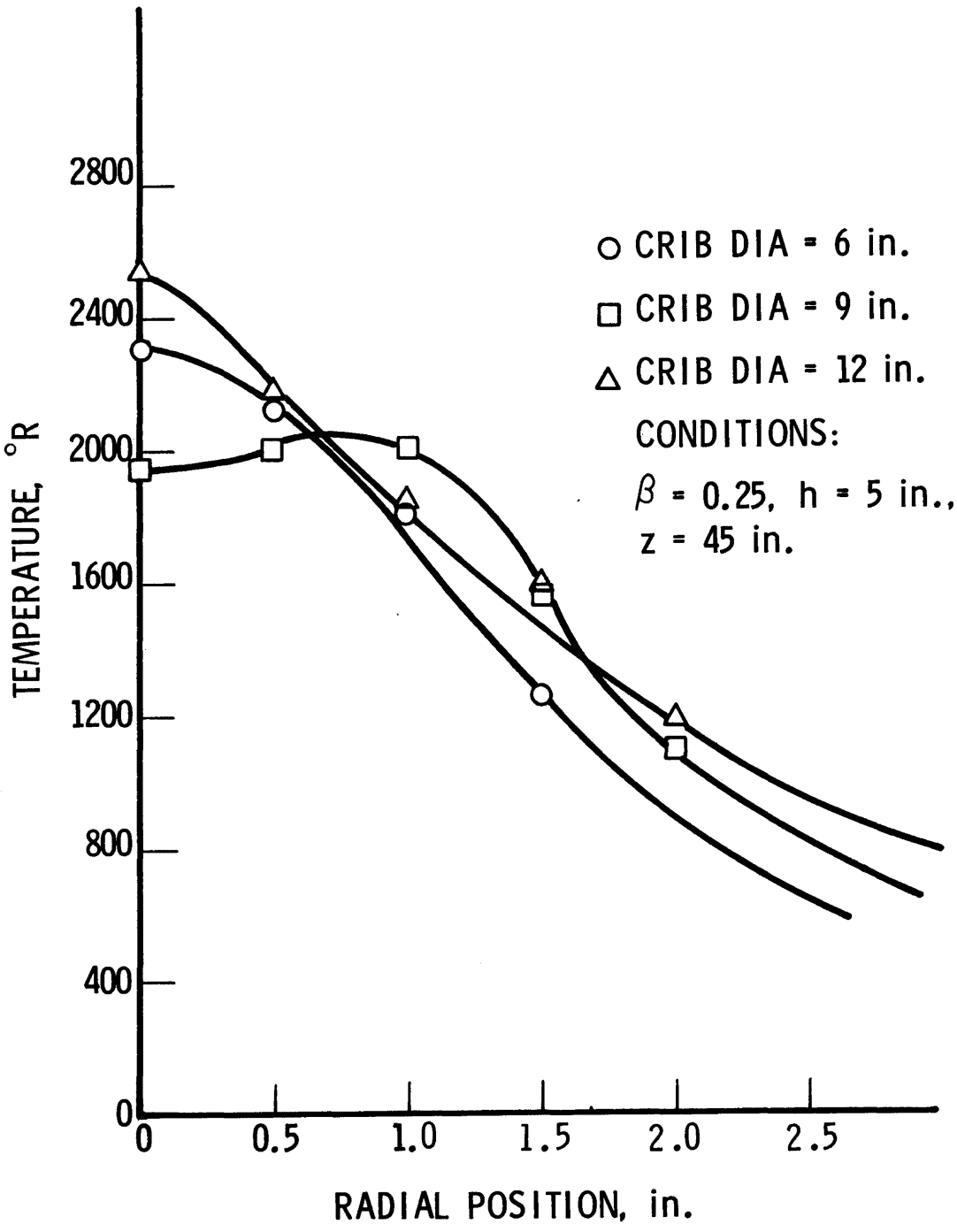


Fig. 32. Temperature Profiles as Function of Crib Diameter

Figure 33 shows the variation of the maximum mass burn rate with the height of the sticks, i.e., the wood loading, in the swirl environment. Since each of these runs was done at a constant 9-in. crib diameter, it is not surprising that the maximum burn rate occurs at the largest stick height. However, it is interesting that the rate of increase in the burn rates decreases as the stick height increases. The temperature profiles shown in Fig. 34 demonstrate that both the maximum axial temperature and the size of the core increase with wood loading.

The total velocity and vector angle were obtained for 6-in. diameter cribs using the rotating pitot tube described earlier. These results are presented in Figs. 35 and 36 (for one specific run) in terms of the velocity components determined from the data. Vertical velocity is a maximum at the centerline and drops off as expected. Note that these results show little variation with the height above the crib up to 45 in. Previous acetone results did show a maximum vertical velocity off the centerline for the lower height considered, i.e., 17 in. This was not manifested in these results under the conditions tested. The tangential velocity profiles also were as expected, being zero at the centerline and rising to a maximum at the core edge. In a previous discussion, it was indicated that these total velocity measurements had to be obtained over a time period which started before the essentially constant burn region in which the other data were obtained. Thus, there was a strong time variation in the results. In order to compensate for this, a correction was applied to the results. Typically, the velocity was measured at the centerline and at radii of 1, 2, 3 and 4 in., and then repeated for the centerline. In all runs which were used, the 3- and 4-in. and second centerline measurements were during the normal data acquisition period. However, the initial centerline, 1-in. and sometimes the 2-in., were during the rapid parameter increase period. To compensate for the changes, it was assumed that the centerline velocity increased linearly during this period and that the velocity at other radial positions increased proportionate to the increasing centerline velocity. Thus, some attempt was made to normalize the velocities to the data acquisition results.

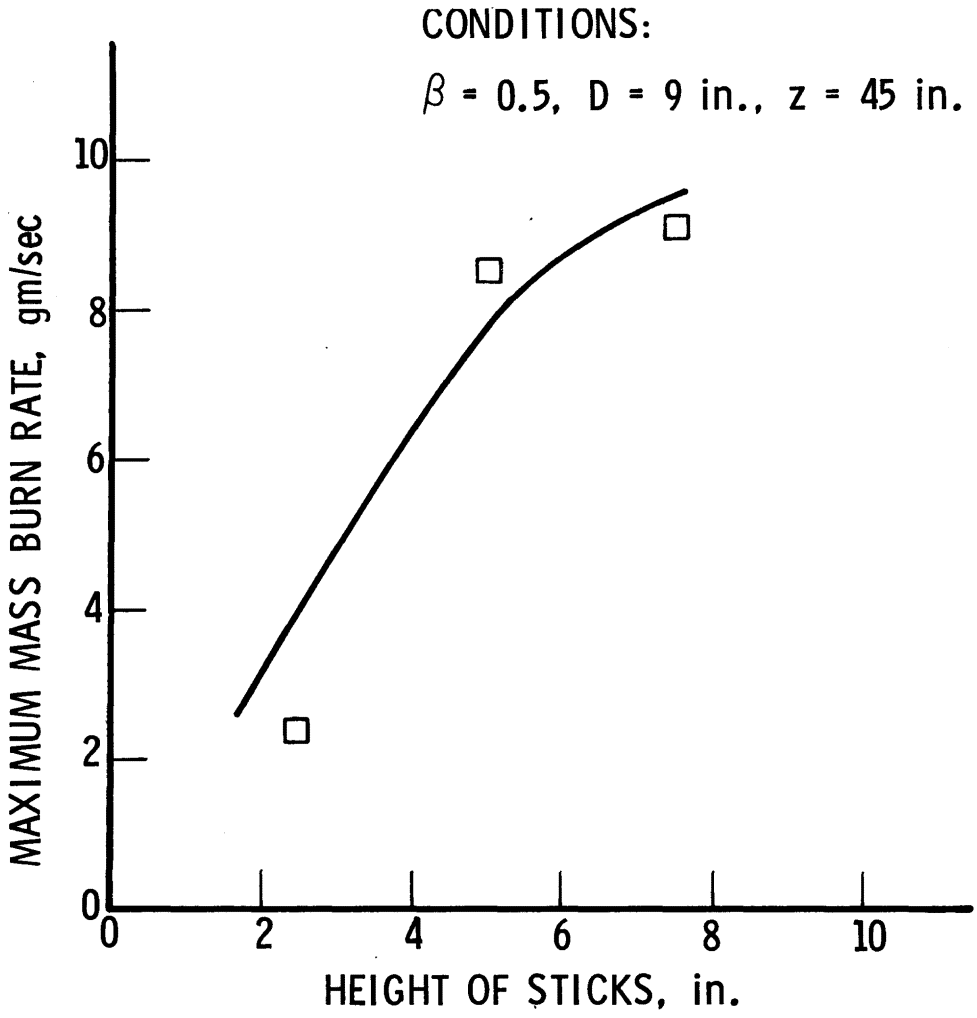


Fig. 33. Burn Rate Variation with Stick Height

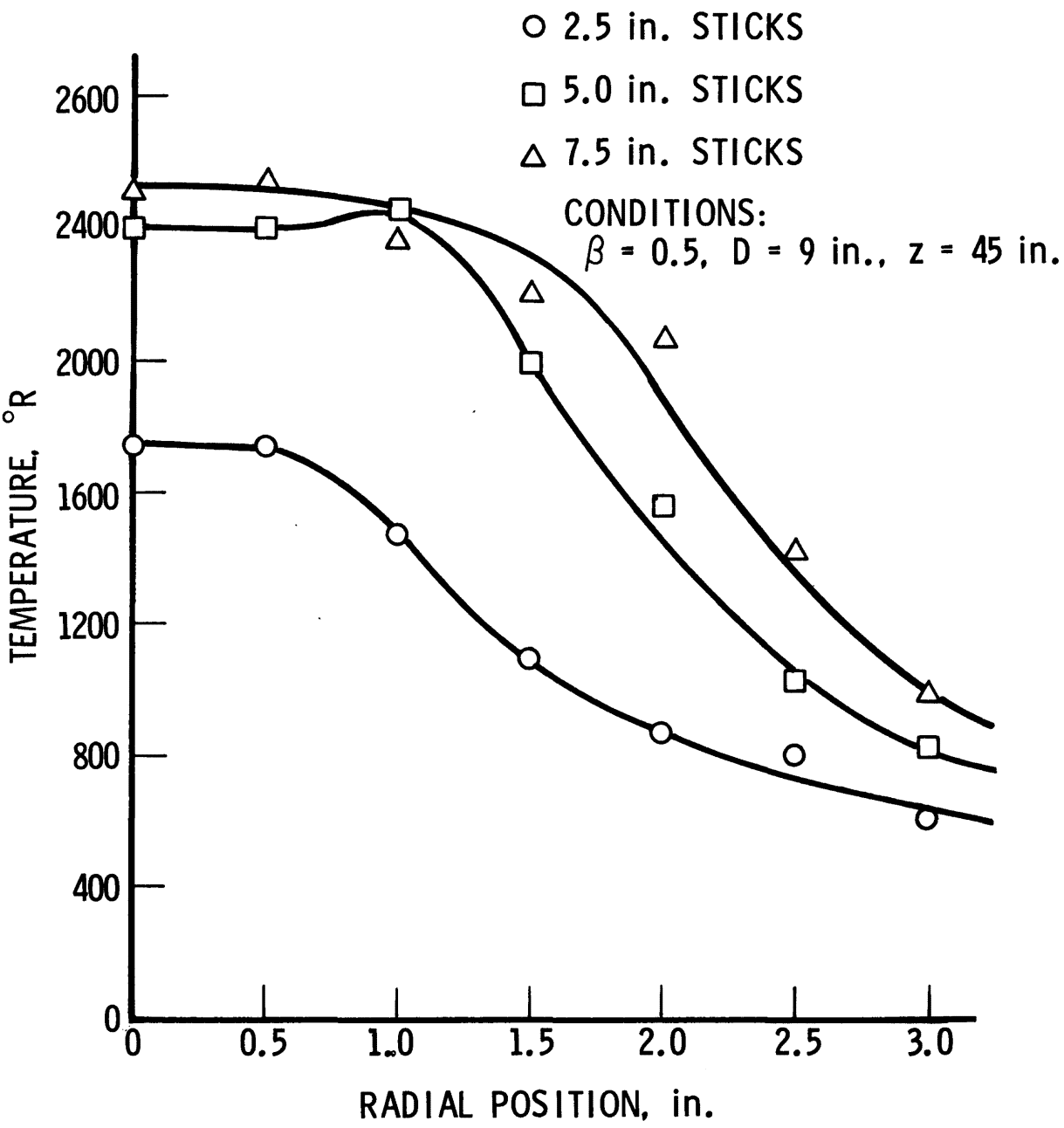


Fig. 34. Temperature Profiles as Function of Height of Burning Sticks

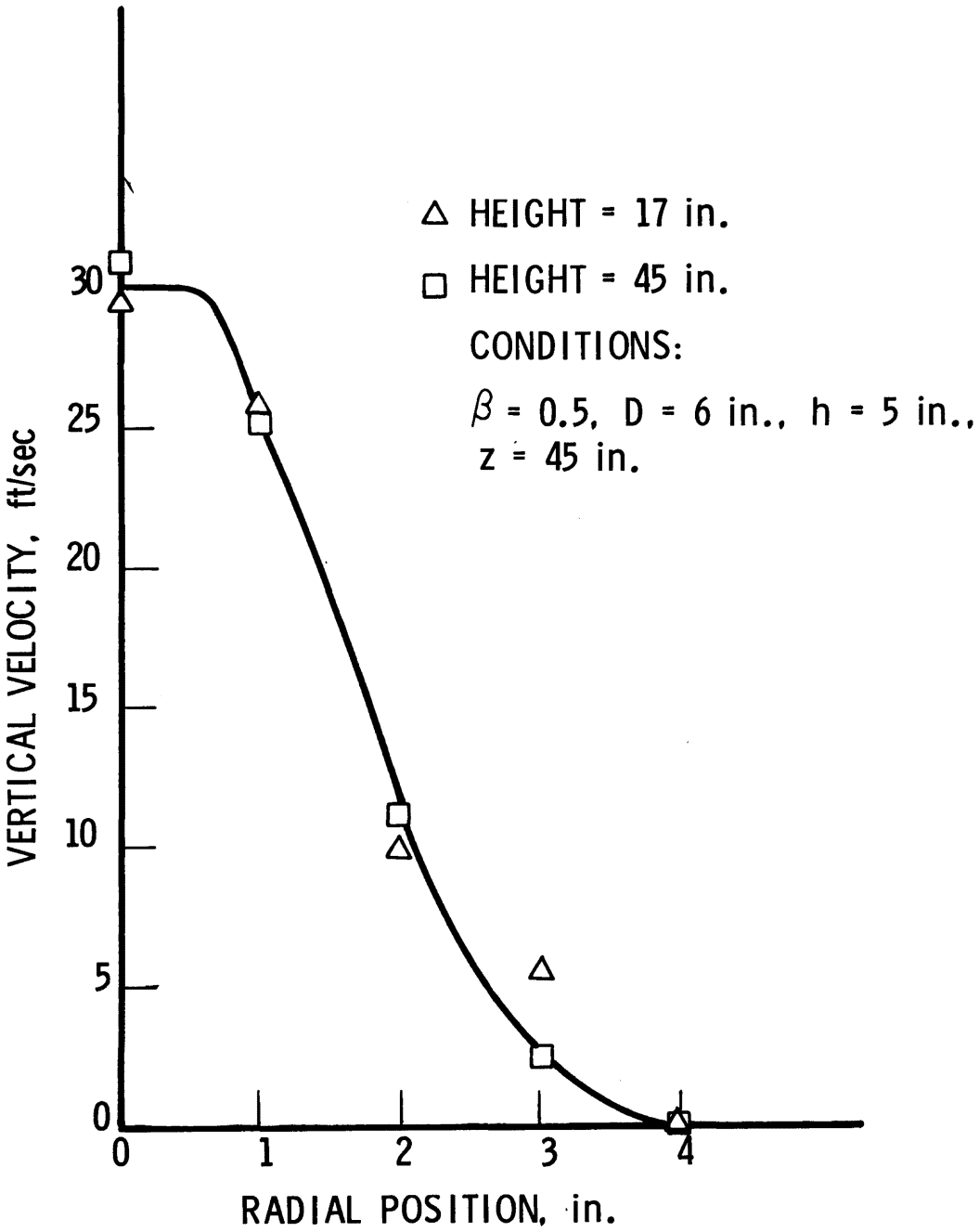


Fig. 35. Radial Distribution of Vertical Velocity

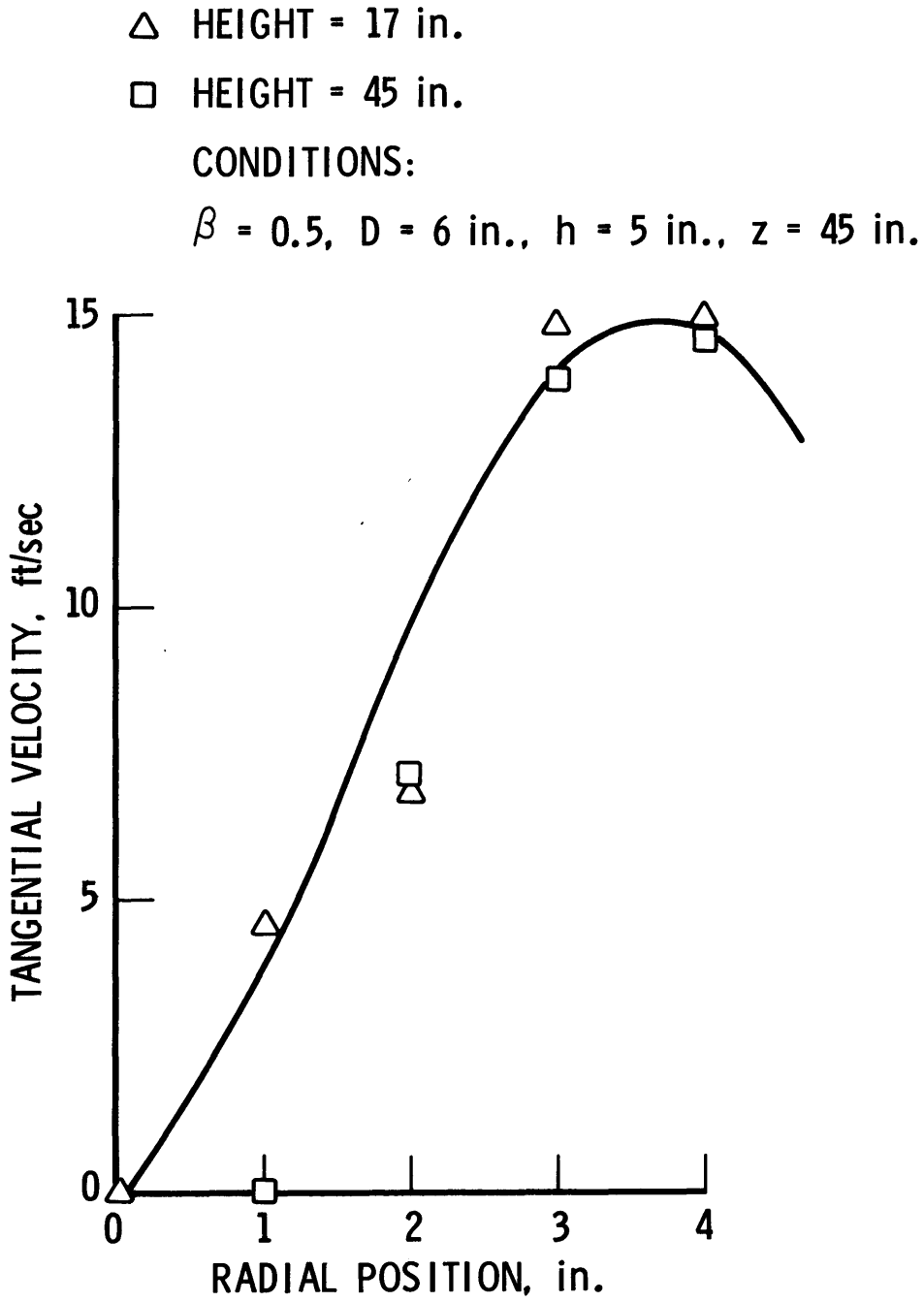


Fig. 36. Radial Distribution of Tangential Velocity

The centerline axial velocity variation with vertical position is shown in Fig. 37 (mean of two runs). The variation shown here is that the velocity is lowest at the lowest position, rises to its maximum at 45 in., and then drops off again at higher positions. The axial temperature variation with height (for a given run) is shown in Fig. 38. The temperature profiles at various heights are shown in Fig. 39 from which the core size can be estimated.

In addition to the runs using wood cribs, described previously, a series of tests was made to directly demonstrate the lifting characteristics of the swirling core. To accomplish this, pieces of wood were released into the core at prescribed positions and their trajectories photographed. Since the previous results indicated that near-maximum lifting conditions probably could be obtained using a 6-in. diameter crib, a 0.5 packing density, and 5-in. sticks, these conditions were chosen for the trajectory tests. Additionally, the maximum axial velocity appears to occur at the 45-in. position, so all of the data were obtained at that position. In all cases, the pieces of wood were balsa of density 0.25 g/cm$^3$ (16 lb/ft$^3$), having a square cross section and a length of 1/2 in. Two stick sizes were used; namely, 1/16 and 1/8 in. square. Pieces of balsa were positioned within the core on a long metal rod and then dropped off the end of the rod and the trajectories photographed. Two orientations were chosen: in (a) the length coincided with the core radius; in (b) the length was normal to the core radius and the core axis. Orientation (a) gives a maximum drag cross section in the vertical and azimuthal directions and a minimum cross section in the radial direction. Orientation (a) is the one observed by Tarifa to be most applicable to firebrand trajectories. Orientation (b) yields a maximum drag cross section in the vertical and radial directions and a minimum cross section in the circumferential direction. Thus, each orientation maximizes the lifting characteristics of the core, while orientation (a) maximizes the circumferential forces and orientation (b) minimizes the circumferential forces. The results of these tests were used for verification of the analytical model and are discussed in Section IV-D-3.

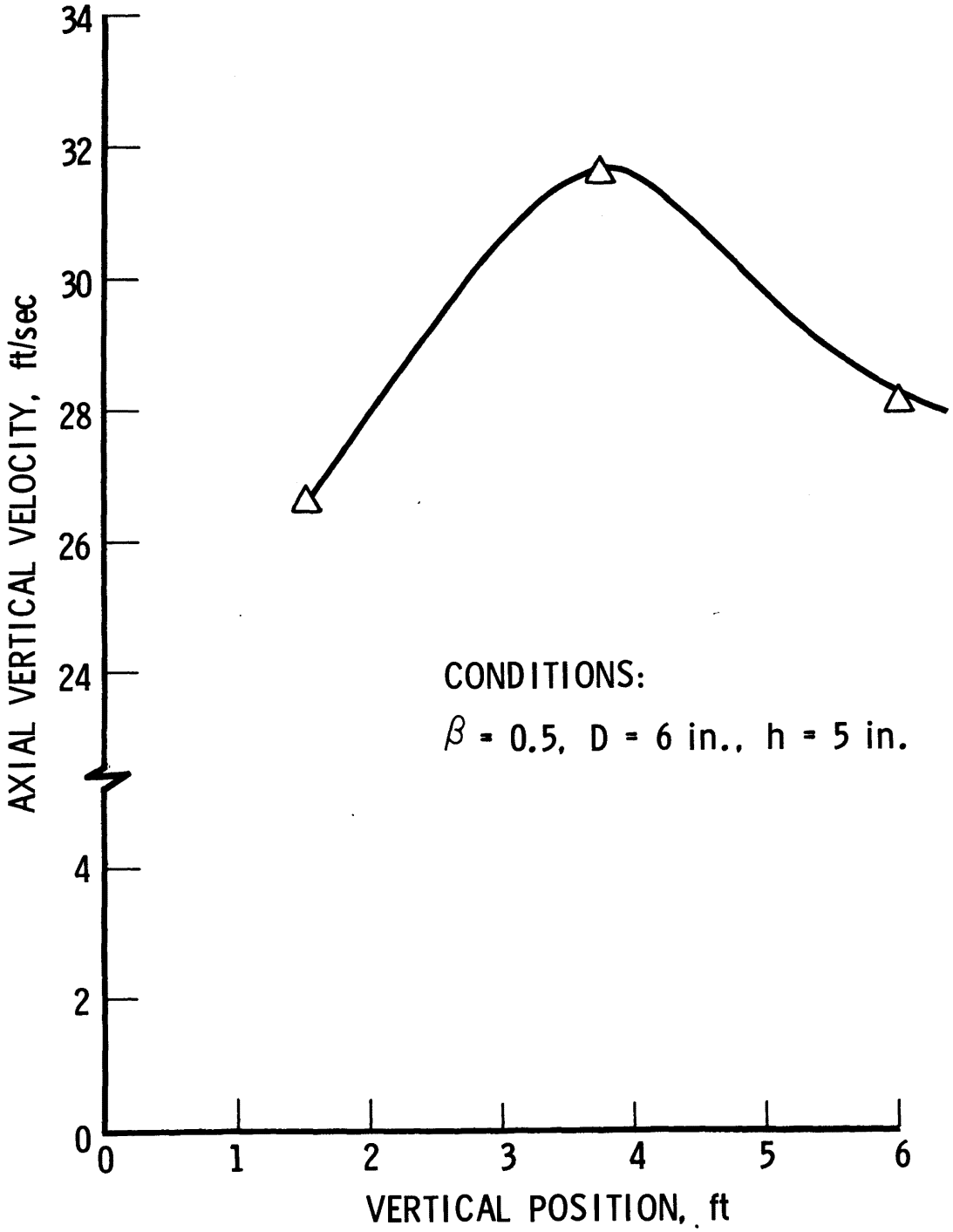


Fig. 37. Axial Velocity Variation with Height

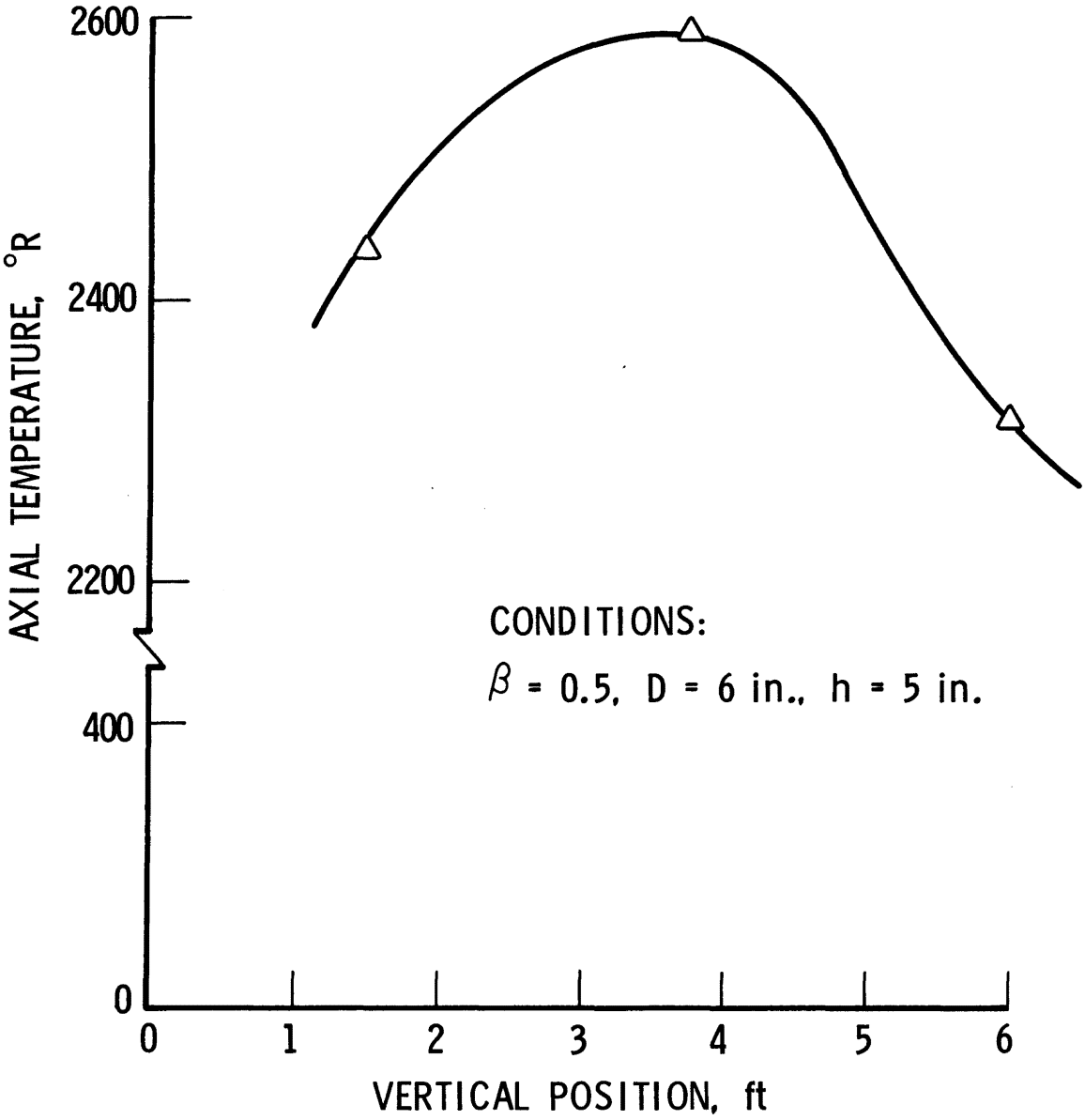


Fig. 38. Axial Temperature Variation with Height

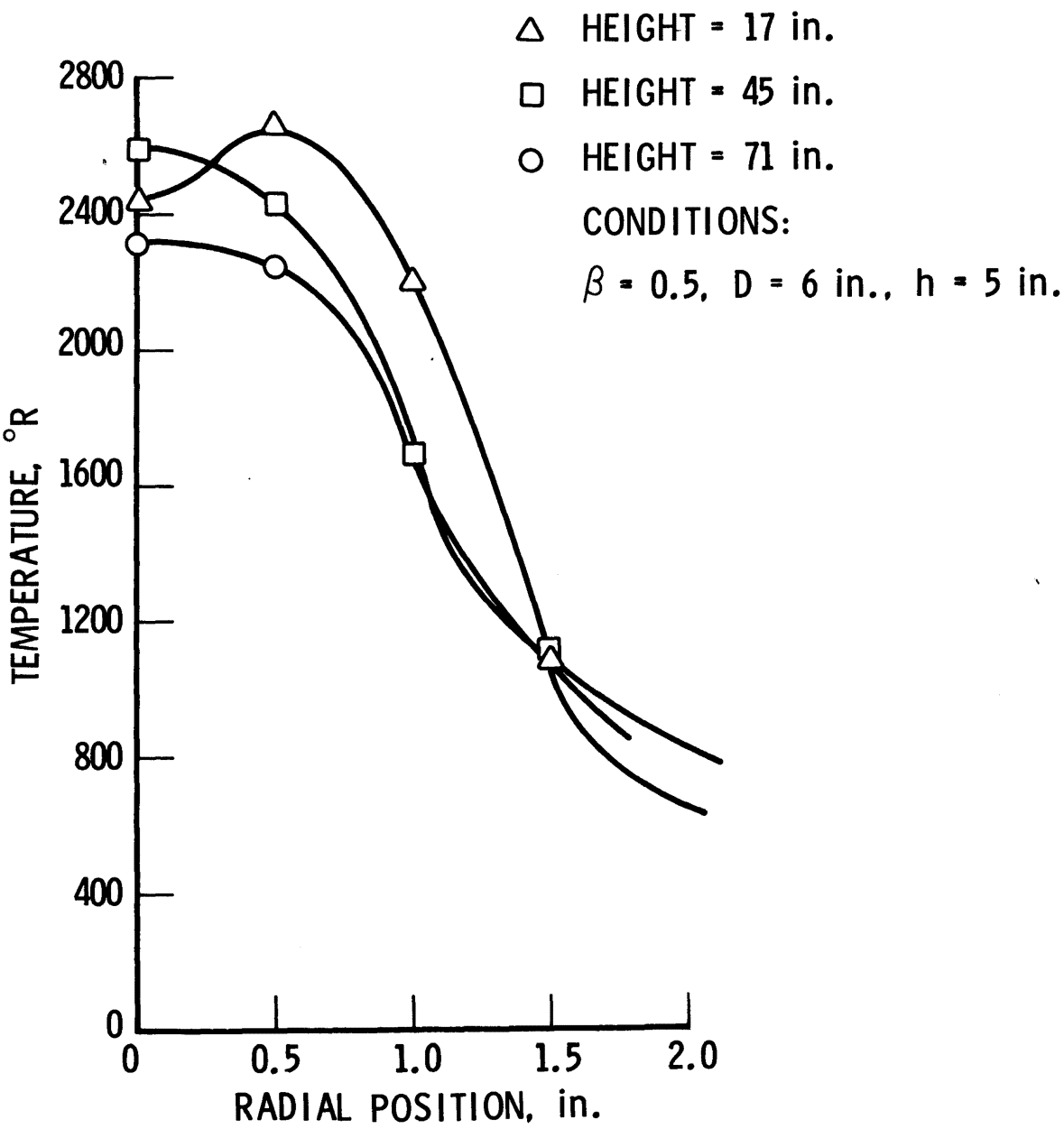


Fig. 39. Temperature Profile Variation with Vertical Height

In addition to the burn data obtained under swirling conditions, a set of runs was made in which the swirl producing components of the apparatus were removed, thus yielding essentially a no-swirl condition. The results of the no-swirl tests are shown in Table 10.

The no-swirl burn rate, similar to the rates with swirl, varied throughout the burn period, and data shown in Table 10 represent maximum rates at approximately the same phase of burning as those during which the fire whirl data were taken. The maximum burn rates observed are not in agreement with Thomas' equation[22] in which the product of bulk density times linear burn rate was constant and equal to 0.95 $lb/ft^2$-min. They are, however, in some agreement with Harmathy's results[14] which indicate that for the dense fuel configurations used in our experiments the burn rate should be proportional to the stick height. There was a considerable scatter of the data collected by Harmathy, and experimental data presented here are within this scatter.

Table 10. No-Swirl Burn Rate Data (Oven-Dry Fuel)

| Crib Diameter, in. | Stick Height, in. | Packing Ratio | Burn Rate, g/sec (max) | Burn Rate, $lb/ft^2$ (min) |
|---|---|---|---|---|
| 6 | 5.0 | 0.50 | 1.73 | 1.17 |
| 6 | 5.0 | 0.25 | 3.36 | 2.27 |
| 9 | 5.0 | 0.50 | 3.62 | 1.08 |
| 9 | 2.5 | 0.50 | 2.51 | 0.75 |

A series of no-swirl burn tests on the same type of cribs with the same fuel was also performed at the NFFL to fill data gaps and to obtain another source of data verification. Missoula burn rates were consistently below those of UCSB (shown in Table 10) by approximately 25%. This can be explained by a possible effect of radiation from the container walls, and possible effect of even a slight wind in the UCSB experiments, which were carried out in open air while the Missoula tests were done inside. The difference between the two sets of data is small when compared to Harmathy and other data scatter; the consistency of both sets of data is an indication of their correctness.

Results presented in this section were obtained in a swirling core above wood cribs. As indicated, the major uncertainty associated with these results stems from the fact that there were strong time variations of the various parameters throughout the run, and thus for only a short period of time near the end of the run could data be obtained with reasonable confidence. In order to extend the usefulness of the data, some approximations were made in order to attempt to normalize the time varying data to this more-or-less static period near the end of the run.

It is clear from observing the burns that a very critical feature is the ability for air to be drawn in through the exterior non-burning crib into the burning region. Thus, it appears that a major element is not necessarily the diameter of the crib but the thickness of the unburned crib region. It appears, therefore, that it is advisable to construct cribs which will be burned uniformly rather than in the above described manner.

It also appears that it may be more advantageous to obtain data for each of the parameters continuously rather than through a scanning mode as was often done. Thus, one clearly sees the time variations and the interactions between the parameters as a function of time. This, of course, minimizes the necessity of normalizing the data as had to be done on occasion. Finally, since the various runs showed a strong variation even under

supposedly constant conditions, a larger amount of data must be obtained at each of the conditions studied. For example, many runs were made using the 6-in. diameter crib with 5-in. sticks at a packing density of 0.5. The maximum burn rate varied from 3 to 4 g/sec. Other parameters, however, showed a much smaller variation. For example, at a height of 45 in. above the crib, the centerline temperature variation between two runs was only 4% and the axial velocity variation was less than 12%. However, it is still clear that additional data will increase the confidence in the results herein.

The large discrepancy in the mass burn rate may be somewhat attributable to the instrumentation. Since the wood cribs were supported on aluminum plates, the amount of wood burned was a smaller fraction of the total weight than in the case of the acetone. Thus, the results for the mass burn rate were dependent upon the differences between two large numbers. It is doubtful that this error is large enough to account for the large variations indicated above, but it may be a contributing factor.

Temperature data reported for wood runs were corrected for thermocouple losses. As described in Appendix A, these corrections, although required, are based on certain assumptions as to the properties of the thermocouple and, therefore, are a possible source of error. All the data presented in this section were based on the measured and subsequently corrected temperatures and the velocities computed were likewise determined from the corrected temperatures. In all cases, the temperature of the air surrounding the core was assumed to be $100^{\circ}$F. Often, the temperature profiles (because of time constraints) did not extend out to a region in which this temperature was realized. Consequently, some of the circulation velocities as reported may be somewhat smaller than the actual values due to the lower temperature assumption made. Finally, the data obtained for the velocities and temperatures in the wood runs were subject to similar noise as discussed in Appendix A and, therefore, the error possibilities due to these problems are similar.

The effect of ambient air relative humidity and temperature was negligible; this was determined from acetone tests which were more repeatable and consistent than wood crib tests. In a series of three similar test runs with acetone (repeated a number of times for different conditions), one was usually made in the morning with low air temperature and high humidity (typically 50°F, 80% relative humidity) and the other two in the afternoon when air temperature was high and humidity low (typically 70°F, 40% relative humidity). No significant variation in any of the runs was observed beyond the expected small scatter of data. This result may be expected since the change in the enthalpy of the incoming air is small in comparison with the flame enthalpy.

The wood used in the tests was oven-dried and was not exposed to ambient air until it was built into the crib and tested.

It is clear from the above presentation that the measurement of the important parameters in a fire whirl generated by a wood crib can benefit from additional work. It is clearer now how an optimum test may be designed to yield maximum information from a given run. This combined with redundancy of data acquisition should yield far better data with a higher degree of confidence. For the analytical-experimental correlation task described in Section IV-D-1, the most relevant and consistent sets of data were utilized. Sufficient data were available to obtain a meaningful correlation.

# VI. CONCLUSIONS

The rate of firebrand burning in flight can be expressed by the rate of average density change as a function of time, wind velocity and initial firebrand size. Empirical equations were developed to define the burning in flight [Eq. (5a)] and on the ground [Eq. (5)].

Fuel moisture has a marked effect on the burning process. Above moisture of 4%, the ignition time is significantly increased and the burning rate decreased markedly at 9% moisture. Also, with high fuel moisture, incomplete burning of the firebrand in wind was observed.

The effect of air relative humidity on burning of oven-dry firebrands was negligible.

Flaming time of firebrands burning in wind is relatively short and is followed by glowing combustion. Firebrands impacting at long distances from the fire front will be mostly in a glowing combustion stage, although they could burst into flame for a period of a few seconds. On the other hand, firebrands impacting near the fire front could be predominantly in a flaming stage and therefore would pose a greater fire hazard.

The experimental fire whirl generator at UCSB provided meaningful and useful fire whirl data. Even though the whirl strength is physically limited by rig diameter, the range of fire whirl strengths obtained was large enough to provide for acquisition of the most comprehensive set of fire whirl data for wood fuels yet obtained.

Utilizing the experimental data, a relatively simple and easily applicable integrated analytical fire whirl model has been developed for the prediction of the core fluid mechanical properties. The model depends on a minimum of inputs which characterize the swirl and the fuel, namely, $\Gamma$, $z_e$, $\rho_b R_o$, and d.

The fire whirl model predicts reasonable results and trends. The core vertical velocity increases with increasing $\Gamma$ and $\rho_b R_o$ and with decreasing d. The velocity decreases with increasing $z_e$ for low to moderate values of $\rho_b R_o$ and is fairly insensitive to $z_e$ for high values of $\rho_b R_o$. The core temperature increases with increasing $\Gamma$ and $\rho_b R_o$ and with decreasing $z_e$.

A firebrand trajectory model has been developed which includes the trajectory of a firebrand in a core, in an ambient swirl, and in a wind region in which the trajectory approach previously formulated is utilized. The core height $z_e$ is the most important fire whirl parameter in determining the maximum firebrand range.

The initial radial position of the firebrand is very important in determining its range, with the range increasing for initial position closer to the core centerline. Firebrands with the largest drag area to weight ratios will have the greatest range. For fire whirls with reasonably large core heights, viable bark-like firebrands can have a range of several miles in a moderate wind.

# VIII. RECOMMENDATIONS

The objective of the firebrand investigation arose from the need to provide fire managers with a scientific tool for real time prediction and statistical assessment of spot fires generated by firebrands. Past investigations performed by various research workers, as well as the work performed by the authors, covered a part of the path leading to the final objective. The following must be completed to achieve the goal of minimizing spot fire hazard and damage:

1. Formulate a probability model for near range spot fires and fire front coalescence.

2. Formulate a probability model for long range spot fires which will include a probability of fire whirl occurrence.

3. Integrate the above models into the generalized fire spread model.

4. Verify the models formulated by observations of real fires and wherever possible by measurements of some of the parameters, and update the mathematical models as necessary.

# APPENDIX A

## INSTRUMENTATION ERROR EVALUATION

During the course of this study, many changes were required in the basic apparatus. First, the top cylindrical section had to be enclosed to maintain adequate circulation. Second, the TBLI were incorporated to improve circulation. These inlets went through several designs with the final design resulting in acceptable stability and increased fuel burn rate.

Instrumentation was improved constantly, to the point of high reliability in the final arrangement. Over the entire test period, burn rate data with acetone were by far the most consistent and reliable. Early velocity measurements were inconsistent due to instrument changes and questions regarding calibration of the pressure transducers. As a result, a transducer calibration system was constructed and used to assure reliable velocity measurements.

During the early test period a great deal of variation in results was obtained. One possible cause of this variation was the difference in the ambient conditions for the various days and times of day during which tests were run. In particular, the wind speed, air temperature, and humidity could be important. With the current configuration, it appears that the wind speed effect has been minimized. Air temperature and humidity variations are not expected to produce large percentage enthalpy differences between the hot core and ambient air. Although these measurements are taken for each run and, as indicated, no consistent variation can be demonstrated, not enough data have been obtained to be certain. For example, some anomalies still exist. Three sets of preliminary tests using the noncontinuous acetone burn mode were run at different times. Boundary layer data were obtained in one afternoon, swirl air data were collected the following morning and the remaining tests were run later that day. Axial velocity data were quite similar in the first two sets of tests but increased about 30% in the

final test. This example demonstrates the advantage of the continuous burn mode compared to the shorter multiple runs in which partial data are acquired and then correlation attempted.

In all runs, fluctuations in the data were encountered due to random wandering of the core. These fluctuations showed up predominantly in the pitot tube measurements. Consequently, data were collected over a time period sufficiently long relative to the random fluctuation time. The data were then averaged in an appropriate manner over the period of measurement. For example, several techniques showed that $\Delta p$ measurements at the centerline of the core coincide with the peaks in the recorded data. Hence, the value taken for the centerline velocity was determined by averaging the peaks within the respective data period.

An error analysis was carried out to estimate potential instrumentation errors. Considering first the pressure difference measurements, the two sources of error are in the response time and magnitude. The response time of the pressure system was capable of measuring frequencies far greater than those concerned within the experiment. This was shown by pulsing the plastic connecting tubes near the pitot tubes. The recorder responded with a pulse never encountered in the fire whirl experiment. Errors in magnitude were considered negligible since the fluctuations in the data far exceeded the instrument error, which was minimized by frequent calibration.

The second measurement error considered was the weight measurement. Again, the response time was so good it made data interpretation difficult and was the reason for adding the low pass filter in the system. Also, magnitude measurements were excellent ($\pm 0.5$ gm) compared to fluctuation in the measurements ($\pm 8$ gm). As mentioned earlier, the absolute fuel weight was not of concern, but rather the slope of the weight curve. Hence, the shift in the weight curve at the beginning of a run did not introduce an error in the burn rate measurement.

The most significant error is that of the thermocouple. The thermocouple tip protrudes from a protective sheath with the wires separated from the sheath by a nonconducting insulator. One error in the indicated temperature was due to conduction through the wires from the thermocouple bead. This error was estimated to be at worst approximately 2%. Another small error was introduced by the long leads from the thermocouple to the recorder and ice bath reference. Here, the ice bath was assumed to be $32^{\circ}F$. The above errors were minor, however, compared to radiative losses as described below. The flame temperature in terms of radiative heat loss and indicated temperature is

$$T_f = \left( \frac{D_t \sigma \epsilon T_t^3}{2k_g} + 1 \right) T_t$$

where

$\sigma$ = $0.17 \times 10^{-8}$ Btu/hr $ft^2$-$^{\circ}R^4$ = Boltzmann constant

$\epsilon$ = 0.7 = tip emissivity

$k_g$ = 0.047 Btu/hr-ft-$^{\circ}R$ = gas thermal conductivity

$D_t$ = $8.33 \times 10^{-4}$ ft = tip diameter

$T_t$ = indicated thermocouple temperature ($^{\circ}R$)

$T_f$ = actual flame temperature ($^{\circ}R$)

At the highest measured temperature ($2200^{\circ}R$), the error is estimated to be 11.2% due to radiation losses. Figure A-1 shows the actual flame temperature estimated for the given indicated thermocouple temperature. As a result, the temperatures given in the previous figures have been corrected using Fig. A-1, and the corrected temperatures were used in determining the core velocities.

The experimental results presented are generally in good agreement with the analytical model predictions. Specifically, the axial velocity increases with circulation as predicted. The model assumed a velocity

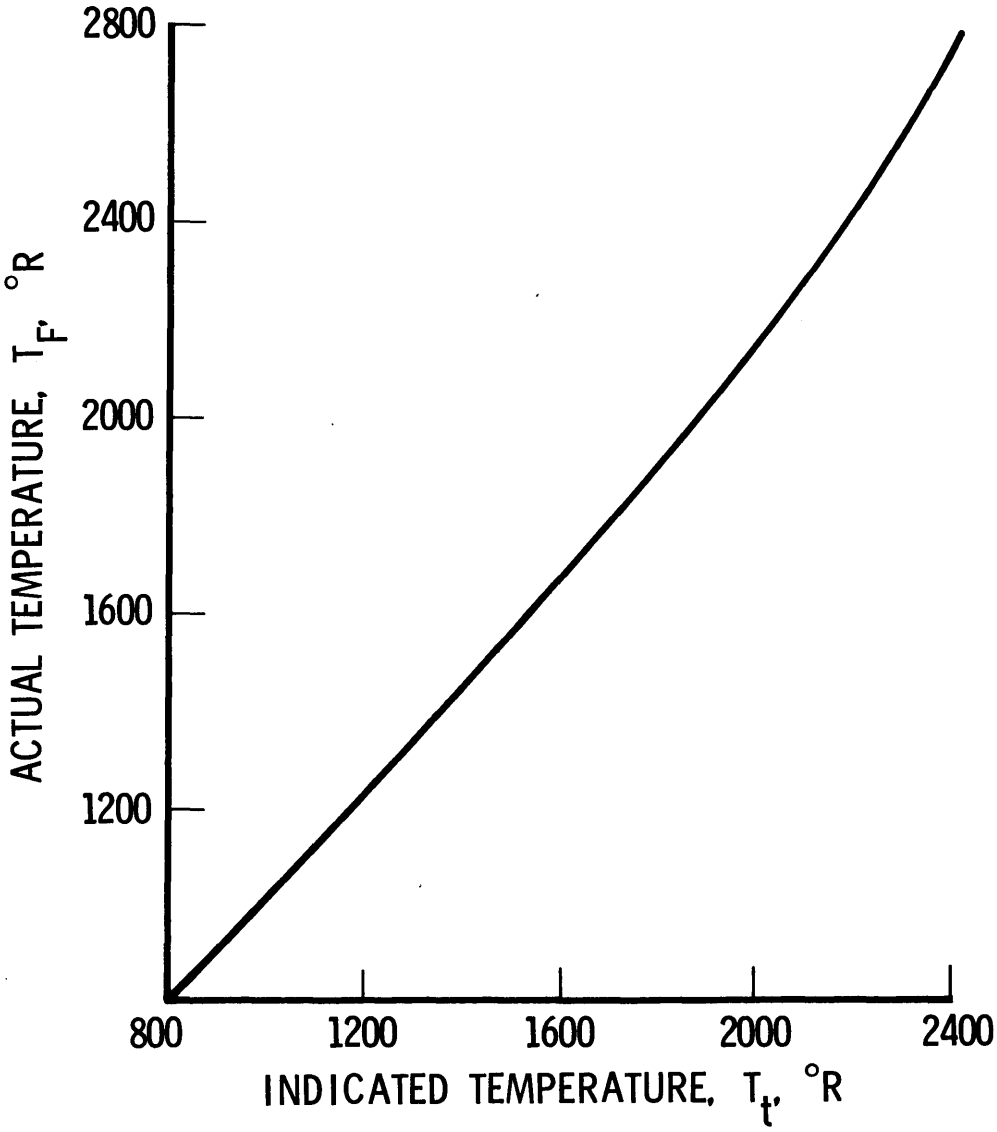


Fig. A-1. True Gas Temperature Compared to Measured Temperature Using Thermocouple

averaged over the core radius. The model prediction of $a_o$ was reasonable. Temperature correlation was good when the correction indicated above was considered. Here again, a radially averaged core temperature is assumed by the model. The measured burn rate ratio did increase with circulation as predicted and numerical agreement was good. This applies to all data shown with the exception of those with different acetone dish sizes. Such data will have temperature correction of approximately $\pm 10\%$ of the measured values.

# APPENDIX B

## ACETONE FIRE WHIRLS

For the first sequence of tests acetone was used for the fuel to generate fire whirls. For these tests the fuel was placed in a glass dish on the weighing system and, as indicated previously, a fuel reservoir could be used to operate the burning on a continuous basis. For these particular tests, three independent parameters could be varied. These were the amount of forced air introduced tangentially (FASI), the amount of air introduced tangentially in the boundary layer (TBLI), and the gap size above the floor for boundary air to be drawn in. Thus, the acetone tests were used primarily to give a detailed description of a typical fire whirl which could be generated in the apparatus used for these experiments.

A typical run procedure takes two forms depending upon the method of fuel feed. In either case, the appropriate induced air flow is provided and allowed to run sufficiently long to establish a steady-state vortex without a burning column. At this condition, the fuel is added in one of two manners. Either a prescribed amount of fuel (typically 100 g) is poured into the dish, or alternatively the fuel is allowed to flow from the fuel reservoir into the dish to a prescribed level (typically 75 g). The fuel is then ignited. In the first method, the fuel weight is recorded through the entire run. In the second method, the liquid level is held constant by monitoring the weight and adjusting the fuel flow rate to the dish accordingly to maintain the constant weight. Once a steady core is established, appropriate instrumentation is started. For the limited fuel mode, a typical acetone run is of the order of 2 to 3 min in duration.

The advantage of the continuous burn method described above over burning a given amount of fuel is that the duration of steady-state burn time is obviously unlimited, but burn rate measurements cannot be made. Consequently, most of the data presented were acquired by burning a prescribed amount of fuel.

The majority of tests were performed using a 6-in. glass dish. However, some tests were performed in order to evaluate the effect on core parameters of the dish size. To demonstrate these effects, fuel dish sizes of 6-, 8-, and 10-in. diameters were used. These dishes differed from the basic glass dish used in the bulk of the tests in that they were made out of ceramic material. Additionally, the sides of these dishes were sloped rather than vertical as was the glass dish used in the other tests. Basic measurements were taken of the temperature profiles, tangential velocity profiles, and axial velocity for different heights. These data are shown in Figs. B-1 through B-4. The temperature profiles measurements confirmed visual observations of increasing core radius with increasing dish radius, particularly at increasing heights, where the effect became substantial. Additionally, these temperature profiles demonstrate many of the same features that will be seen later and discussed in more detail.

The axial velocity profiles indicated virtually no effect of dish diameter at the middle measurement point of 45 in. However, there was a surprising dip for the 8-in. diameter dish at the other test heights. A reasonable explanation for this phenomenon cannot be seen at this time. The tangential velocity profiles are shown in terms of the circulation. Only those data at 45 in. and 71 in. are shown, since those at 17 in. were very erratic and showed no correlatible trends. The figures show that there is a slight increase in circulation with increasing dish size. However, the total effect is minimal, particularly at the 45-in. measurement region.

As indicated above, the majority of the tests were run using a 6-in. diameter glass dish. The effect of dish size and core parameters is indicated above to provide quantitative descriptions and to indicate general trends to be expected for tests run with other than the 6-in. diameter dishes. The tests described hereafter were all made with the 6-in. dish to establish the variation of the various parameters within the core for a fixed dish size.

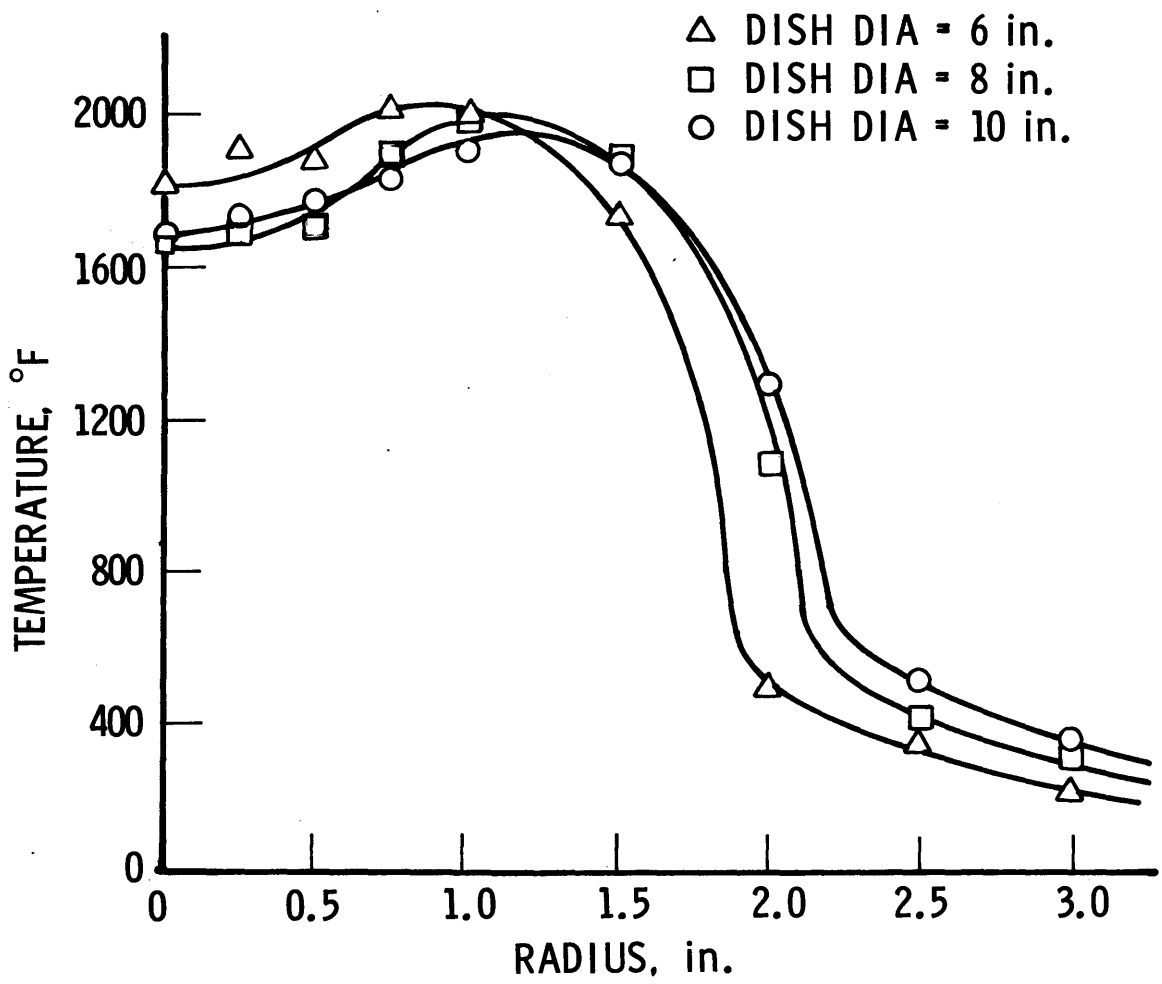


Fig. B-1. Temperature Profiles at Height of 17 in. for Various Dish Diameters

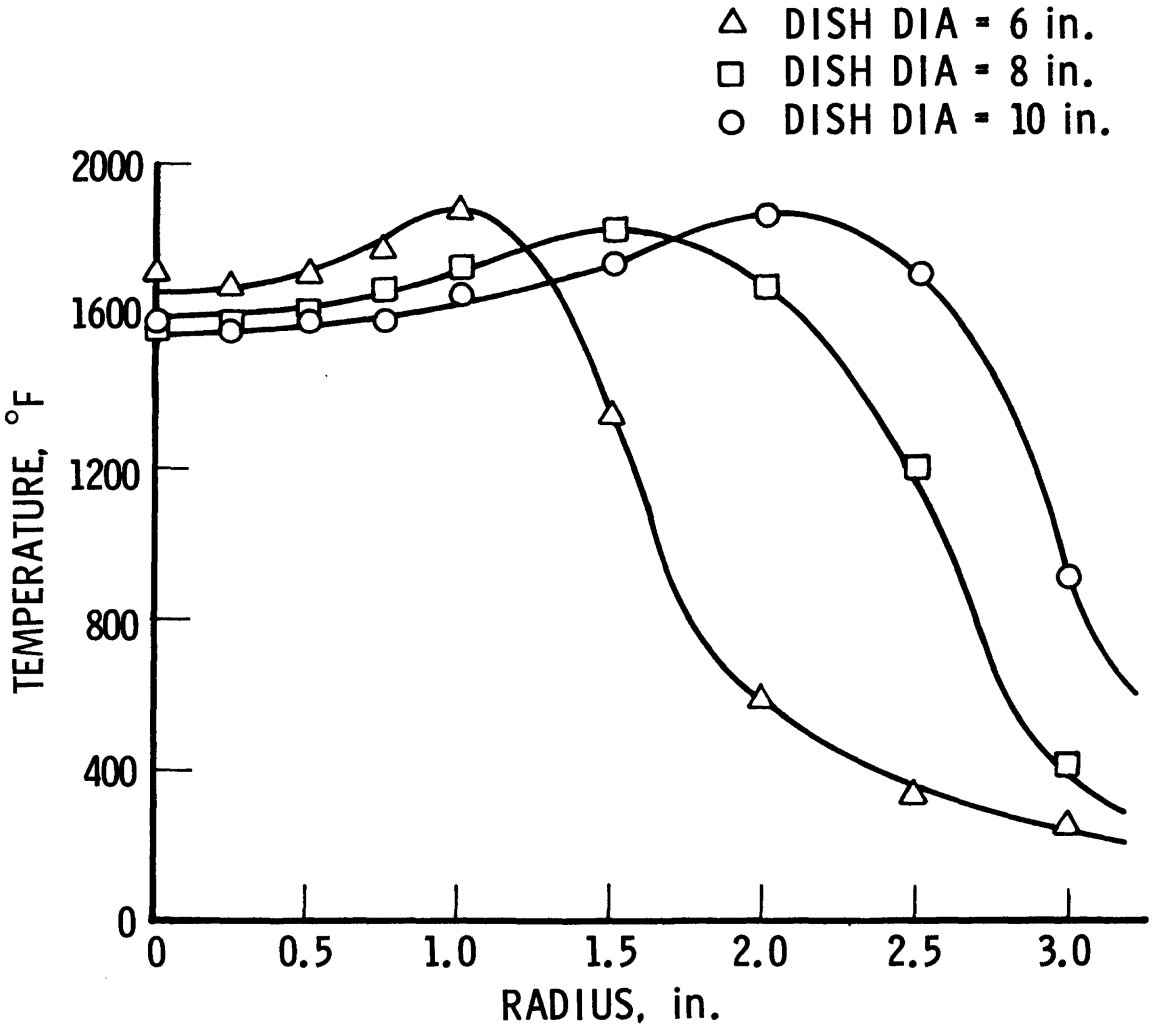


Fig. B-2. Temperature Profiles at Height of 45 in. for Various Dish Diameters

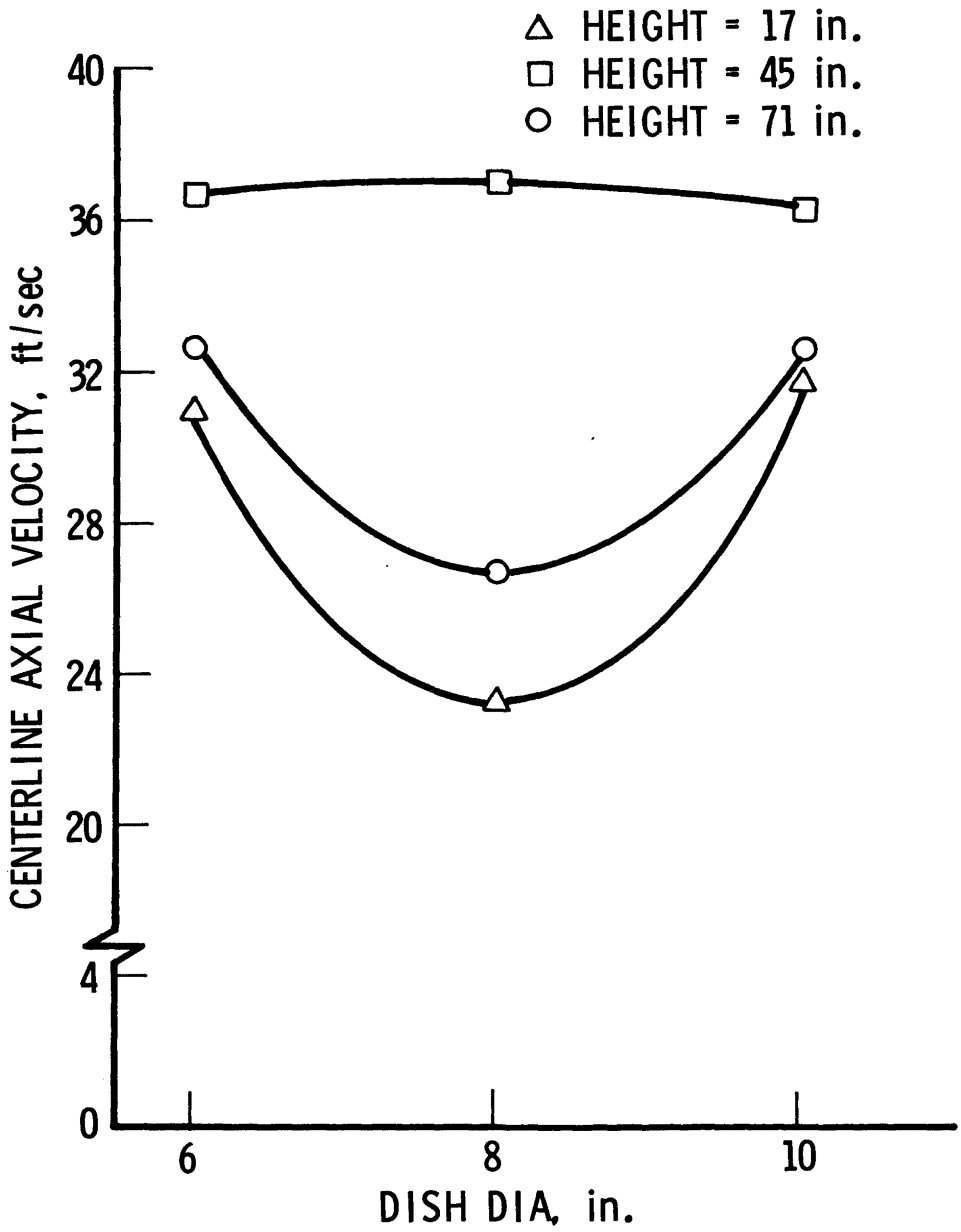


Fig. B-3. Axial Velocity Variation with Dish Diameter at Various Heights

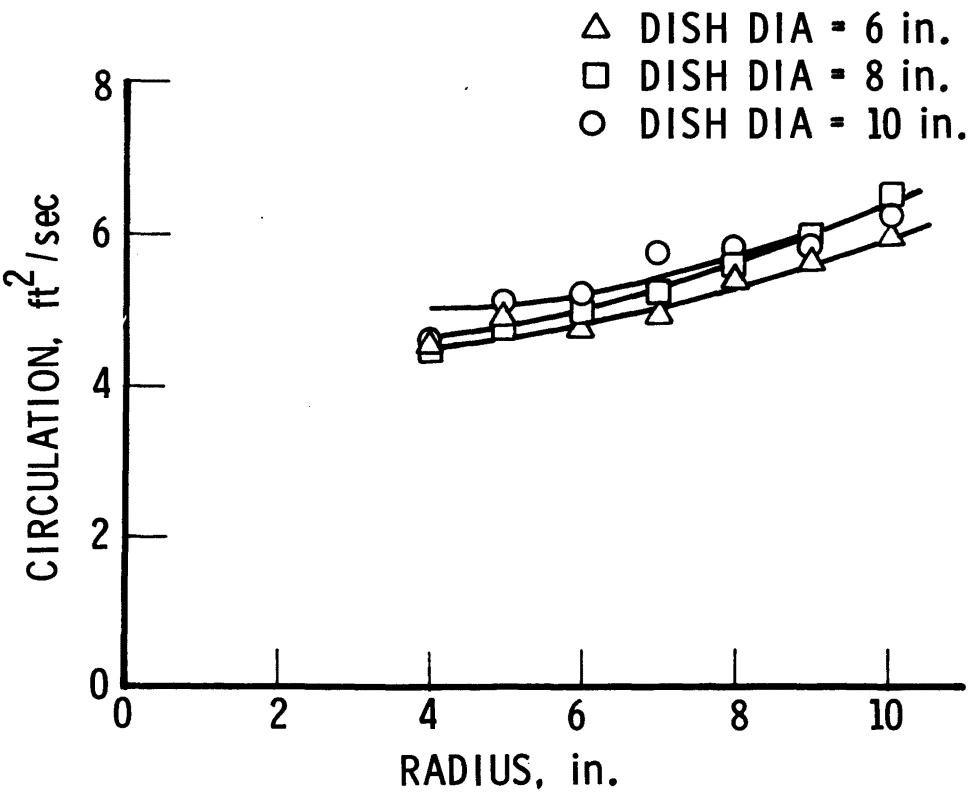


Fig. B-4. Circulation Profiles at Height of 45 in. for Various Dish Diameters

Preliminary data were required in order to optimize the test rig configuration to obtain maximum axial velocity. Measurements taken were axial velocity, temperature at r = 0.5 in., tangential velocity at r = 5 in. and the burn rate. These data were obtained at a height of 45 in. and tangential velocity was measured at all three data heights. First, the effect of varying the effective boundary layer height was observed. Three effective boundary layer heights (0.45 in., 0.9 in. and 1.35 in.) were studied. Results of the boundary layer height on burn rate with and without swirl (no FASI or TBLI) are given in Fig. B-5. It is clear that for gap heights of more than 1/2 in. there is a significant increase in the burn rate due to swirl. The centerline axial velocity and temperature appeared to be highest with the 0.9-in. effective boundary layer gap. The effect on circulation (at r = 5 in.) was minimal with a slight decrease in most cases. Since it was desired to obtain the highest axial velocity, the boundary layer gap in further tests was set at 0.9 in.

The last of the preliminary tests provided data on the variation of core parameters with varying flow through the FASI (circulating air) at the established TBLI gap. The resultant burn rate ratios are given in Fig. B-6. The burn rate and axial centerline velocity (not shown) indicate a peak near 0.14 lb/sec air flow (corresponding to tangential air velocity of approximately 20 ft/sec). As earlier, the criterion for optimization was axial velocity, and swirl air was set at 0.14 lb/sec flow.

At this point, optimization was complete with regard to axial velocity for the given dish size of 6 in. diameter. The test data obtained (three tests at each condition) included circulation profiles in the swirl region and core temperature and velocity profiles (both magnitude and direction) at the three indicated heights.

The average results of these tests are presented in Figs. B-7 through B-12. The first two figures show the variation of the tangential velocity and circulation with both radius and height. There is little variation with height.

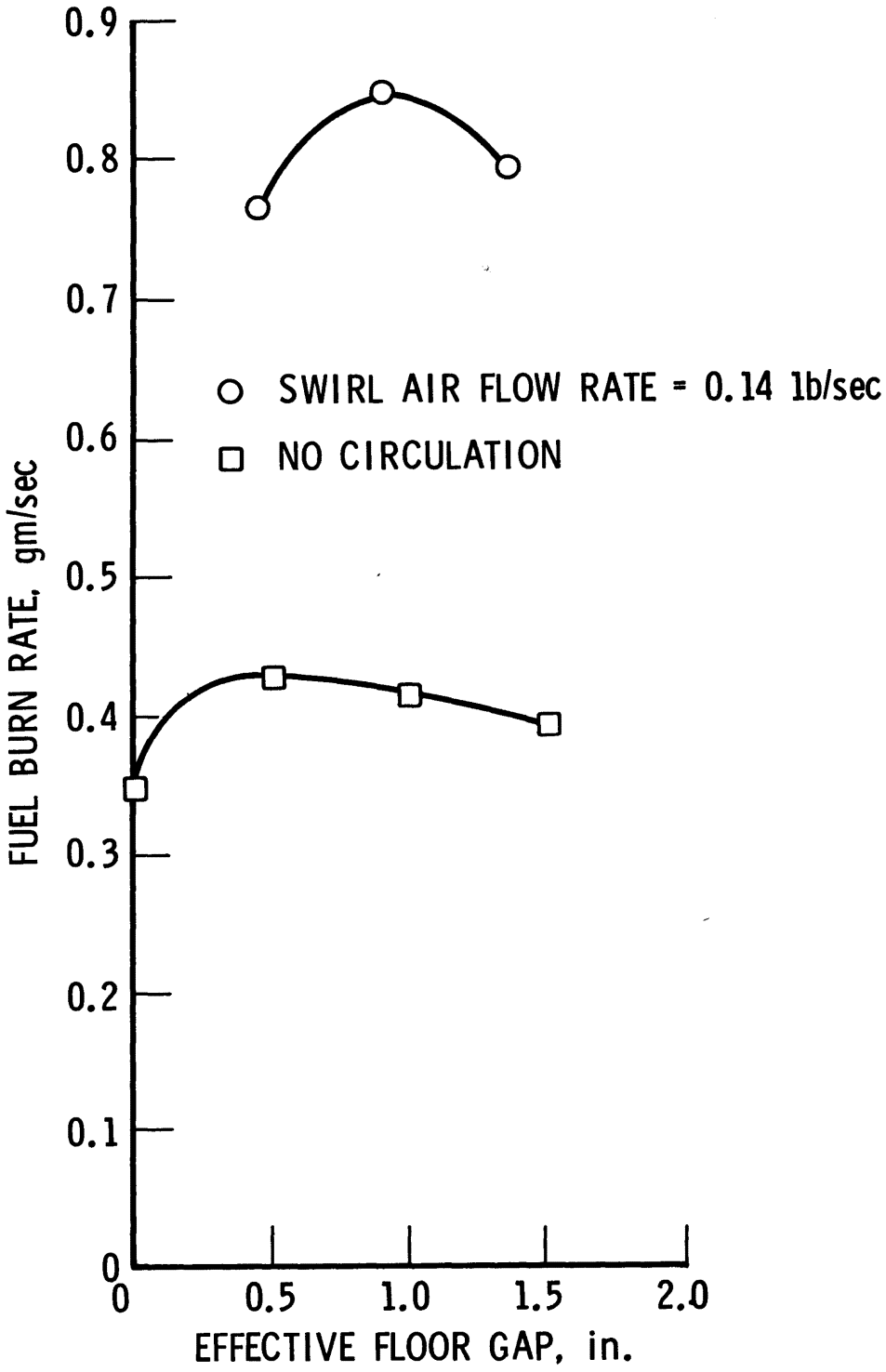


Fig. B-5. Acetone Burn Rate Variation with Boundary Layer Gap

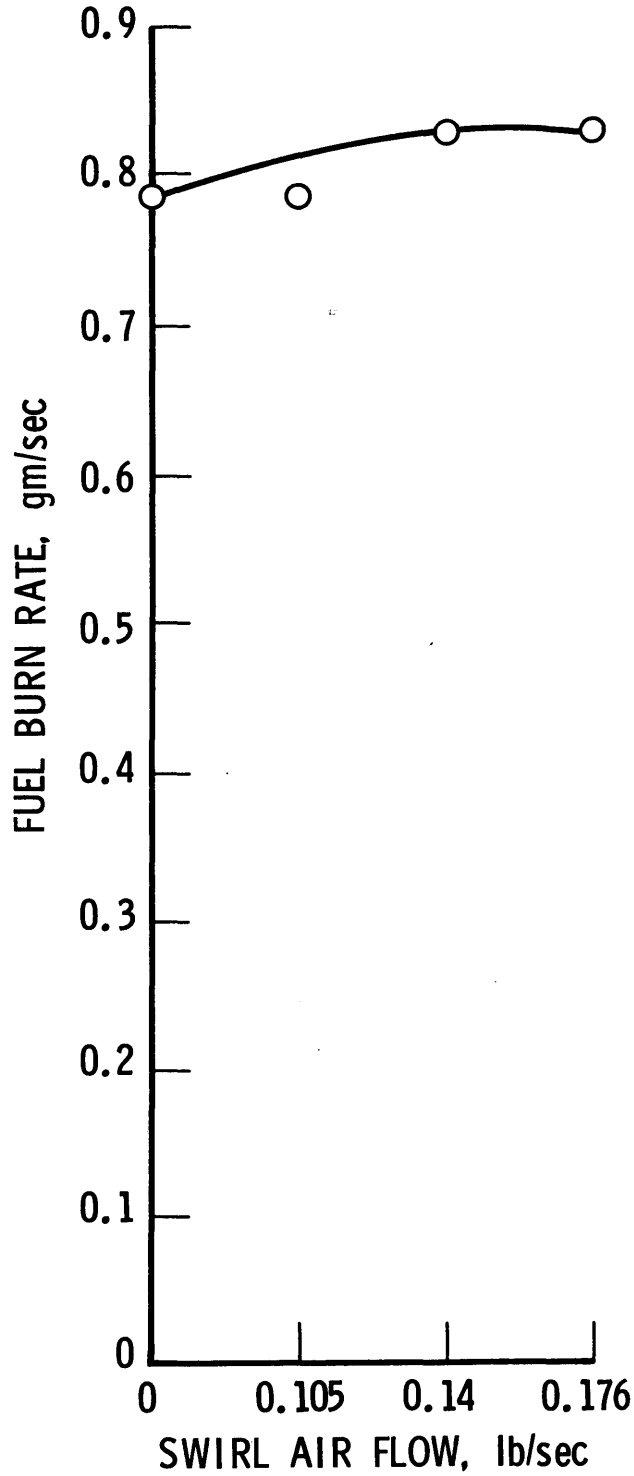


Fig. B-6. Acetone Burn Rate Variation with Swirl Air Flow

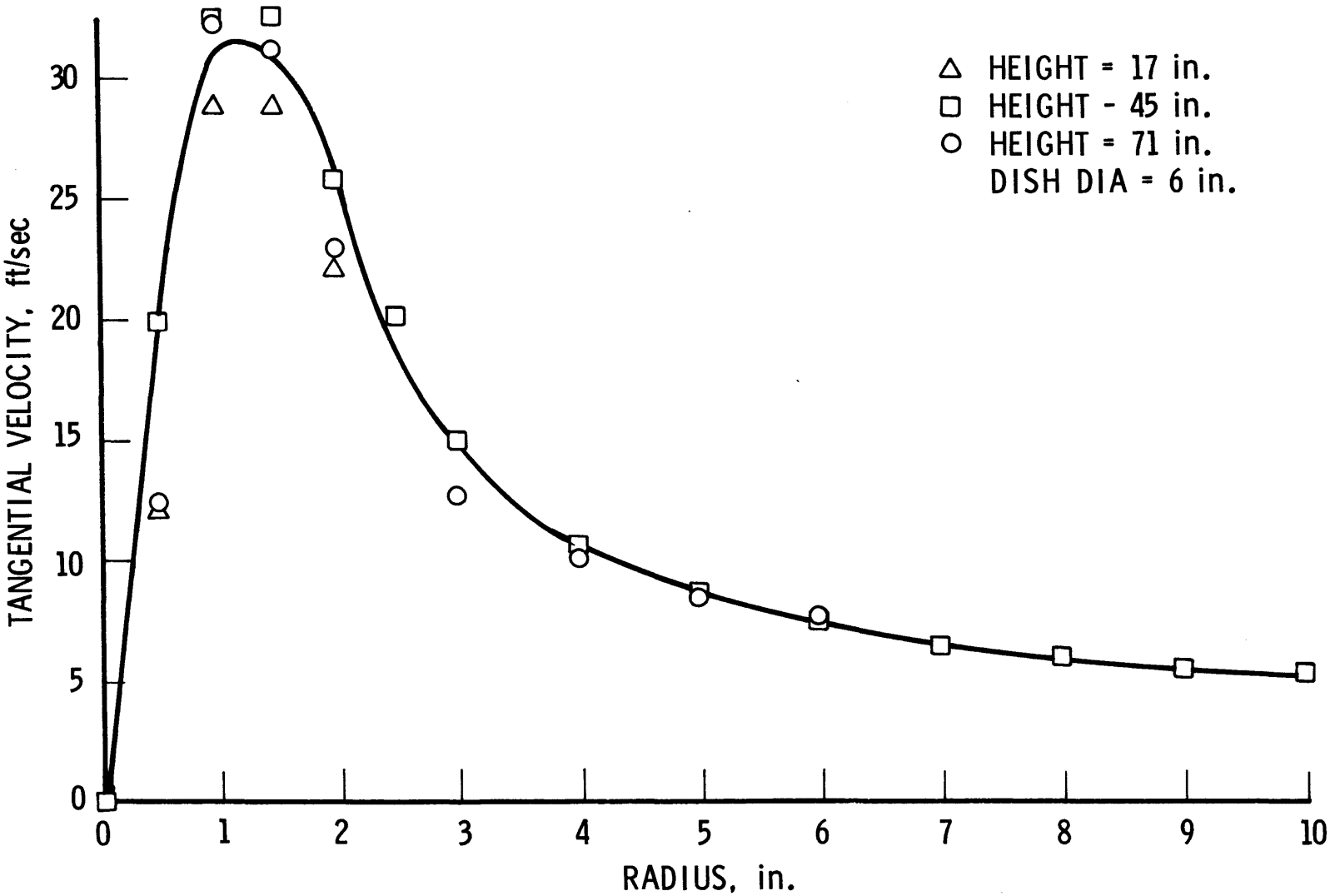


Fig. B-7. Tangential Velocity Distribution at Various Heights

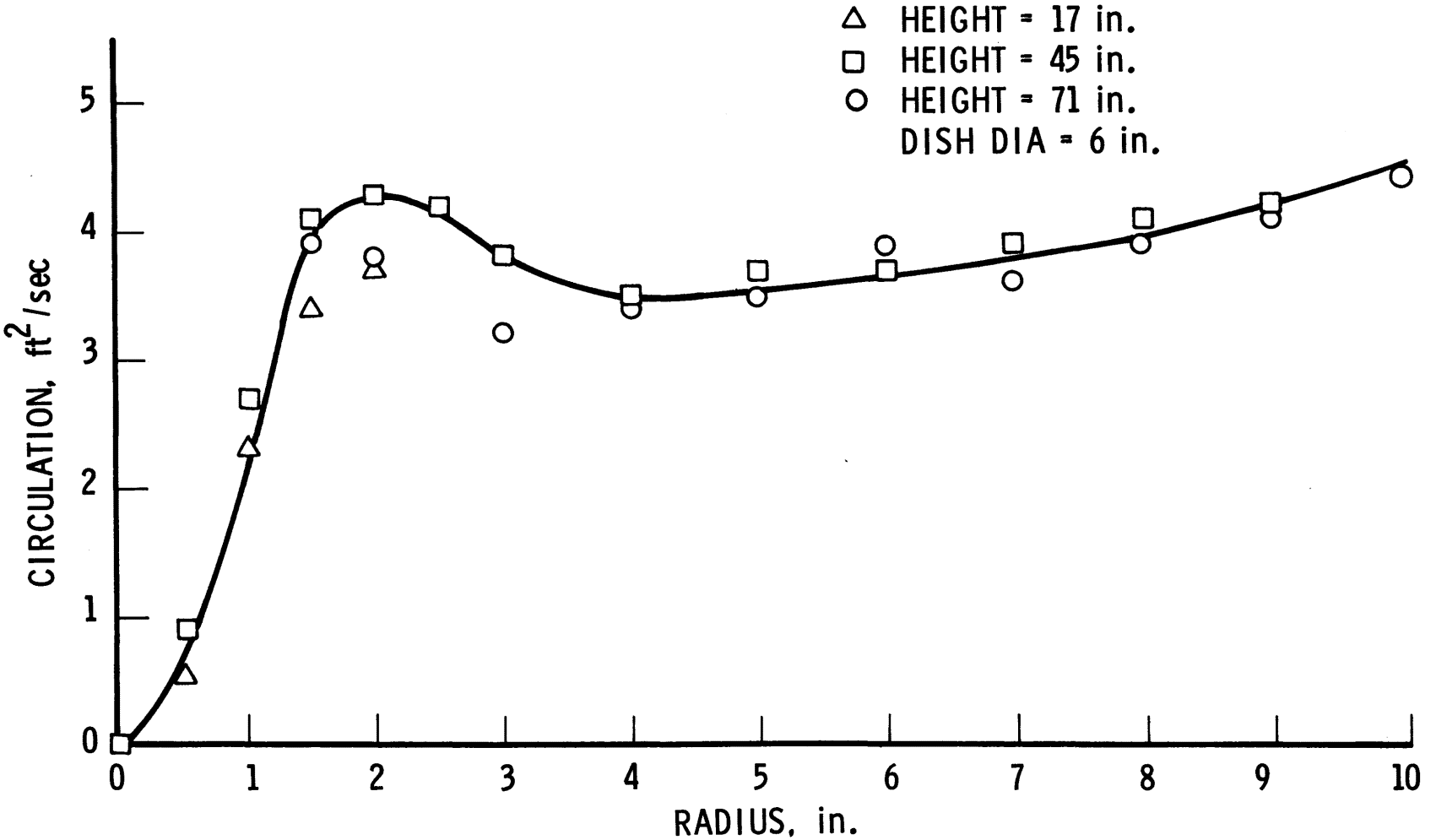


Fig. B-8. Circulation Distribution at Various Heights

With radius, however, the tangential velocity is near zero in the core, rising to a maximum near the core edge and then decreasing in the outer swirl regions, confirming the analytical model proposed. The circulation curve follows a similar pattern in the core, rising to a maximum at the edge and then becoming essentially constant just outside the core edge. Both the tangential velocity and circulation, however, rise to a large value approaching the walls, corresponding to the FASI air velocities. A high value of circulation (approximately 13 $ft^2/sec$) was demonstrated near the wall but variations of the FASI flow rates and the intended changes of gamma near the wall did not cause significant changes to the swirl near the core edge. Some variation in circulation was obtained with change in acetone dish size (see Fig. B-4) and greater variation occurred with changes in wood crib sizes (see Fig. 31).

Figure B-9 gives temperature profiles at the three vertical locations indicated. These profiles indicate that the centerline temperatures are lower than those in regions somewhat off the centerline and that the core size is approximately 3 in. in diameter.

Figure B-10 shows the variation in centerline temperature and axial velocity with height. The centerline temperature decreases with height while the axial velocity peaks near the middle of the vertical extent measured.

Finally, Figs. B-11 and B-12 give the core velocity profiles. Results are given in terms of vector direction and the vertical component of the velocity as they vary with radius. In velocity direction data, 0 deg represents the vertical flow and 90 deg indicates tangential flow. These results indicate that the velocity does indeed vary from vertical at the axis to purely tangential just outside the core.

The measurement of velocities with the boundary layer pitot rakes have shown that the velocities must be low since the dynamic head was below the sensitivity level of the instrument ($v_r < 2\text{-}3$ ft/sec). This agrees with the analytical prediction of radial inflow velocities estimated in Section IV to be approximately 1 ft/sec.

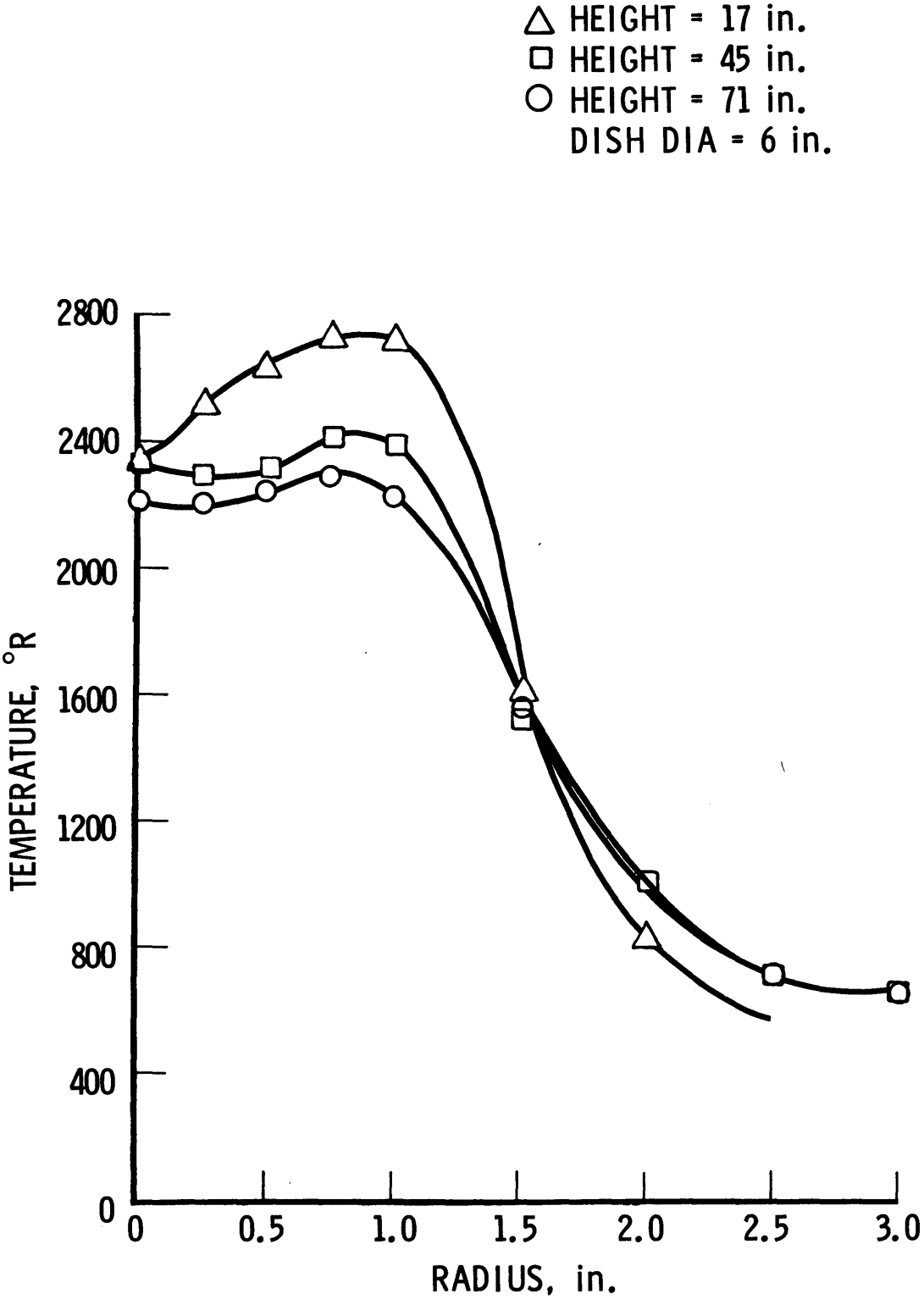


Fig. B-9. Temperature Profiles at Various Heights

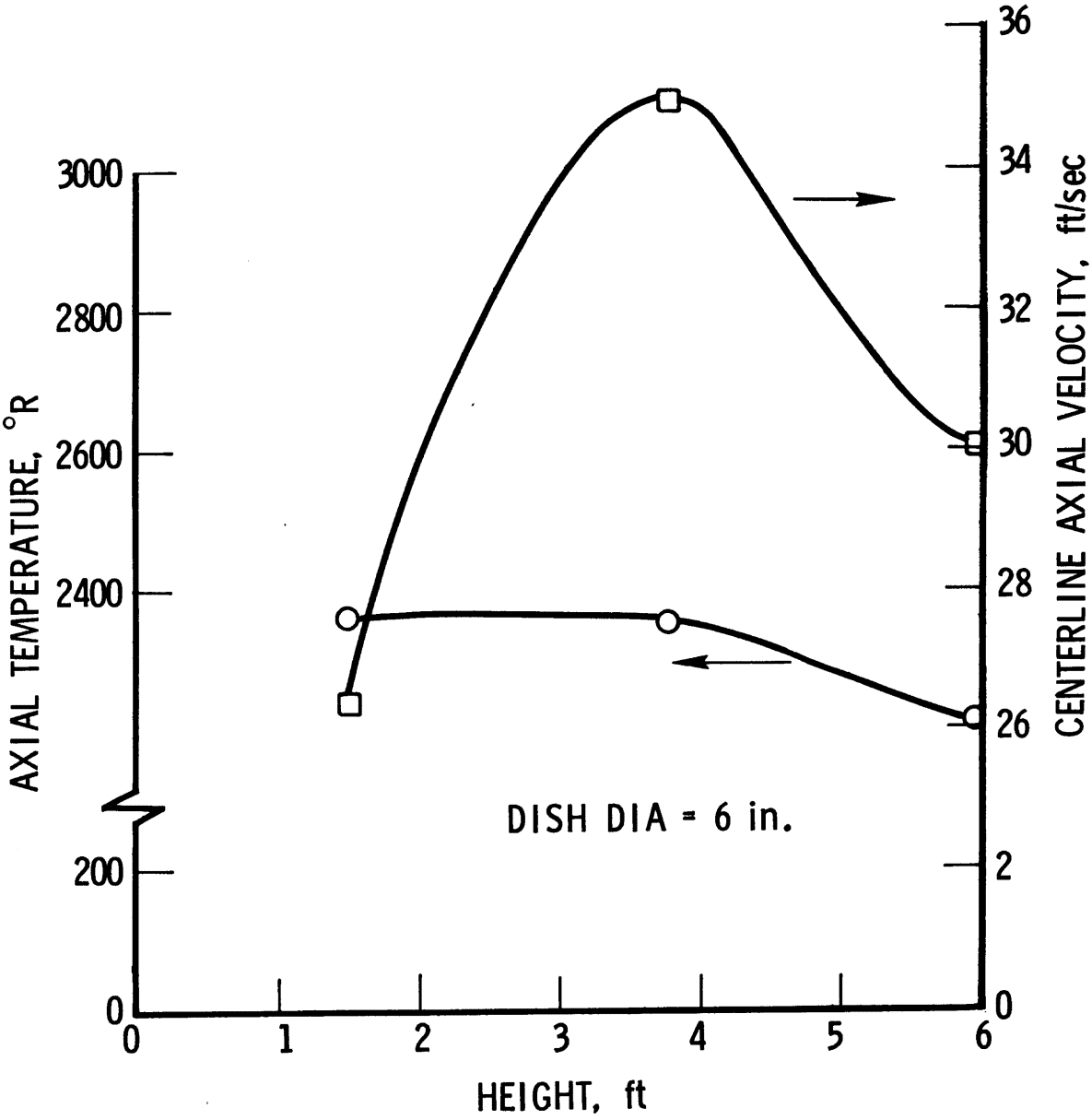


Fig. B-10. Axial Temperature and Vertical Velocity Variation with Height

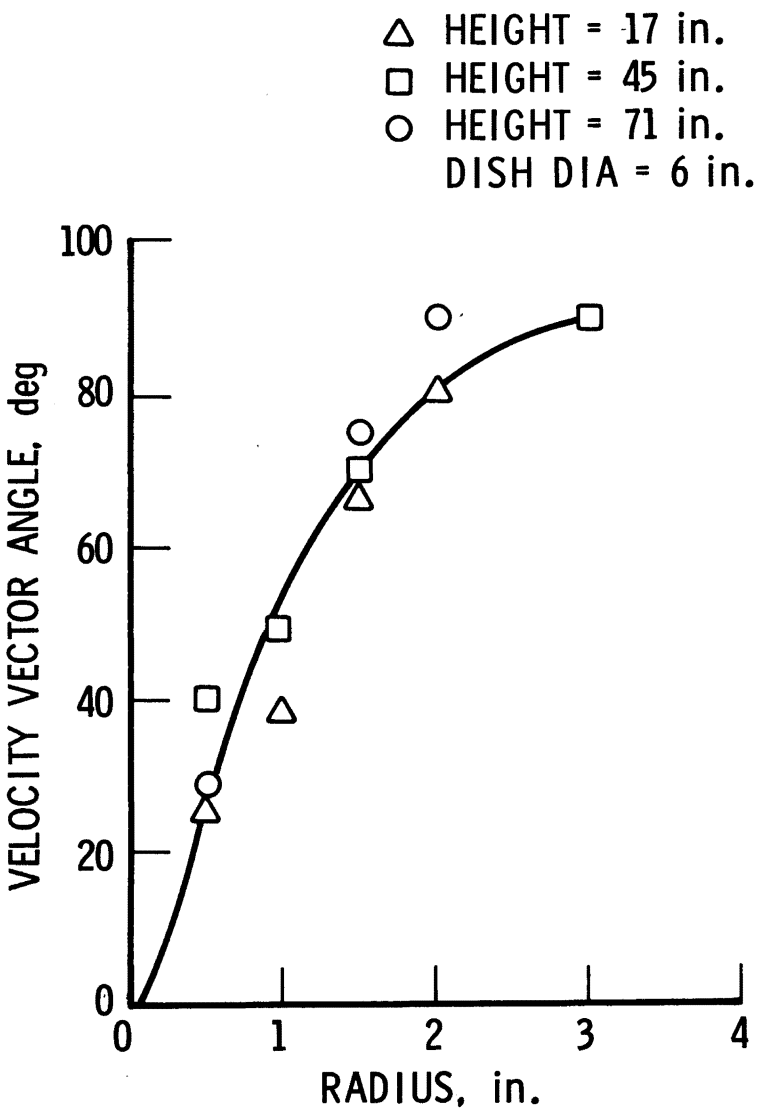


Fig. B-11. Velocity Vector Direction Variation with Radial Position

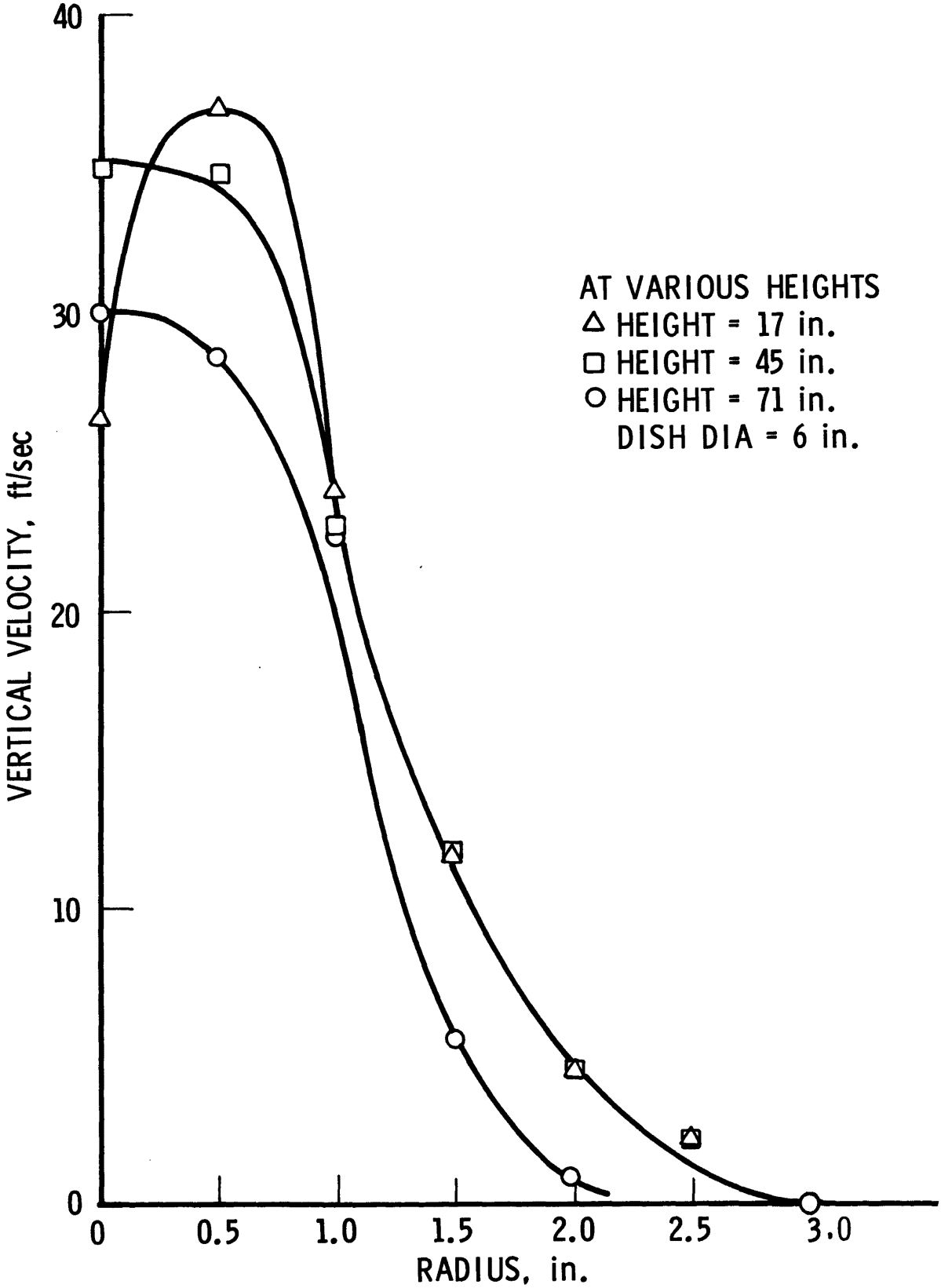


Fig. B-12. Vertical Velocity Profiles at Various Heights

## SYMBOLS

| | |
|---|---|
| $a$ | core radius, ft (Section IV) |
| $a'$ | a nondimensional parameter characterizing the fuel heat convection [Eq. (50)] |
| $a_o$ | core radius at z = 0 |
| $A$ | firebrand drag area ($ft^2$) (Section IV) |
| $A_{(t)}$ | firebrand maximum cross section, $cm^2$ |
| $b'$ | a nondimensional parameter characterizing boundary layer radial mass inflow [Eq. (51)] |
| $C_f$ | skin friction coefficient at the core/air interface |
| $C_D$ | drag coefficient |
| $C_p$ | specific heat, core mean specific heat at temperature T, $Btu/lb_m$-$^oR$ |
| $C_{p_\infty}$ | ambient air specific heat, $Btu/lb_m$-$^oR$ |
| $d$ | characteristic fuel diameter or size |
| D, D(t) | instantaneous firebrand diameter |
| $D_{f\ell}$ | firebrand diameter, cm, after completion of in-wind burning |
| $D_o$ | initial firebrand diameter--cm in Sections II, III; ft in Section IV |
| $g$ | standard acceleration due to gravity, 981 $cm/sec^2$ or 32.18 $ft/sec^2$ |
| $h$ | total heat transfer coefficient between the swirling flow and the burning surface, $Btu/ft^2$-sec-$^oR$ |
| $h_o$ | initial thickness of flat plate firebrand, cm (Section III) |
| $h_o$ | fuel surface heat transfer coefficient without swirl, $Btu/ft^2$-sec-$^oR$ (Section IV) |
| $h_w$ | added convective heat transfer contribution due to swirl, $Btu/ft^2$-sec-$^oR$ |

SYMBOLS (Continued)

| | |
|---|---|
| $k$ | experimentally determined constant appearing in firebrand density change equations, $sec/cm^2$ |
| $L$ | firebrand length--cm (Section III); ft (Section IV) |
| $m_{(t)}$ | firebrand mass, g |
| $M$ | fuel moisture content in percent |
| $\dot{M}$ | total fuel crib burn rate, with swirl, within and outside of core, $lb_m/sec$ |
| $\dot{M}_f$ | core fuel burn rate with swirl, $lb_m/sec$ |
| $M(\xi)$ | nondimensional boundary layer radial velocity profile variable |
| $\dot{M}_o$ | steady-state burn rate of fuel crib without swirl, $lb_m/sec$ |
| $\dot{M}_T$ | $\rho u_o \pi a_o^2$, total mass flow in core, $lb_m/sec$ |
| $N(\eta)$ | nondimensional boundary layer azimuthal velocity profile variable |
| $p$ | pressure, $lb_m/ft\text{-}sec^2$ ($1\ lb_f/ft^2 = 32.18\ lb_m/ft\text{-}sec^2$) |
| $P_r$ | Prandtl number |
| $Q_c$ | net heat of combustion of the fuel which is effective in heating the core gas, $Btu/lb_m$ |
| $Q_i$ | effective heat of ignition of the fuel, $Btu/lb_m$ |
| $Q_m$ | boundary layer mass inflow into core, $lb_m/sec$ |
| $R$ | linear burn rate of fuel with swirl, ft/sec |
| $R_{e_c}$ | characteristic Reynolds number for swirl convection heat transfer to a characteristic wood fuel particle |
| $R_g$ | gas constant, $lb_m\text{-}ft^2/sec^2\text{-}^oR\text{-}(lb_m\text{-mole})$ (Section IV) |
| $R_{g,s}$ | gas constant of core gas at temperature $T_s$ |

| | |
|---|---|
| $R_{g,T}$ | mean gas constant of core gas at temperature T |
| $R_{g,\infty}$ | ambient air gas constant |
| S | total firebrand surface area, $cm^2$ |
| $S_o$ | initial total firebrand surface area, $cm^2$ |
| $S_t$ | Stanton number |
| $t_{f\ell}$ | in-wind burning time, sec |
| T | temperature, local fire whirl core temperature, mean core temperature, $^oR$ (Section IV) |
| $T_s$ | fuel surface burning temperature, $^oR$ |
| $T_\infty$ | ambient temperature, $^oR$ |
| u | vertical velocity, radially averaged core vertical velocity, ft/sec |
| $u_o$ | radially averaged core vertical velocity at core base, ft/sec |
| $v_r$ | boundary layer mean radial velocity, ft/sec |
| V | volume of firebrand, $cm^3$ |
| $V_{BL}$ | boundary layer radial velocity, ft/sec |
| $V_c$ | convection characteristic velocity, ft/sec |
| $V_o$ | initial firebrand volume, $cm^3$ |
| $w_o$ | initial fall velocity, cm/sec |
| $w_{(t)}$ | instantaneous firebrand fall velocity, cm/sec |
| W | azimuthal velocity, ft/sec |
| $W_f$ | instantaneous firebrand fall velocity, ft/sec |
| z | axial variable, ft |
| $z_e$ | vertical extent of the ambient circulation, ft |

SYMBOLS (Concluded)

| | |
|---|---|
| $\alpha$ | see Eq. (44) |
| $\beta$ | g ze/$u_o^2$ [Eq. (44)], or packing ratio in Section IV-D-1 |
| $\gamma$ | relative initial radial position of firebrand |
| $\Gamma$ | ambient circulation, $ft^2/sec$ ($\Gamma$ = Wa) |
| $\zeta$ | nondimensional boundary layer axial variable for radial velocity |
| $\eta$ | nondimensional boundary layer vertical coordinate |
| $\mu_a$ | ambient air viscosity, poise |
| $\nu$ | mean core kinematic viscosity, $ft^2/sec$ |
| $\nu_\infty$ | ambient kinematic viscosity, $ft^2/sec$ |
| $\rho$ | density, core mean density, $lb_m/ft^3$ (Section IV) |
| $\rho_b$ | bulk density of the fuel, $lb_m/ft^3$ |
| $\rho_c$ | final burning wood density, $g/cm^3$ |
| $\rho_{f\ell}$ | sample density, $g/cm^3$, at termination of in-wind burning |
| $\rho_o$ | initial firebrand density, $g/cm^3$ |
| $\rho_s$ | core gas density at a temperature of $T_s$, $lb_m/ft^3$ |
| $\rho_w$ | firebrand density, $lb_m/ft^3$ |
| $\rho_{w_o}$ | initial firebrand density, $lb_m/ft^3$ |
| $\rho_\infty$ | ambient air density, $lb_m/ft^3$ |
| $\rho$, $\rho(t)$ | instantaneous firebrand density, $g/cm^3$ |
| $\sigma$ | fuel particle surface area/particle volume, $ft^{-1}$ |
| $\tau_o$ | fuel surface shear stress, $lb_m/ft\text{-}sec^2$ |
| $\omega$ | angular velocity, $sec^{-1}$ |

## REFERENCES


1. Muraszew, A., "Firebrand Phenomena," The Aerospace Corporation, Report No. ATR-74(8165-01)-1, 1974.

2. Muraszew, A., J. B. Fedele and W. C. Kuby, "Firebrand Investigation," The Aerospace Corporation, Report No. ATR-75(7470)-1, 1975.

3. Rothermel, R. C., "A Mathematical Model for Predicting Fire Spread in Wildland Fires," USDA Forest Service Res. Paper INT-115, 1972.

4. Cheney, N. P. and G. A. V. Bary, Forest Research Institute, Canberra, A. C. T., 1969.

5. Tarifa, C. S., "Transport and Combustion of Firebrands," U. S. Department of Agriculture, Madrid University Report, Vol. II, 1967.

6. Byram, G. M. and R. E. Martin, "The Modeling of Fire Whirlwind," Forest Science, 16(4), 1970, pp. 386-399.

7. Schlichting, H., Boundary Layer Theory, McGraw-Hill Book Co., New York, New York, 1960.

8. Fons, W. L., "Heating and Ignition of Small Wood Cylinders," Industrial and Engineering Chemistry, 42(10), November 1950.

9. Lee, S. L., "Axisymmetrical Turbulent Swirling Natural Convection Plume," Part 1, J. of Appl. Mech., 33, September 1966, pp. 647-655.

10. Emmons, H. W. and S. J. Ying, "The Fire Whirl," Eleventh Symposium on Combustion (1966), The Combustion Institute, 1967, pp. 475-488.

11. Lee, S. L., "Axisymmetrical Turbulent Swirling Natural Convection Plume," Part 2, J. of Appl. Mech., 33, September 1966, pp. 565-661.

12. Morton, B. R., Sir Geoffrey Taylor, and J. S. Turner, "Turbulent Gravitational Convection from Maintained and Instantaneous Sources," Proceedings of Royal Society of London, 234, 1956, pp. 1-22.

13. Byram, G. M., Combustion of Forest Fuels, Forest Fire Control and Use, K. R. Davis (Ed.), McGraw-Hill Book Co., Inc., New York, New York, 1959.

REFERENCES (Continued)


14. Harmathy, T. Z., "A New Look at Compartment Fires, Part I," Fire Technology, 8(3), August 1972, pp. 196-217.

15. King, A. R., "Characteristics of a Fire-Induced Tornado," Australian Meteorological Magazine, 44, March 1964, pp. 1-9.

16. Martin, R. E., D. Pendleton, and W. Burgess, "Effect of Fire Whirlwind Formation on Solid Fuel Burning Rates," Nineteenth Symposium on Combustion, The Combustion Institute, 6-7 May 1974.

17. Rott, N. and W. S. Lewellen, "General Research, Boundary Layers in Rotating Flows," The Aerospace Corporation, Report No. ATN-64 (9227)-6, 4 September 1964.

18. Hoerner, S. F., Fluid-Dynamic Drag, 1958, published by the author.

19. Delaney, N. K. and N. E. Sorenson, "Low Speed Drag of Cylinders of Various Shapes," NACA Technical Note 3038, 1953.

20. Lee, S. L. and G. M. Hellman, "Firebrand Trajectory Study Using an Empirical Velocity-Dependent Burning Law," Combustion and Flame, 15, 1970, pp. 265-274.

21. Postolka, R., "Characterization of Fire Whirls for Prediction of Firebrand Generation," UCSB Master of Science Thesis in Mechanical Engineering, September 1975.

22. Thomas, P. H., "Effect of Fuel Geometries on Fires," Building Research Establishment, Great Britain, February 1974.